

JUACEP Program at University of Michigan & UCLA 2014 - 2015



Japan-US Advanced Collaborative Education Program

Nagoya University

Table of Contents

<1> About the Program	
(a) Overview	... 4
(b) Participants	... 5
<2> Research Reports	... 7
<3> Research Presentations	...69
(a) For 2014 Long-term course	
(b) For 2015 Short-term course	
(c) For 2015 Medium-term course	
<4> Findings through JUACEP	
(a) Students' reviews	...94
(b) Questionnaires (in Japanese)	...113

<1> About the Program

(a) Overview

(b) Participants

(a) Overview

JUACEP provides three program courses for students of the Graduate School of Engineering at Nagoya University to study abroad: a short-term (two months) course; a medium-term (six months) course; and a long-term (one year) course. Choosing one of those courses the selected students are offered an opportunity to work together with faculty and other researchers or students from all over the world at the world's top universities.

Each student works on a research project related to his/her own master's thesis topic while belonging to a specialized laboratory of the University of Michigan or UCLA. In addition to research, the students are expected to attend lab seminars, lab discussions and other events. At the end of each course, the students are required to submit a research report to their mentors at the host institution, then give a research presentation based on their achievements in front of the faculty and peer students at JUACEP Workshop held in Nagoya University. The report and the presentation are primary requisites of the program for course credits.

This publication is compiling the activities of the following students.

- [a] One student of long-term course from August 2014 to July 2015 at Univ. Michigan
- [b] Five students of medium-term course from August 2015 to January 2016 at Univ. Michigan
- [c] Six students of medium-term course from August 2015 to January 2016 at UCLA
- [d] One student of short-term course from August to September 2015 at Univ. Michigan
- [e] Four students of short-term course from August to September 2015 at UCLA

JUACEP 2014 Long-, 2015 Short-/Medium-term Courses Flowchart

	Long-term course, 2014	Medium-term course, 2015	Short-term course, 2015	
August 2014 January 2015	[a] Long-term course study at UM from Aug. 2014 to Jul. 2015			
February		Public announcement and accepting application (Jan. – Mar.)		
March		Screening candidates		
April		Approaching faculty of UM/UCLA by the selected students (UM course students are checked up English qualification by the faculty, and UCLA course students apply for VGR*. Both are on DS-2019** procedure.)		
May		J-1 visa application		
June				
July				
August	<i>13th Workshop, Aug. 6</i>	[b,c] Medium-term course study at UM/UCLA from Aug. 2015 to Feb. 2016	[d,e] Short-term course study at UM/UCLA from Aug. to Sep. 2015	
September				<i>15th Workshop, Oct. 2</i>
October				
November				
January 2016				
February		<i>16th Workshop, Feb. 4</i>		

*VGR: Visiting Graduate Researcher for UCLA

**DS-2019: Certificate of eligibility to obtain J-1 Visa

(b) Participants

University of Michigan

Long-term (Program period: August 5, 2014 – August 1, 2015)

Name		Advisor at NU	Advisor at UM
Shun Arakane	M1	Prof. Seiichi Hata Micro-Nano Systems Engineering	Prof. Jay Guo Mechanical Engineering

Medium-term (Program period: August 5, 2015 – January 31, 2016)

Name		Advisor at NU	Advisor at UM
Takamasa Horibe	M2	Prof. Norihiko Yoshikawa Aerospace Engineering	Prof. Brent Gillespie Mechanical Engineering
Hiroto Izuoka	M1	Prof. Noritsugu Umehara Mechanical Science and Engineering	Prof. Xiaogan Liang Mechanical Engineering
Michihiro Kanie	M1	Prof. Seiichi Hata Micro-Nano Systems Engineering	Prof. Albert Shih Biomedical Engineering
Kiichi Okuno	M1	Prof. Noritsugu Umehara Mechanical Science and Engineering	Prof. Bogdan Epureanu Mechanical Engineering
Ryo Yamaguchi	M1	Prof. Noritsugu Umehara Mechanical Science and Engineering	Prof. Peter Green Materials Science and Engineering

Short-term (Program period: August 5, 2015 – September 26, 2015)

Name		Advisor at NU	Advisor at UM
Shintaro Oyama	M1	Prof. Noritsugu Umehara Mechanical Science and Engineering	Prof. Levi Thompson Chemical Engineering

UCLA

Medium-term (Program period: August 4, 2015 – January 31, 2016)

Name		Advisor at NU	Advisor at UCLA
Takahiro Hatano	M1	Prof. Yang Ju Mechanical Science and Engineering	Prof. Xiaochun Li Mechanical and Aerospace Engineering
Yusuke Kasai	M1	Prof. Fumihito Arai Micro-Nano Systems Engineering	Prof. Chang-Jin Kim Mechanical and Aerospace Engineering
Taichi Nakao	M1	Prof. Noritsugu Umehara Mechanical Science and Engineering	Prof. Suneel Kodambaka Materials Science and Engineering
Shogo Okishio	M1	Prof. Hosei Nagano Aerospace Engineering	Prof. Laurent Pilon Mechanical and Aerospace Engineering
Masaki Sato	M1	Prof. Makoto Kobashi Materials Science and Engineering	Prof. Suneel Kodambaka Materials Science and Engineering
Takamichi Suhara	M1	Prof. Noritaka Usami Materials Physics and Energy Engineering	Prof. Kang L. Wang Electrical Engineering

Short-term (Program period: August 4, 2015 – September 26, 2015)

Name		Advisor at NU	Advisor at UCLA
Junya Kato	M1	Prof. Tsuyoshi Inoue Mechanical Science and Engineering	Prof. Tsu-Chin Tsao Mechanical and Aerospace Engineering
Shunsuke Okumura	M1	Prof. Noritsugu Umehara Mechanical Science and Engineering	Prof. Suneel Kodambaka Materials Science and Engineering
Ikuya Onozato	M1	Prof. Eiji Shamoto Mechanical Science and Engineering	Prof. Katsushi Arisaka Physics and Astronomy
Asami Yokoyama	M1	Prof. Yoshinobu Baba Applied Chemistry	Prof. Hsian-Rong Tseng Molecular and Medical Pharmacology

Coordinators at Partner Universities

Prof. Katsuo Kurabayashi
Prof. Jenn-Ming Yang

Mechanical Engineering, University of Michigan
Materials Science and Engineering, UCLA

JUACEP Members

Prof. Noritsugu Umehara
Prof. Yang Ju
Assoc. Prof. Yasumasa Ito
Tomoko Kato
Chiharu Yada

Mechanical Science and Engineering
Mechanical Science and Engineering
Mechanical Science and Engineering
Administrative Staff
Administrative Staff

<2> Research Reports

Studies at University of Michigan

- [L] Shun Arakane mentored by Prof. Jay Guo (P.9)
Fabrication of Radio Frequency Devices by Use of 3D Printing Technology
- [M] Takamasa Horibe mentored by Prof. Brent Gillespie (P.10)
Comparing Series Elasticity and Admittance Control for Haptic Rendering
- [M] Hiroto Izuoka mentored by Prof. Xiaogan Liang (P.20)
Nanofluidic-Flow-Assisted Assembly (NFAA) of Well-dispersed Plasmonic Nanostructures into Nanoslit Sensors
- [M] Michihiro Kanie mentored by Prof. Albert Shih (P.25)
3D-Printing of Porous and Solid Silicone Structures
- [M] Kiichi Okuno Mentored by Prof. Bogdan Epureanu (P.26)
Vibration-Based Identification of Interphase Damping of FRP
- [M] Ryo Yamaguchi mentored by Prof. Peter Green (P.27)
Physical Aging of Star-shaped Polymer Nanocomposites
- [S] Shintaro Oyama mentored by Prof. Levi Thompson (P.28)
Effects of Micropores on Pseudocapacitive Charge Storage in Vanadium Nitrides

Studies at UCLA

- [M] Takahiro Hatano mentored by Prof. Xiaochun Li (P.34)
Micro/Nano Sensing Technique on Diamond Tip Using Microsave
- [M] Yusuke Kasai mentored by Prof. Chang-Jin Kim (P.38)
Study of Trapped Air under Shear Flow Using Transparent Single Trench
- [M] Taichi Nakao mentored by Prof. Suneel Kodambaka (P.39)
Chemical Vapor Deposition of MoS₂ Thin Layers
- [M] Shogo Okishio mentored by Prof. Laurent Pilon (P.45)
Property Review and Thermal Conductivity Measurement on Lunar Regolith and Regolith Simulant
- [M] Masaki Sato mentored by Prof. Suneel Kodambaka (P.55)
Growth and Characterization of Single-Crystalline Zr (0002)/Al₂O₃ (0001) and ZrC (111)/ Al₂O₃ (0001) Thin Films
- [M] Takamichi Suhara mentored by Prof. Kang L. Wang (P.56)
Electrical Transport Properties of Undoped BaSi₂ Evaporated Thin Films
- [S] Junya Kato mentored by Prof. Tsu-Chin Tsao (P.61)
Dynamics of A Rotating Shaft in Magnetic Bearings
- [S] Shunsuke Okumura mentored by Prof. Suneel Kodambaka (P.65)
Optimization of Deposition Conditions of HCP Zr
- [S] Ikuya Onozato mentored by Prof. Katsushi Arisaka (P.66)
Laser beams for 2D and 3D Worm Tracker
- [S] Asami Yokoyama mentored by Prof. Hsian-Rong Tseng (P.67)
Thermoresponsive NanoVelcro Substrate Technology for CTC Purification and AR-v7 Mutation Analysis of Castration-Resistant Prostate Cancer

**[L]; Long-term course, [M]; Medium-term course, [S]; Short-term course*

FABRICATION OF RADIO FREQUENCY DEVICES BY USE OF 3D PRINTING TECHNOLOGY

Shun Arakane

Department of Micro-Nano System Eng. Graduate School of, Nagoya University
arakane.shun@b.mbox.nagoya-u.ac.jp

Supervisor: L. Jay Guo

Electrical Electronics and Computer Science, University of Michigan
guo@umich.edu

ABSTRACT

In this paper, a novel method is developed to fabricate flexible and transparent radio frequency (RF) devices by use of 3D printed mask and mold. To get flexibility and optical transparency, transparent and flexible materials such as silver nanowires (AgNWs) and cyclic olefin copolymer were utilized for the RF devices. Firstly, chipless radio frequency identification (RFID) strain sensor based on electrical LC resonator is designed and demonstrated in this paper. The resonant frequency of the RFID tag changes in response to the applied tensile strain along the x- and y-directions. The transmittance of the RFID tag is ~35% over the visible range of the electromagnetic spectrum. Secondly, a substrate integrated waveguide (SIW) structure is realized with a flexible substrate for wearable application. Easy, fast and low-cost processes to get SIW structure are achieved by using two layers of the thin cyclic olefin copolymer.

Undisclosed

Comparing Series Elasticity and Admittance Control for Haptic Rendering

Takamasa Horibe

Department of Aerospace Engineering, Nagoya University
horibe.takamasa@j.mbox.nagoya-u.ac.jp

Supervisor: R. Brent Gillespie

Department of Mechanical Engineering, University of Michigan
brentg@umich.edu

Abstract

The control and hardware design of any haptic device must address two chief challenges: rendering the virtual wall as stiff as possible, and rendering free-space motion as free as possible. We use series elastic actuators in order to realize these two objectives. The series elastic element can effectively hide an apparent impedance or high friction caused by highly geared transmission, hence it is able to render not only a high virtual impedance but also free-space motion. We also focus on the coupled stability of haptic interfaces based on passivity criteria and compare the performance limit of two haptic architectures: admittance control device and SEA device.

1 Introduction

The design of a haptic device and its controllers is invariably a study in tradeoffs. In theory, rendering a programmable immitance¹ simply requires sourcing a force in certain relation to sensed motion or sourcing a motion in the inverse relation to sensed force. However pure force and motion sources are difficult to find on the shelf or even to invent. At a certain frequency the mass used to build the device will necessarily foil any efforts to source force or motion and especially the inherent dynamics dominates the immitance rendered at high frequencies. A transmission can be used to increase the force output capacity but only at the expense of increased effective inertia and lower motion sourcing capability.

Haptic display devices fall into two basic families: the impedance display devices that function as force sources (sensing motion) and the admittance

display devices that function as motion sources (sensing force).

The impedance control device has a low impedance when its motors are unpowered, and it uses motor power to increase that impedance when appropriate to render the feel of a virtual object. Therefore to achieve a good free-space behavior using an impedance control device requires astute hardware design to minimize the inherent device impedance, this makes the free space motion (at high frequencies) is relatively free. On the other hand it can not render a very high stiffness because the motor does not have a high gear ratio transmission required to produce the high forces.

The admittance control device, on the other hand, has a high impedance when its motors are unpowered and it energizes its motors to decrease or increase that impedance when appropriate for haptic rendering. The imposed force from the user is sensed with a force sensor placed as close as possible to the point of contact with the user. The measured force is used to calculate the desired position. Even though this architecture can render a high virtual impedance, the behavior at high frequency is dominated by the high apparent mass created by the gear ratio, and the free space motion (at high frequencies) is in fact not very free.

In this paper, we employ series elastic actuators (SEAs) for a haptic interface. The basic idea of SEAs is introduced by Pratt and Williamson [6] and recognized to have significant advantages in robot designs but have not found their way into the design of haptic devices, for a haptic interface. The SEA has their roots in the desire to achieve smooth force control and minimize impact forces in robots interacting with their environments and it also has some advantages for a haptic interface. The series elastic element provides a sensitive measure of the force of interaction and also significantly reduces the backdrive impedance of the device, thus impact forces from the environment are attenuated with a reduced apparent mass

¹*Immitance* is a term can be used to refer to the relationship between force and motion with specifying input and output, whereas admittance implies motion response to force and impedance implies force response to motion. *Immitance* was introduced by Bode [1] but is no longer as familiar as *impedance* and *admittance*

due to the intervening spring. Furthermore the character can also make it possible to render a smooth free motion even though its inherent impedance is very high. Despite the advantages described above, there is a shortcoming which is a reduction of a maximum virtual stiffness that the haptic device can render.

Since the SEA device can use a highly geared transmission without considering the back drivability, it is able to render a higher stiffness than the impedance control device can, but not as high as the admittance control device can due to the inevitable instability. The SEA device can be unstable when it renders a virtual stiffness, so stability analysis is needed to clarify the limitations of its performance. It is important for a haptic device to be stable even if it contacts a user. In the field of haptics, the device and the user are coupled by direct contact and they are analyzed as a unit. Even if each component of the coupled system is stable, the whole coupled system can show unstable behavior. On the other hand, if the each component is passive, the passivity theory guarantees that the coupled system as a whole can be passive and still stable. Generally the human is assumed to be a passive system, so we discuss the passivity condition for the haptic interface.

In this paper, at first, we explore the promise of series elasticity as a means to circumvent the shortcomings of admittance display, no free motion at high frequencies. We compare to experimental results produced using a platform that supports both admittance display and display through a series elastic element. We also make a direct comparison of the capacity of a haptic device with a series spring and an admittance display device in terms of their capacity to stably render a range of immitances.

2 Model Description

2.1 Admittance Control Devices

A certain relationship between force and motion may be rendered to a human user through a haptic device using either impedance control or admittance control. Impedance control is the most common approach for haptic rendering; it is employed by many haptic devices such as the Phantom [15]. One advantage of impedance control is the exclusion of load cells. However, the haptic device used in impedance control must be designed for good backdrivability (low inherent backdrive impedance).

In contrast, admittance control employs force sensing to close a loop around a haptic device with a relatively large inherent backdrive impedance. Actuators with significant gearing or other transmissions that provide for a large torque output capacity also result in a high effective inertia and damping (high backdrive impedance). Then motion is commanded

in relation to sensed user interaction force to render a programmable (lower) backdrive impedance.

Let us begin by describing admittance control in some detail. A schematic model and a block diagram model of an admittance-controlled device is shown in Fig. 1, 2 respectively.

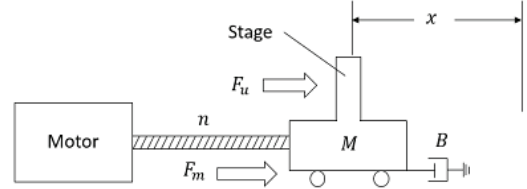


Figure 1: Schematic model of haptic device at admittance control

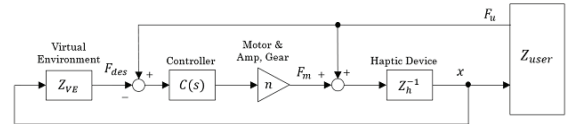


Figure 2: Block diagram at admittance control

Let M designate the the effective mass of the device end-effector grasped by the human user and let B describe damping to ground. The user applies force F_u and a motor applies force F_m through a transmission with gear ratio n . The inherit impedance of haptic device is written as

$$Z_h = Ms^2 + Bs. \quad (1)$$

A feedback controller $C(s)$ is used to close a loop so as to cause sensed for F_u to track the desired force F_{des} which is specified by the virtual environment Z_{VE} . The relation in admittance architecture is given from Fig. 2 as follows.

$$X = Z_h^{-1}(F_m + F_u) \quad (2)$$

$$F_m = nC(s)(F_u - F_{des}) \quad (3)$$

$$F_{des} = Z_{VE}X \quad (4)$$

Here let us define the driving point impedance as $Z_{DP} \equiv F_u/\dot{X}$. Hence the closed loop driving point impedance in this architecture may be expressed using:

$$Z_{DP-Adm}^{CL} = \frac{F_u}{V_u} = \frac{nC(s)Z_{VE} + Z_h}{s(nC(s) + 1)}. \quad (5)$$

where CL means closed loop. In this expression, we can see that the driving point impedance is shaped by tuning the feedback gain $C(s)$. As $(C(s) \rightarrow \infty)$ the

driving point impedance converges to the virtual environment impedance: $Z_{DP} \rightarrow Z_{VE}/s$, which means a perfect transparency.

We also define the driving point impedance in open loop Z_{DP}^{OP} . This is given by substituting $C(s) = 0$ into Eq. (5) and is expressed as

$$Z_{DP-Adm}^{OP} = \frac{Z_h}{s}. \quad (6)$$

As we mentioned, the inherent impedance of haptic device usually is usually large (non-backdrivable) when admittance control is used. Inevitably, the rendered impedance must approach the inherent impedance at high frequencies.

2.2 Series Elastic Actuator Device

We now introduce the control architecture of a haptic device that features a series elastic element. Series elastic actuators have been proposed in robotics [6] for various advantaged afforded by good backdrivability.

A schematic model is presented in Fig. 3.

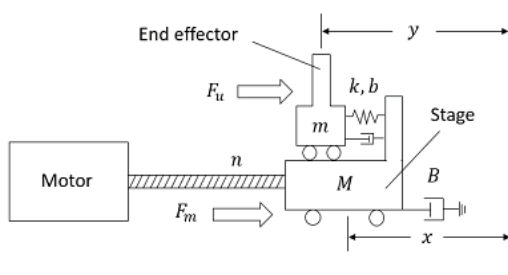


Figure 3: Schematic model of haptic device at series elastic actuator control

As depicted in Fig. 3, an elastic element (physical spring) is placed between the stage and end-effector. By virtue of this spring the SEA device has a low apparent (open loop) impedance. Additionally, the force F_u applied by the human user is available if the relative displacement of the spring is measured and the spring constant is known: $F_u \approx k(y - x)$. Thus a force sensor is not required. A block diagram is shown in Fig. 4.

Using this model, the following relationships in Laplace form are available:

$$F_k = k(X - Y) \quad (7)$$

$$F_b = sb(X - Y) \quad (8)$$

$$X = Z_h^{-1}(F_m - F_k) \quad (9)$$

$$Y = Z_e^{-1}(F_u + F_k) \quad (10)$$

$$F_m = C(s)(-F_k - F_{des}) \quad (11)$$

$$F_{des} = Z_{VE}Y \quad (12)$$

where $Z_e = ms^2$ is the impedance of the end-effector and k, b are the stiffness and damping of the physical spring placed between stage and end-effector.

Here the driving point impedance is defined as $Z_{DP} \equiv F_u/\dot{Y}$ and manipulation of the equations above produces:

$$Z_{DP-SEA}^{CL}(s) = \frac{Z_e(Z_h + knC(s) + k') + k'(Z_h + nC(s)Z_{VE})}{s(Z_h + knC(s) + k')} \quad (13)$$

where $k' = k + sb$. It should be mentioned that the rendered impedance does not converge to the virtual environment as feedback gain increases to infinity.

$$\frac{F_u}{Y} \rightarrow Z_e + Z_{VE} \left(1 + \frac{b}{k}s\right) \quad (C(s) \rightarrow \infty). \quad (14)$$

This is because the user force has been approximated by neglecting the end-effector. However, the end-effector is usually designed with a small mass compared to the stage ($m \ll M$) and if the force is dominated by spring rather than damping, such errors can be neglected.

The driving point impedance in open loop may then be expressed as

$$Z_{DP-SEA}^{OP} = \frac{1}{s} \left(Z_e + \frac{Z_h k'}{Z_h + k'} \right) \quad (15)$$

One can recognize in Eq. (15) the series coupling of two impedances Z_e and $Z_h k'/(Z_h + k')$. The second impedance can be seen as the parallel coupling of Z_h and k' . Thus the open loop impedance is smaller than the open loop impedance of the admittance control device.

This SEA architecture has an advantage for good back-drivable, but there also exist some disadvantage for stability. The stability of SEA is discussed in some papers [14], [13]. We especially focus on comparison between two architectures, Admittance and SEA in term of Z-width, which is described in "Coupled Stability" section.

2.3 Comparative Analysis

It is useful to compare the performance of the Admittance Display and SEA devices when they both attempt to render freespace ($Z_{VE} = 0$) using the same controller.

In the following, the virtual environment Z_{VE} is set as a constant stiffness as $Z_{VE}(s) = K_{VE}$ and controller is set as a proportional gain as $C(s) = C_p$. One can examine this backdrivability by Z_{DP} calculated in Eq.(16),(17).

At low frequency, the gains converge to the same value, while the gains in high frequency have different values. The mass of the end-effector is very small compared to the stage ($m \ll M$), so generally the gain

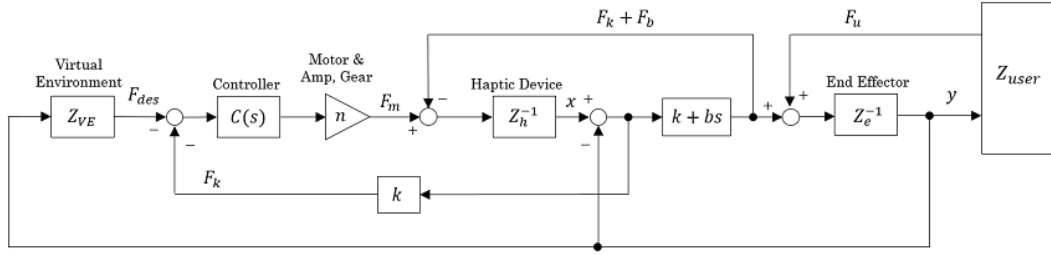


Figure. 4: SEA Block Diagram with end-effector

of impedance in the SEA architecture is smaller than in the Admittance architecture.

$$|Z_{DP}(j\omega)|_{Adm} = \begin{cases} \frac{M}{1+nC_p} \omega & (\omega \gg 1) \\ \frac{nC_p}{nC_p+1} \frac{K_{VE}}{\omega} & (\omega \ll 1, K_{VE} \neq 0) \\ \frac{B}{nC_p+1} & (\omega \ll 1, K_{VE} = 0) \end{cases} \quad (16)$$

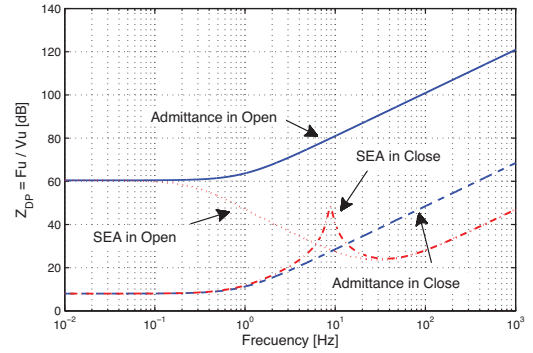
$$|Z_{DP}(j\omega)|_{SEA} = \begin{cases} m\omega & (\omega \gg 1) \\ \frac{nC_p}{nC_p+1} \frac{K_{VE}}{\omega} & (\omega \ll 1, K_{VE} \neq 0) \\ \frac{B}{nC_p+1} & (\omega \ll 1, K_{VE} = 0) \end{cases} \quad (17)$$

Figure 5 shows the Bode plots of the driving point impedance for both the Admittance Display and SEA devices in both an open-loop $C(s) = 0$ and closed loop conditions $C(s) = C_p$. The same proportional gain C_p was used for both devices to produce these graphs.

At low frequency both control architectures behave similarly, but there is a huge difference at high frequencies, which shows the advantage of SEA, good back-drivability.

3 Apparatus Description

We devised a single-axis system that could be configured either as an Admittance Display device or a Series Elastic Actuator. Figure 6, 7 shows both a CAD rendering and photograph of the apparatus. The encoder attached to the back-shaft of the motor measured the angle θ , which can be used to deduce the stage displacement $x = \theta/n_g$, where n_g is the gear ratio. A second encoder measures the relative displacement between stage and end-effector ($x - y$), the displacement spanned by the physical spring. The DC


 Figure. 5: Bode plot showing driving point impedance in open loop Z_{DP}^{OP} and closed loop Z_{DP}^{CL} ($C_p = 10$) rendering $Z_{VE} = 0$ with an Admittance control device and SEA device ($k = 1300$)

motor is connected to the stage and makes a torque proportional to a current generated by an amplifier. The force F_m is generated from the torque through a highly geared ball-screw transmission. Eventually the force is written as $F_m = \eta n_g k_T I$ where η , k_T , I are a efficiency of the transmission, torque constant and current from amplifier respectively. n is denoted as the gain from the current to force. Values for these parameters are shown in Table.1.

A user can handle the end effector and the displacement is measured by encoder, that data is fed back to move motor in order to render desired virtual environment to the user. The best advantage of this apparatus is the back drivability because of the elasticity between the stage and end effector.

The proximal side of a beam load cell is attached to the stage in the case of Admittance Display. The distal side of this loadcell is grasped by the user.

4 Experimental Result

We seek experimental results to support the analytical findings outlined above, in particular to explore

Table. 1: The parameters for SEA control

	character	value	unit
Mass of stage	M	176.4	[kg]
Damping coefficient of stage	B	1051.4	[kg/s]
Mass of end-effector	m	0.0353	[kg]
Damping coefficient of end-effector	b	15.0542	[kg/s]
Spring constant	k	1300	[N/m]
Gain of gear and motor	$n (= \eta n_g k_T)$	41.8	[1/m]
Gear efficiency	η	0.6	[-]
Gear ratio	n_g	400π	[rad/m]
Torque constant	k_T	0.0554	[Nm/A]
Force from motor	F_m	-	[N]
Force from user	F_u	-	[N]

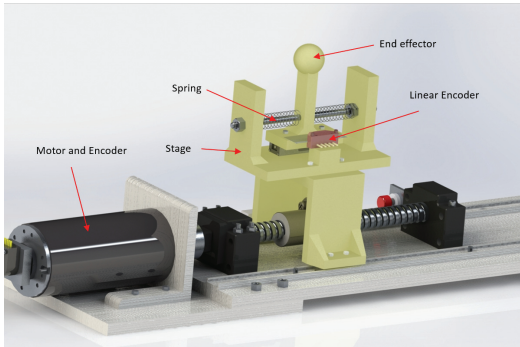


Figure. 6: Hardware design by SolidWorks

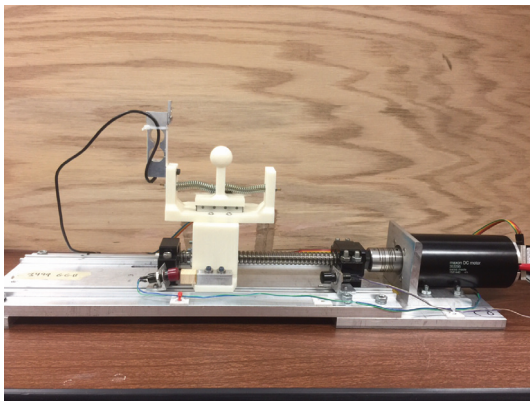


Figure. 7: Haptic apparatus

the advantages of series elasticity over admittance display for haptic rendering. Fig. 8 shows the driving point impedance for both devices attempting to render free motion ($K_{VE} = 0$). One can see the same situation in Fig. 9 which shows the two devices rendering a virtual spring ($K_{VE} = 1000N/m$)

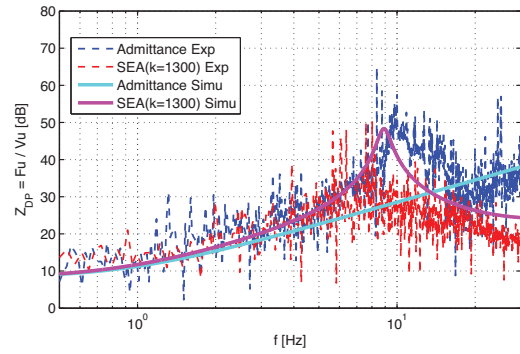


Figure. 8: Comparison between two haptic architectures for free motion ($K_{VE} = 0$) in closed loop ($C_p = 10$)

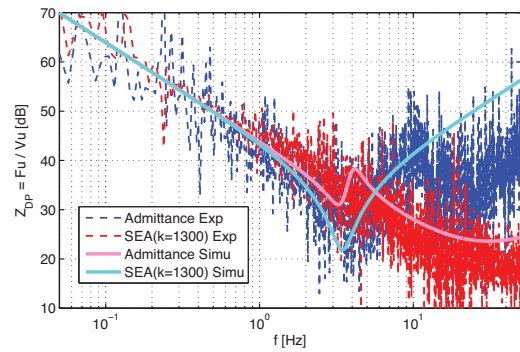


Figure. 9: Comparison between two haptic architectures for Virtual Spring ($K_{VE} = 1000$) in closed loop ($C_p = 2$)

Fig. 10 shows the impedance in open loop ($C_p = 0$). In this figure, the Admittance control device does not fit the ideal model primarily because of the effects of Coulomb friction. The stage does not move when an user attempts to backdrive it, in contrast to the SEA end-effector, which lacks the large effective mass and friction.

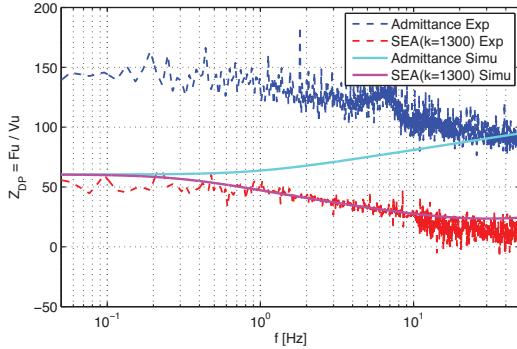


Figure 10: Comparison between two haptic architectures in Open Loop ($C_p = 0$)

As one can see in those figures, the SEA holds an advantage over the admittance control device in terms of back drivability. However, the system with series elasticity can easily be driven unstable, as was already apparent from its the model with a relative degree of 4 in Eq. 13. Thus we take up the topic of stability in the next section.

5 Coupled Stability Analysis based on Passivity Condition

Our objective is to render an arbitrary virtual environment to the user, but we expect restrictions will be placed to guarantee stability. Margaret researched that time delay gives a constraint for stability in haptic rendering [2]. Colgate and Brown show that the several factor restricts the dynamic range of achievable impedances Z -Width, and that an impedance is achievable if it satisfies a robustness property such as passivity [10]. Only for an impedance control, the necessary and sufficient condition of passivity in sampled-data system is proposed [8]. Here we employ the concept of Z -width and compare the stability of Admittance and SEA architecture.

5.1 Human Impedance Model

The haptic device can be touched by human operator, so generally the stability condition is approached through a concept of passivity. The passivity theorem proves that the passive system is stable even if any other passive system is coupled together. Therefore if the human is assumed as a passive system,

the passivity theorem guarantees the coupled system should be stable. In some case the haptic interface or also teleoperation system is considered as 2-port system which is connected to both the virtual environment and human operator, which can deal with complicated nonlinear virtual environment[3]. However the 2-port passivity gives strict constraint, so the virtual coupling has to used in order to satisfy the condition [4], [5]. In this paper, on the other hand, the virtual environment is decided by a linear model as $F_{VE} = Z_{VE}X$, and then the haptic interface can be seen as 1-port system. The necessary and sufficient condition of passivity for 1 port system is shown in [11],[12] as

1. $Z_{DP}(s)$ has no poles in the right half plane
2. $Z_{DP}(s)$ is positive real.

Actually even in the ideal condition, the SEA device is not even stable according to the virtual environment. Consider the stability of the transfer function Y/F_u . If $b = 0$ is assumed for simplicity, the condition that places the poles of the transfer function in the left-half plane is

$$K_{VE} < \frac{1 + nC_p}{nC_p}k. \quad (18)$$

In general nC_p is set to a large value, thereby the above condition requires the virtual stiffness smaller than physical spring stiffness. The stability of SEA is also discussed in [13],[17], but there is no analysis compared to other haptic architectures from SEA under an fair condition.

In contrast to the SEA device, the admittance control device is totally stable and passive in ideal cases. In force control the force signal is sampled in time and possibly quantized in magnitude as well. The sampling and zero order hold processes, which are part of any sampled-data controller, may have an effect on stability. For both haptic architecture, every data used for feedback is measured with same sampling time and controller includes zero-order hold. Hence we shall rewrite the force F_m as a command to the motor as

$$u = H(s)F_m, \quad H(s) = \frac{1 - e^{-sT}}{sT} \quad (19)$$

where u is a real input derived from motor to haptic device. Here the zero order hold operator is approximated using a first order Padé approximation as

$$H(s) \simeq \frac{1}{\tau s + 1}, \quad \tau = \frac{1}{2}T \quad (20)$$

From this form it is clear that the input includes a time delay of τ .

So we start to think the passivity condition for an admittance control device. The driving point

impedance of admittance control device derives following.

$$\begin{aligned} & \text{Re}(Z_{DP}(j\omega)) \\ &= \frac{(BT^2 - 2MTnC_p)\omega^2 - 2TnC_pZ_{VE} + 4B(nC_p + 1)}{T^2\omega^2 + 4(nC_p + 1)^2}. \end{aligned} \quad (21)$$

and then the passivity condition is derived as

$$C_p \leq \frac{BT}{2nM}, \quad Z_{VE} < \frac{2B(nC_p + 1)}{nC_pT}. \quad (22)$$

Above constraint means the admittance control device can not be passive because generally the value of $BT/(2nM)$ is almost 0. This is because the system has to be a passive even if the human arm impedance has an infinite large value, which is totally inappropriate [11]. Although the human operator can grasp the device strongly and that is considered as a large value of human impedance, the maximum impedance must has a limitation. Therefore, the maximum and minimum human impedance idea [4] is introduced as in Fig. 11.

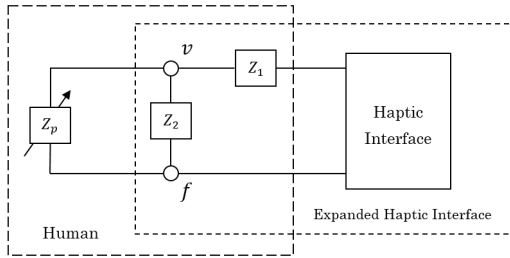


Figure. 11: Human impedance model

In this figure, $Z_1 = Z_{min}$ and $Z_2 = Z_{max} - Z_{min}$ and Z_p are considered a variable impedance. If Z_p is zero, the human impedance is $Z_1 = Z_{min}$ and if Z_p is infinity, the total impedance becomes $Z_2 - Z_1 = Z_{max}$. Here we call the system which includes the haptic interface and Z_1, Z_2 a expanded haptic interface, and its impedance is computed as

$$Z'_{DP} = \left(\frac{1}{Z_2} + \frac{1}{Z_1 + Z_{DP}} \right)^{-1} = \frac{Z_2(Z_1 + Z_{DP})}{Z_1 + Z_2 + Z_{DP}} \quad (23)$$

So now we can consider the coupled stability of an admittance control and SEA device by substituting Z_{DP-Adm}^{CL} or Z_{DP-SEA}^{CL} into eq.(23) and applying the passivity condition. Actually we do not limit the minimum impedance, that is, we use $Z_{min} = 0$ so as to cover cases with no contact. For maximum impedance, we borrow from [4] and set the maximum impedance as

$$Z_{max} = 300 + 1000/s \quad (24)$$

This value was in turn based on previous research [16], which shows that the human arm impedance can be approximated as a spring and damper model. We estimate the human arm impedance in strongly gripping case based on Least-Square technique using the spring and damper model in order to confirm the accuracy of the model. The result is shown in Fig. 12 and it seems the spring and damper model fits almost correctly to the experimental result.

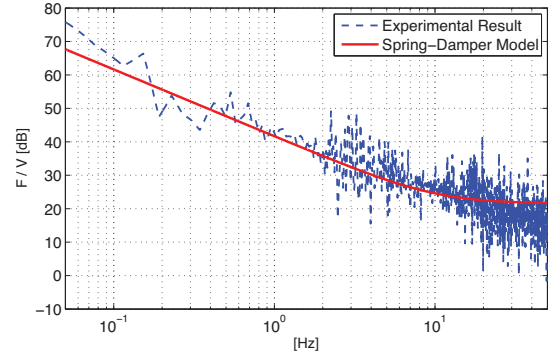


Figure. 12: human arm impedance estimation by spring-damper model

The estimated value is

$$Z_{max-estimated} = 12 + 758/s \quad (25)$$

and it is smaller than the one used in [4]. Because the impedance considered in [16] pertains to the whole arm, whereas our device is only grasped with the fingers, the condition (24) will presumably be conservative for our case.

5.2 Passivity Condition and Z-width

The passivity condition restricts the dynamic range of impedance where the haptic device can render. The range is explicitly calculated in the following.

Note that the control gain range should be decided because of saturation or coulomb friction, so the feedback gain range is set as $C_p = [1, 10]$ for our haptic device. Generally, the haptic interface can be likely unstable when it renders high virtual impedance, hence the maximum virtual stiffness $Max K_{VE}$ which satisfies the passivity condition is discussed.

Substituting eq.(5) into eq.(23) and applying the passivity condition, $Max K_{VE}$ is calculated as in Fig.13.

This figure shows that a smaller gain and a smaller sampling time can achieve the higher virtual impedance and these relation is almost linear. The blank space at the top right area in the figure shows it is impossible to satisfy the passivity condition. From eq.(16), (17), it can be seen the virtual environment can effect to the behavior only at the low frequencies and feedback gain does not affect to it so much. Therefore, in

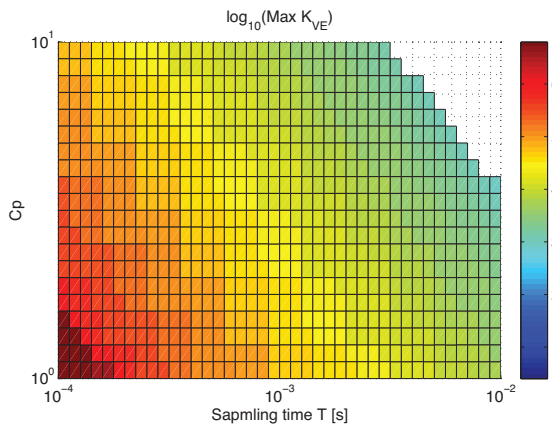


Figure. 13: Maximum virtual stiffness K_{VE} satisfying passivity condition for Admittance control device

order to the highest virtual driving point impedance, we can choose the feedback gain as $C_p = 1$. Our haptic device is connected to a digital controller with sampling time $T = 0.001[s]$, so the maximum virtual stiffness is calculated as 4×10^4 .

For SEA control device, the passivity condition depends on the sampling time T , the feedback gain C_p and physical spring stiffness k . Therefore, at the same way as in admittance, the $Max K_{VE}$ is calculated as in Figure.14~16, which show the case of $T = 0.01, 0.001, 0.0001[s]$ respectively.

Remind that eq.(18) indicates a larger physical stiffness can achieve a larger virtual stiffness, but those figures show there is a limitation for the maximum virtual stiffness even if it has a infinity stiffness spring, that is actually due to the time delay considered in eq.(20). Hence there exists a minimum physical stiffness value which can render a maximum virtual stiffness. With $T = 0.001$, the value is $k = 5.5 \times 10^4$ and achieve $Max K_{VE} = 4 \times 10^4$ at $C_p = 1$. In addition, you can compare the $Max K_{VE}$ of the two haptic architectures in Figure. 17 which shows the $Max K_{VE}$ with varying sampling time T and feedback gain $C_p = 1$.

On the other hand, the minimum virtual impedance is rendered with $Z_{VE} = 0$. From eq.(16), (17), it can be seen a larger feedback gain can achieve the smaller driving point impedance. The minimum virtual impedance can be calculated in the same way of maximum case, and the passivity condition is satisfied for both haptic devices with any feedback gain or any physical spring (actually the passivity condition restricts the control gain as around $C_p < 30$ in both device, so the minimum driving point impedance is limited by the condition). So $Z_{VE} = 0$ and $C_p = 10$ gives the minimum Z_{DP} .

Under those conditions described above, the Z -width is calculated in Figure. 18. Note that since only the behavior at low frequencies is taken into account in order to calculate the Z -width, the calculated mini-

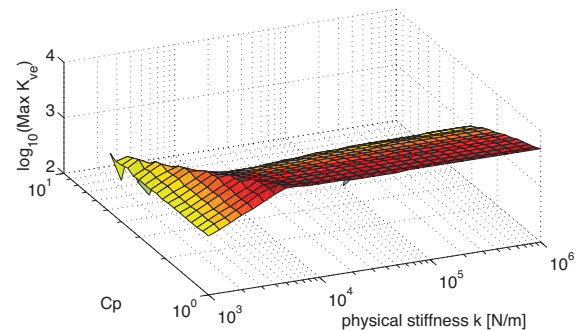


Figure. 14: Maximum virtual stiffness K_{VE} for Series Elastic Actuator control with $T = 10ms$

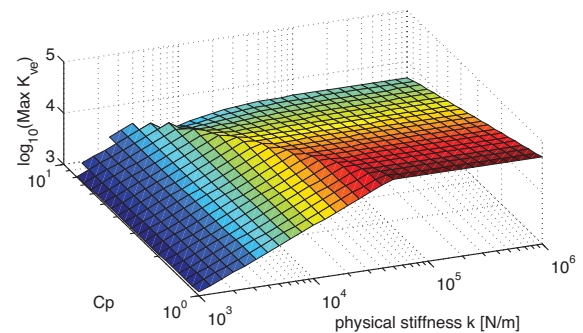


Figure. 15: Maximum virtual stiffness K_{VE} for Series Elastic Actuator control with $T = 1ms$

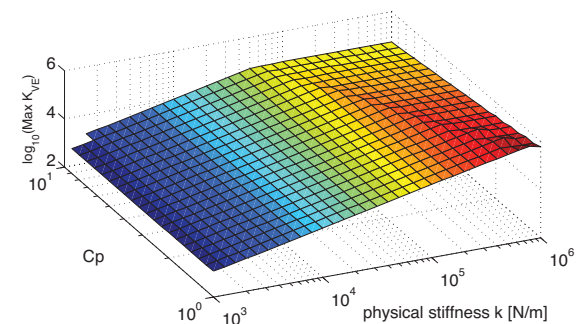


Figure. 16: Maximum virtual stiffness K_{VE} for Series Elastic Actuator control with $T = 0.1ms$

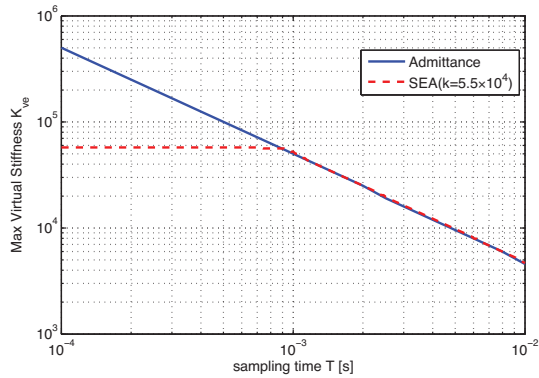


Figure. 17: Comparison of virtual stiffness limitation in Admittance SEA architecture for passivity with sampling time varying

imum driving point impedance in SEA does not show a minimum impedance at high frequencies. From this figure, at frequencies lower than 10Hz, one can see the SEA device with $k = 5.5 \times 10^4$ can render both as high and low driving point impedance as the admittance control device. The SEA device has no longer the advantage of rendering free motion around 20 Hz because of a resonance due to high elasticity, but still has better back drivability at frequencies higher than 100 Hz compared to the admittance control device. The advantage of good back drivability also can be seen also in Figure. 19. Even though a high elastic element make a high driving point impedance at a resonance frequency when a motor is unpowered, the device keep a lower driving impedance than that the admittance control device makes at high frequencies, which means good backdrivability and tolerance for a impact from an external environment.

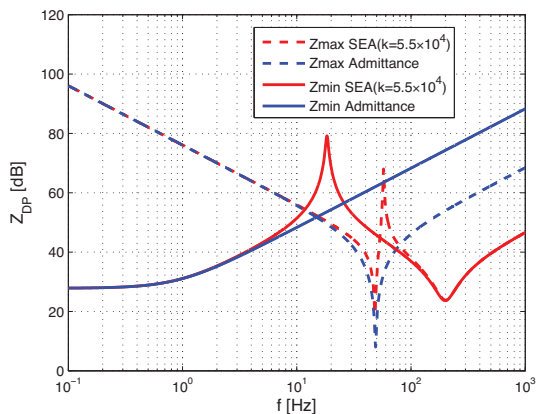


Figure. 18: Maximum and minimum virtual impedance (Z-width)

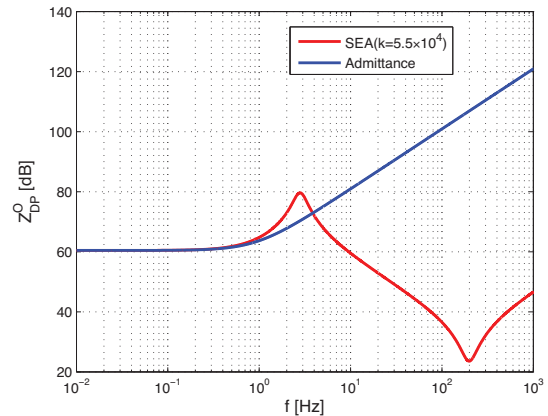


Figure. 19: Driving point impedance in Open loop

6 Conclusion

We focus on the comparison study of two haptic architectures in terms of the driving point impedance which the haptic interface can render. The advantages of series elasticity for haptic interface is shown and validated via simulation and experiment. The coupled analysis based on passivity criteria reveals the performance limit of haptic architectures.

References

- [1] H. W. Bode, "Network Analysis and Feedback Amplifier Design", Princeton: Van Nostrand, (1959)
- [2] Margaret Minsky, Ming Ouh-young, Oliver Steele, "Feeling and Seeing: Issues in Force Display", *Comput. Graphics*, Vol. 24, No. 2, pp. 235-243 (1990)
- [3] Keyvan Hashtrudi-Zaad, Septimiu E. Salcudean, "Analysis of Control Architectures for Teleoperation Systems with Impedance/Admittance Master and Slave Manipulators", *Int. Journal of Robot. Research*, Vol.20, No.6, pp. 419-445 (2001)
- [4] Richard J. Adams and Blake Hannaford, "Control Law Design for Haptic Interface to Virtual Reality", *IEEE Trans. of Control System Technology*, Vol. 10, No.1 (2002)
- [5] Richard J. Adams and Blake Hannaford, "Stable Haptic Interaction with Virtual Environment", *IEEE Trans. on Robot. and Automat.*, Vol. 15, No. 13 (1999)
- [6] Gill A. Pratt and Matthew M. Williamson, "Series Elastic Actuators", *IEEE Intelligent Robots and Systems* Vol. 1 399-406 (1995)

- [7] R. Brent Gillespie and Dongwon Kim and Jacob M. Suchock and Yu Bo and Jeremy D. Brown, "Series elastic for free free-space motion for free" IEEE Haptic Symposium pp. 609-615 (2014)
- [8] J. Edward Colgate and Gerd G. Schenkel, "Passivity of a Class of Sampled-Data Systems: Application to Haptic Interface", Journal of Robotics Systems Vol.14, No.1 pp. 37-44 (1997)
- [9] Marwan Radi, Jordi Artigas, Carsten Preusche, and Hubert Roth "Transparency Measurement of Telepresence Systems", Euro Haptics pp. 766-775 (2008)
- [10] J. E. Colgate and J. M. Brown, "Factors affecting the Z-width of a haptic display", in Proc. IEEE Int. Conf. Robot. Automat. Vol. 4, pp. 3205-3210 (1994)
- [11] Colgate E, Hogan N "An analysis of Contact Instability in Terms of Passive Equivalents" IEEE Int. Conf. on Robot. and Automat., pp. 404-409 (1989)
- [12] Hogan N "On the Stability of Manipulators Performing Contact Tasks", IEEE Journal of Robotics and Automation, No.4, Vol.6 pp. 677-686 (1988)
- [13] Jakob Oblak, Zlatko Matjacic "Design of a series visco-elastic actuator for multi-purpose rehabilitation haptic device", Journal of Neuro Engineering and Rehabilitation, No.8, Vol.3 (2011)
- [14] Jacob Oblak and Zlatko Matjacic, "On the Stability and Passivity of Haptic Device Characterized by a Series Elastic Actuation and Considerable End-Point Mass", IEEE International Conf. on Rehabilitation Robotics pp. 1-5 (2011)
- [15] T. H. Massie and J. K. Salisbury, "The phantom haptic interface: A device for probing virtual objects," in Proceedings of the ASME winter annual meeting, symposium on haptic interfaces for virtual environment and teleoperator systems, Vol. 55, No. 1, pp. 295-300 (1994)
- [16] F. A. Mussa-Ivaldi, N. Hogan, and E. Bizzi, "Neural, mechanical, and geometric factors subserving arm posture in humans," J. Neurosci., Vol. 5, No. 10, pp. 2732-2743, (1985)
- [17] Fabrizio Sergi, Marcia K. O'Malley "On the stability and accuracy of high stiffness rendering in non-backdrivable actuators through series elasticity," Mechtronics, Vol. 26, pp. 54-75, (2015)

NANOFLUIDIC-FLOW-ASSISTED ASSEMBLY (NFAA) OF WELL-DISPERSED PLASMONIC NANOSTRUCTURES INTO NANOSLIT SENSORS

Hiroto Izuoka

Department of Mechanical Science and Engineering, Graduated School of Engineering, Nagoya University
izuoka@ume.mech.nagoya-u.ac.jp

Supervisor: Xiaogan Liang

Department of Mechanical Engineering, University of Michigan
xiaoganl@umich.edu

ABSTRACT

This report shows the novel fabrication of well-dispersed and high-density plasmonic structures for subsequent Localized Surface Plasmon Resonance (LSPR) and Surface-enhanced Raman Scattering (SERS) sensing. We present a method for assembling plasmonic nanostructures into nanoslit sensor structures. This method is termed as Nanofluidic-Flow-Assisted-Assembly (NFAA). In a NFAA process, the addressable nano/microfluidic structures were firstly fabricated into a Si substrate and strongly sealed with a quartz coverslip. Using NFAA, we have demonstrated the coating of Au nanorods (NRs) with length of 80 nm and width of 40 nm, and spherical Au nanoparticles (NPs) with 5 nm diameter into nanoslit sensors. The SEM images displayed that the resulting surface density of AuNRs in 200 nm-deep nanoslit channel was up to ~ 20 NR/ μm^2 . In addition, the density of AuNPs in 80 nm-deep nanoslit channel was estimated up to ~ 200 NP/ μm^2 . Clearly, both showed significantly higher density than current deposition methods.

1. INTRODUCTION

The sensing techniques utilizing plasmonic properties of metallic nanostructures (e.g., nanoparticles (NPs) and nanorods (NRs)) have been a subject of considerable interest lately because of their high detection sensitivity and low limit-of-detection (LOD) [1, 2]. Examples of such plasmonic device principles include

Localized Surface Plasmon Resonance (LSPR) and Surface-enhanced Raman Scattering (SERS) [3-6]. In principle, the both sensing can even achieve single-molecule level detection [1, 2, 3].

The key step to fabricate such plasmonic sensors is the deposition of high-density, well-dispersed metal nanostructures on solid surfaces with integration of well-sealed nano/microfluidic structures. However, the requirements of a high coating density and a good dispersion of metal nanostructures stand in a trade-off to each other. In particular, high coating densities usually result in significant nanostructure aggregation and inter-particle plasmonic coupling, which results in degradation of detection sensitivity and LOD. Because of this reason, the regular coating methods usually generate areal nanostructure densities less than ~ 0.2 NP/ μm^2 [7], which limits the sensitivities. Furthermore, such aggregation of high-density plasmonic nanostructures results in a too poor fabrication yield to enable scale-up biosensor arrays for practical multiplexing sensing applications. New generic nanoplasmonics/ nanofluidics-compatible nanofabrication methods are needed to tackle this challenge.

Here, we present a method for assembling plasmonic nanostructures into nanofluidic sensor structures. This method is termed as Nanofluidic-Flow-Assisted-Assembly

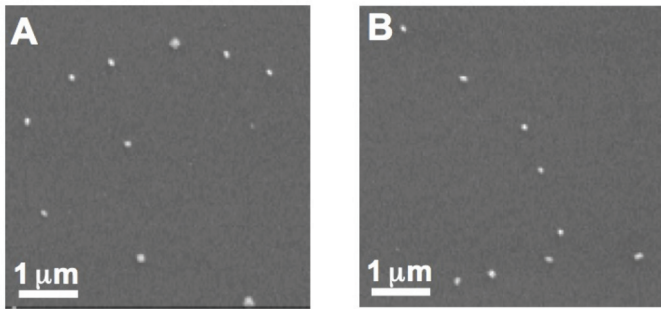


Fig. 1 SEM images of AuNRs on a glass substrate with low density (~ 0.2 NPs/ μm^2) [7]

(NFAA). NFAA utilizes nanofluidic flows with large shear rates to selectively coat high-density, well-dispersed plasmonic nanostructures into sensor areas.

2. EXPERIMENTAL

2.1 Au Colloidal Solution

In this study, two types of colloidal solution of plasmonic nanostructures were used. One is AuNRs with an average length of 80 nm and an average width of 40nm. The other is 5nm spherical AuNPs.

2.2 Fabrication of Nanoslit Devices

The devices were fabricated in the following procedure.

- (1) Using the patterned photoresist as a mask, an etching step is then performed to form microchannels that are used to introduce NPs colloidal solution.
- (2) Similar photolithography and etching are applied again to create a shallow trench (nanoslit channel) on the substrate.
- (3) Sandblasting process is employed from the backside of the wafer to create accessing holes.
- (4) Prior to the bonding process, Si wafer was first treated with Nanostrip solution ($\text{H}_2\text{SO}_4 : \text{H}_2\text{O}_2 : \text{H}_2\text{O} = 18 : 1 : 1$) for 10 min, and then rinsed thoroughly with DI water. Quartz coverslip was cleaned with Buffered Hydrofluoric acid solution (BHF) for 2 min, and then rinsed with DI water. These cleaning processes

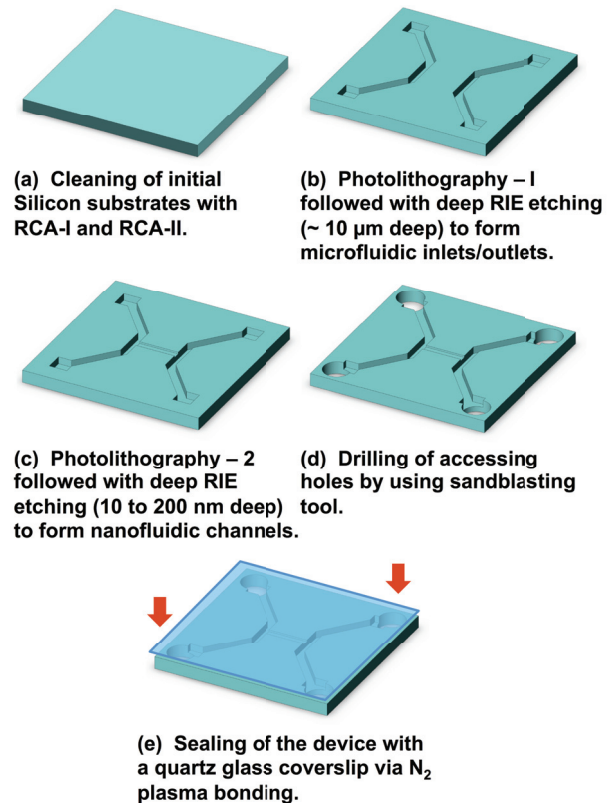


Fig. 2 Fabrication flow chart

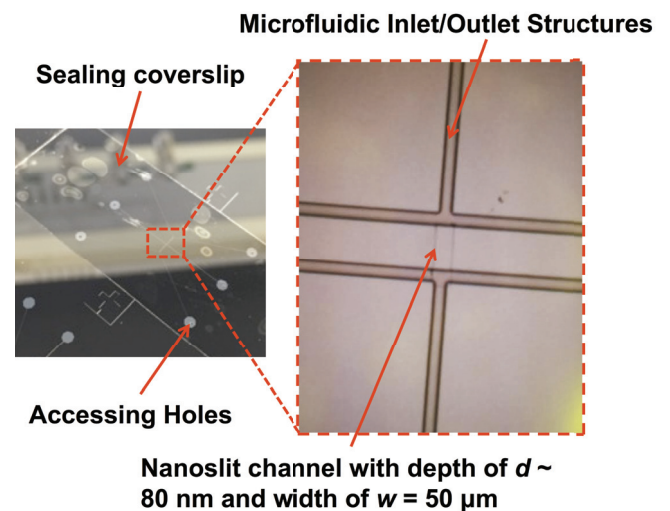


Fig. 3 Optical micrograph of an as-fabricated nano/microfluidic device

remove contaminants on the surface, and make the surface hydrophilic [8].

- (5) Each wafer proceeded to atmospheric N_2 plasma treatment for surface activation for 30 sec at 500 W.

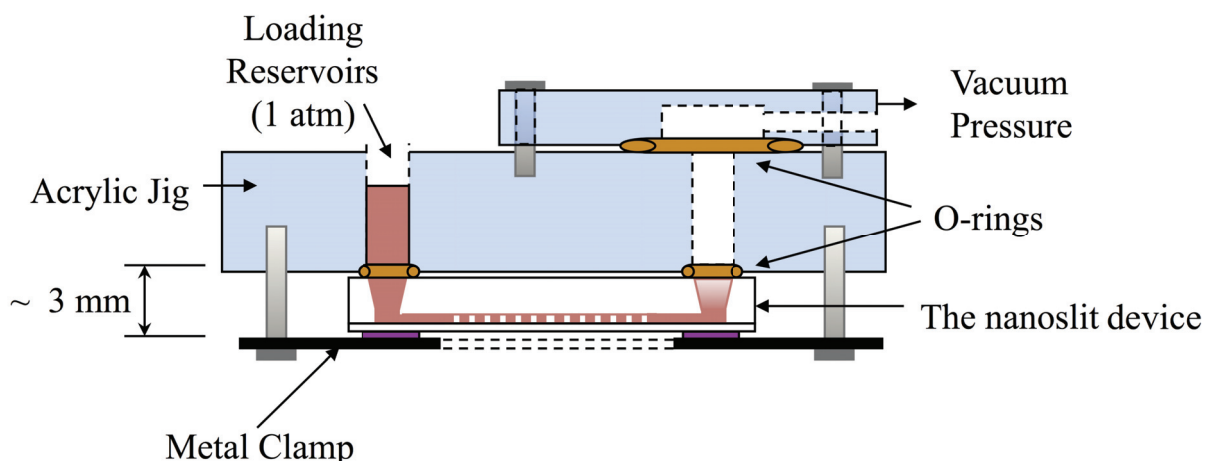


Fig. 4 Schematic illustrate of the NFAA setup

(6) After plasma treatment, the both wafers were brought into contact at room temperature under hand-applied pressure.

Figure. 3 shows the optical micrograph of an as-fabricated nano/microfluidic device for testing NFAA. The devices are composed of 3 inlet/outlet microchannels and 1 nanoslit channel. The sensing area for the following optical measurement, such as LSPR and SERS, is going to be nanoslit channel.

2.3 Nanofluidic-Flow-Assisted-Assembly (NFAA)

Fig. 4 schematically illustrates the NFAA setup. The jig holds Nanoslit device fabricated in the process mentioned in (2.2). For assisting flow through nanoslit channel, the outlet holes were connected to the vacuum chamber. On the other hand, the AuNPs colloidal solution was injected into reservoirs completely covering the inlet holes. As a result, the pressure gradient was created, and the solution in the reservoirs flowed from a region of high pressure (atmospheric pressure) to a region of low pressure (vacuum pressure) through nanoslit channel.

Fig. 5 shows the principle of the NFAA process. A colloidal solution of plasmonic nanostructures is subsequently filled into the nanofluidic structures, and the solution flow is constantly driven by the pressure drop. Within the nanoslit areas, the large shear rate of the nanofluidic flow is important to enable the

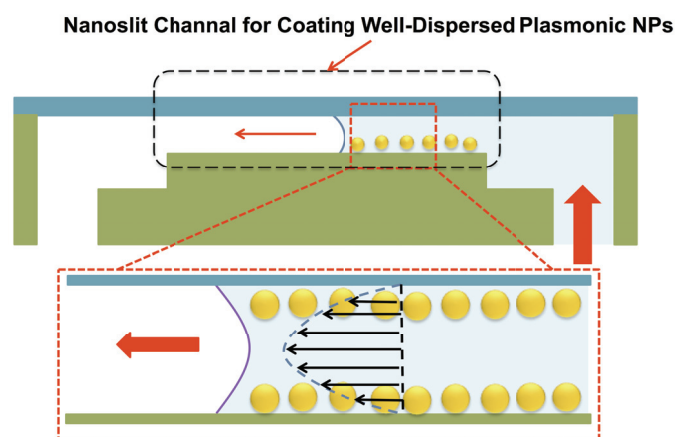


Fig. 5 The principle of Nanofluidic-Flow-Assisted-Assembly (NFAA)

NPs uniformly deposited on the top/bottom surfaces and prevents particle aggregation.

2.4 Scanning Electron Microscope

In order to compare AuNPs/AuNRs coverage and dispersion on the surfaces, the sample surface morphology was characterized using a scanning electron microscope (SEM, SU8000, Hitachi) after the NFAA process.

3. RESULTS AND DISCUSSION

Fig. 6 displays the SEM images of exemplary plasmonic nanostructures coated on the nanoslit channel using NFAA.

3.1 NFAA for 5 nm AuNPs

AuNPs were successfully deposited on the 100 nm-deep nanoslit channel using NFAA. Additionally, the SEM image shows that the

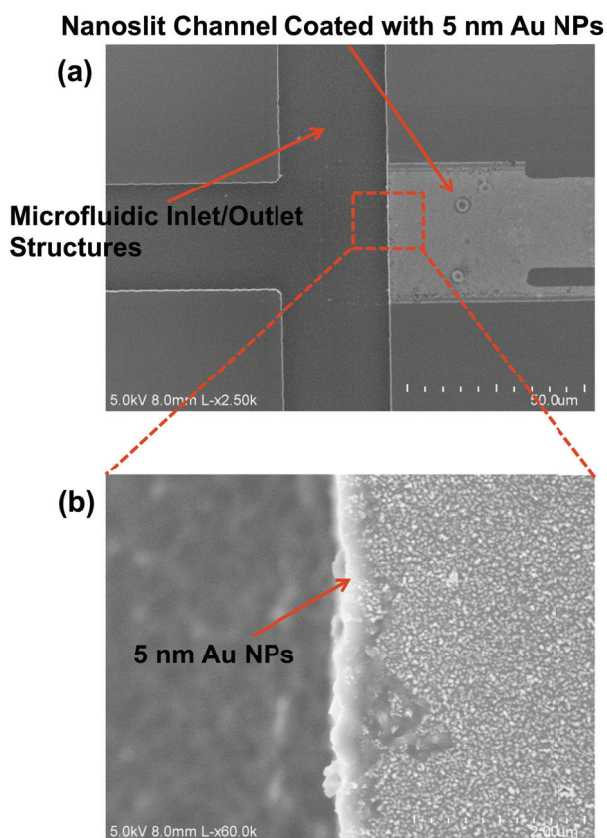


Fig. 6 SEM images of (a) well-dispersed AuNPs on the entire Nanoslit channel, and (b) 5 nm spherical AuNPs with areal density of $\sim 200 \text{ NP}/\mu\text{m}^2$

AuNPs were uniformly coated on the entire channel (Figure. 6a). The estimated areal density of AuNPs is $\sim 200 \text{ NP}/\mu\text{m}^2$ (Figure. 6b).

3.2 NFAA for AuNRs (40 nm×80 nm)

AuNRs were also successfully deposited on the 200 nm-deep nanoslit channel using NFAA. Moreover, the well-dispersed AuNRs on the entire channel were observed in Figure. 7a. Figure. 7b shows that resulting areal density of AuNRs is $\sim 20 \text{ NR}/\mu\text{m}^2$.

The uniform and high-density coating could be achieved for both NPs compared to the conventional coating method. Additional study on the dependence of the resultant plasmonic nanostructure densities/dispersions on the processing parameters such as flow times, nanoslit dimensions, and dimensions of plasmonic nanostructures.

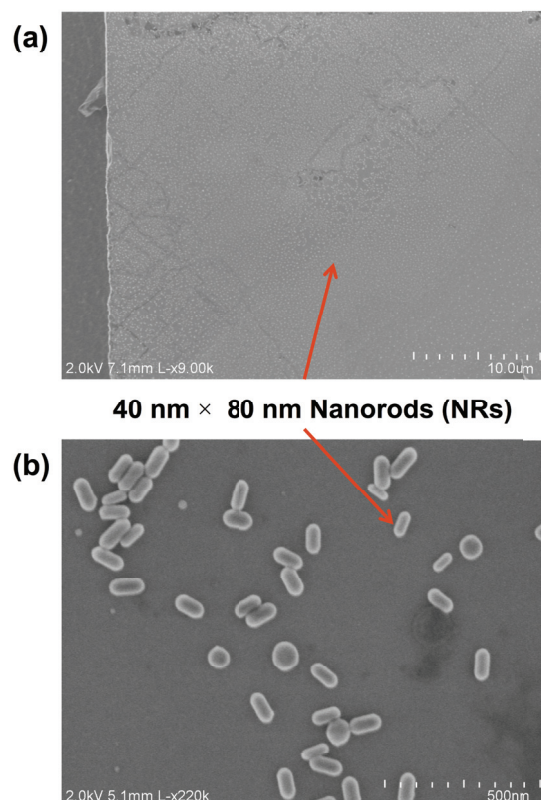


Fig. 7 SEM images of (a) well-dispersed AuNRs on the entire Nanoslit channel, and (b) 40 nm × 80 nm AuNRs with areal density of $\sim 20 \text{ NR}/\mu\text{m}^2$

4. CONCLUSION

In conclusion, we have developed a new coating method for assembling plasmonic structures to incorporate nano/micro structures with plasmonic structures. The coating method was termed as Nanofluidic-Flow-Assisted-Assembly (NFAA). NFAA was demonstrated for two different types of NPs (AuNRs/AuNPs). The NPs coated using NFAA showed uniformly dispersed as well as high-density structures on the entire nanoslit channel. The densities of the plasmonic structures were considerably higher than conventional ways (AuNPs: $\sim 200 \text{ NP}/\mu\text{m}^2$, AuNRs: $\sim 20 \text{ NR}/\mu\text{m}^2$). Therefore, we consider that NFAA is promising way to overcome the fabrication challenge for integration of nanofluidics and plasmonics, which leads to biological and chemical sensor devices for extremely precise detection.

In the further work, the uniformity of plasmonic structures coated using NFAA should be evaluated by quality factor of LSPR

or enhancement factor of SERS. Obviously, this work advanced the critical nanofabrication and enabling new sensing device functionality.

ACKNOWLEDGMENT

I sincerely would like to express my greatest appreciation to Professor Xiaogan Liang for giving such great experience to work in his group at University of Michigan. I also gratefully acknowledge the support from the all members, especially Hongsuk Nam, in Liang's group. Finally, I would like to show my gratitude to JUACEP for the whole support.

REFERENCES

- [1] I. Ament, J. Parasad, A. Henkel, S. Schmachtel, and C. Sonnichsen, *Nano Letters*, 12 (2), 1092-1095 (2012)
- [2] H. Xu, E. J. Bjerneld, M. Kall, and L. Borjesson, *Physical Review Letters*, 83, 4357 (1999)
- [3] B. Oh, N. Huang, W. Chen, J. H. Seo, P. Chen, T. T. Cornell, T. P. Shanley, J. Fu, and K. Kurabayashi, *ACS Nano*, 8 (3), 2667-2676 (2014)
- [4] Yockell-Lelièvre, Helene, Félix Lussier, and J-F. Masson, *The Journal of Physical Chemistry C* 119.51, 28577-28585 (2015)
- [5] Mahmoud, Mahmoud A., and Mostafa A. El-Sayed, *The Journal of Physical Chemistry Letters* 4.9, 1541-1545 (2013)
- [6] Piorek, B. D., Lee, S. J., Santiago, J. G., Moskovits, M., Banerjee, S., & Meinhart, C. D, *Proceedings of the National Academy of Sciences*, 104(48), 18898-18901 (2007)
- [7] Chen, P., Chung, M. T., McHugh, W., Nidetz, R., Li, Y., Fu, J., ... & Kurabayashi, K, *ACS nano*, 9 (4), 4173-4181 (2015)
- [8] Zhang, Xuan Xiong, and Jean-Pierre Raskin. *Microelectromechanical Systems*, Journal o

3D-PRINTING OF POROUS AND SOLID SILICONE STRUCTURES

Michihiro Kanie

Department of Micro-Nano System Engineering, Graduate School of Engineering, Nagoya University
kanie.michihiro@b.mbox.nagoya-u.ac.jp

Supervisor: Albert J. Shih

Department of Mechanical Engineering and Biomedical Engineering, Graduate School of Engineering, University of Michigan
shih@umich.edu

ABSTRACT

The 3D printing of soft materials is not new. However, this technology has not been widely adopted nor developed for mass production of custom products. We have explored various approaches for 3D printing of moisture-cured silicone and conducted tests. First, we investigate the process parameters to squeeze the moisture-cured silicone out of the nozzle and build the 3D-printed parts with minimum void to maximize mechanical properties. Tensile test specimens were printed in 45/135, 90 degrees orientations to the tensile force direction and showed the good mechanical properties of 3D-printed silicone. Second, we created silicone foam by utilizing the coiling phenomenon of the dribbling silicone viscous fluid. Depending on the balance of gravitational, frictional and inertial forces on the descending stream, distinct styles of coiling occur and can be used to build silicone foam blocks. Compression test foam was printed and the results were compared with those of other silicone foams.

Undisclosed

VIBRATION-BASED IDENTIFICATION OF INTERPHASE DAMPING OF FRP

Kiichi Okuno

Graduate School of Engineering, Nagoya University
okuno.kiichi@c.mbox.nagoya-u.ac.jp

Supervisor: Prof. Bogdan Epureanu

Department of Mechanical Engineering, University of Michigan
epureanu@umich.edu

ABSTRACT

Damping is an important parameter for vibration control, fatigue endurance and impact resistance in mechanical and material design. Accurately modeling and identifying the damping properties of fiber-reinforced plastics (FRPs) have not been addressed enough because of the complexity of the multi-physics involved. While fibers and matrix material alone can be characterized more easily, FRPs are much more complex due to interphase properties, fiber orientation, and volume fraction. Current methods to model FRP vibrations are inefficient, cumbersome or often inaccurate especially because of the interphase effects. This paper presents an alternative method to model and identify interphase characteristics and the resulting damping. The approach is demonstrated for beams of longitudinal FRPs, and could be applied to any unidirectional FRP with simple modifications. First, bending vibration phenomena of longitudinal FRP are modeled theoretically for the hypothetical case where there is no interphase debonding or friction. This takes into account the mechanical properties of each material and the volume fraction of fiber. High fidelity simulations are used to validate the theoretical approach. Second, friction-type damping in the interphase region is added to the validated theoretical model. Third, vibration tests are conducted using a composite called bamboo reinforced LDPE with four different volume fractions. Experimental forced response functions are used together with the theoretical model to identify the damping properties of the interphase region as the damping properties of bamboo fibers alone and of LDPE alone are available. This allows the identification of as-manufactured microscopic characteristics through simple macroscopic measurements, which enables a more accurate modeling of FRPs, rapid mechanical design, and material development.

Undisclosed

Physical Aging of Star-shaped Polymer Nanocomposites

Ryo Yamaguchi

Department of Mechanical Science and Engineering, Graduate School of Engineering, Nagoya University
r.yamaguchi@ume.mech.nagoya-u.ac.jp

Supervisor: Peter F. Green

Department of Materials Science and Engineering, Graduate School of Engineering, University of Michigan
pfgreen@umich.edu

ABSTRACT

The physical aging occurs in all glass materials. We investigated the effects of grafted gold nanoparticles on the glass transition temperature and the physical aging of star-shaped polystyrene (SPS) thin films (h : 25 ~ 240 nm) by spectroscopic ellipsometry. Au(2)PS₂₉ nanocomposites films showed different properties from linear polystyrene nanocomposites films which is reported so far. The glass transition temperature (T_g) of these films was independent of weight fraction of grafted gold nanoparticles (c_p). On the other hand, the physical aging rate (β) was shown to speed up with increasing c_p . Furthermore, this phenomenon was apparently observed in the thinner films. We also showed the temperature dependence of physical aging rate. When we decrease or increase ΔT_a ($= T_{age} - T_g$) from $\Delta T_a \approx 35$ °C, the physical aging rate of pure SPS decreases rapidly compared with that of Au(2)PS₂₉_5.0 wt.%.

Undisclosed

EFFECTS OF MICROPORES ON PSEUDOCAPACITIVE CHARGE STORAGE IN VANADIUM NITRIDES

Shintaro Oyama

Department of Mechanical Science and Engineering, Graduate School of Engineering, Nagoya University
oyama@ume.mech.nagoya-u.ac.jp

Supervisor: Prof. Levi Thompson

Department of Chemical Engineering, University of Michigan
lth@umich.edu

ABSTRACT

To understand the effect of micropores on the pseudocapacitive behaviour of Vanadium Nitride (VN), we synthesized and characterized five samples of VN which exhibited phase purity, individual pore size distributions and surface area. The electrochemical performance of these materials was explored in 0.1 mol/L H₂SO₄ and 0.1 mol/L KOH electrolytes. The higher surface area VN was observed to exhibit the higher gravimetric capacitance. Next, we introduced a new parameter, S_{micro}/S_{BET} , a measure of the micropores to total surface area, and we found that the areal specific capacitance of these materials had a linear relationship with S_{micro}/S_{BET} in basic electrolytes. This finding demonstrated that micropores have a higher contribution in the total specific capacitance of VN.

1. INTRODUCTION

Supercapacitors, also called electrochemical capacitors, are a kind of charge storage device, remarkably higher charge storage than electrolytic capacitors because of a much larger surface area as well as, extra storage through the electric double layer and pseudocapacitance phenomena. Supercapacitors currently bridge the gap between conventional batteries and electrolytic capacitors^[1] (Fig. 1). They are expected to be applied in a wider range of fields than so seen before, for instance, in electric vehicles and in combination with renewable energy source.

The major advantages of supercapacitors over lithium-ion batteries, which are the main stream battery storage type at the moment, are short charge times, long cycle lives, high specific power and wider usable temperature ranges.^[3] Supercapacitors do not need any chemical reactions to charge, and therefore their lifetimes are longer. However, supercapacitors possess low specific energies, linear discharge voltage, high self-discharge, low cell voltages, high self-discharge, low cell voltage and high costs per watt.^[3]

Electrochemical energy storage has been applied to various energy storage requirements, for instance, the energy grid, transportation and portable electronics. Many such applications demand not only high power density but also high energy density. Therefore, in recent years, there

have been many reports describing research efforts to increase the energy density of supercapacitors.

Early-transition-metal carbides/nitrides have been hold potential for electrode materials,^{[5][6]} because of low cost, high conductivity and high accessible surface area.^[7] Using early-transition-metal carbides/nitrides is expected to enhance charge storage in supercapacitors through pseudocapacitance. VN has been reported to exhibited as high a capacitance as 1340 Fg⁻¹ in aqueous electrolytes,^[8] making VN a potential material for supercapacitor' electrodes.

Despite several research efforts being put towards supercapacitor materials in recent years, their pseudocapacitive storage mechanisms are still not well understood. Thompson et al. revealed that the amount of adsorbing H⁺ and OH⁻ species occurs mostly in micropores in MoN and VN. This indicated that small pores (micropore, pore size is < 2 nm) were more active than mesopores (pore size 2 to 50 nm) and macropores (pore size > 50 nm); however, these reports have not been confirmed anywhere in the literature. To the best of our knowledge, there are no reports in the literature describing effects of the pore size distribution of VN on electrochemical properties of VN.

Then, purpose of this research is to reveal the effect of

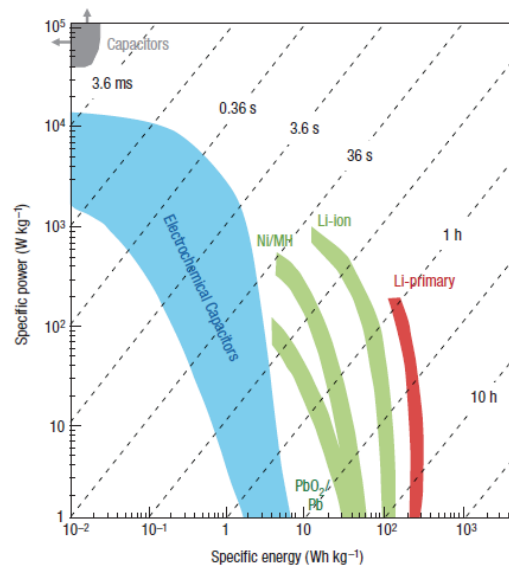


Fig. 1 Specific power against specific energy for various electrical energy storage devices^[1]

micropores of VN on electrode capacitance. To this end, we synthesized VN materials with different pore size distributions by varying the synthesis conditions. And I correlated these to electrochemical performance.

2. EXPERIMENTAL METHOD

2.1 MATERIAL SYNTHESIS

High-surface-area nitrides were prepared from V_2O_5 (Alfa Aesar, US) via a temperature-programmed reaction (TPR) method with NH_3 (Cryogenic Gases). Anhydrous NH_3 (Cryogenic Gases) was used as the reaction gas for the nitrides. V_2O_5 was first crushed and sieved to retain particles with sizes between 125 and 250 μm . The particles were supported on a quartz-wool plug in a quartz-tube reactor. In this report, we made VN under five different reaction conditions. The reaction conditions used to synthesis VN are listed in Table 1. After synthesis, the materials were quenched to room temperature, then passivated using a flowing mixture of 1 % O_2/He (Cryogenic Gases) for 5 hours to form an oxygen-rich protective layer that prevents bulk oxidation of the material when exposed to air.

2.2 PHYSICAL CHARACTERIZATION

The physical surface areas and pore size distributions of the passivated materials were determined by N_2 physisorption using a Micrometrics ASAP2020 analyzer. The Brunauer-Emmett-Teller (BET), Barrett-Joiner-Helenda (BJH) and Harvoth-Kawasoe methods were used to determine the surface areas, the pore size distributions in the region from 2 nm to 200 nm and from 0.3 nm to 2nm, respectively. Prior to analysis, the materials were degassed under vacuum conditions at 350 $^{\circ}C$ for 5 hours. The materials were characterized by X-ray diffraction (XRD) using a Rigaku Miniflex Diffractometer with $Cu K\alpha$ ($\lambda=0.15404$ nm) source. The XRD was carried out at a scan rate of 5.0 $^{\circ} min^{-1}$ with a step size of 0.1 $^{\circ}$ over a 2θ range of 10 to 90 $^{\circ}$. The JADE 10.0 software was used for peak identification.

2.3 ELECTROCHEMICAL CHARACTERIZATION

The electrochemical properties were determined using cyclic voltammetry (CV). The CVs were collected using 0.1 mol dm^{-3} H_2SO_4 (99.999 %, Sigma Aldrich) or 0.1 mol dm^{-3} KOH (Alfa Aesar, Reagent Grade, US) as electrolytes. The experiments were performed using a three-electrode glass cell with an Autolab PGSTAT302N potentiostat (Metrohm, US). The working electrode was made by slurry-coating the materials onto Ti foil substrates (99.97 %, Alfa Aesar, 0.127 nm thickness, US). The slurry was produced by mixing the as-prepared VN (92 wt%) with carbon black (5 wt% Super PLI, TIMCAL) and polyvinylidene fluoride (10 wt%, Kynar) in N-methylpyrrolidone solvent (99.98 %, Alfa Aesar, US). The approximate coated area on the Ti foil was 1 cm^2 . The coated foil was dried under vacuum at 80 $^{\circ}C$ for 8 hours.

A flowing stream of N_2 (99.998 % with an oxygen trap, US) was bubbled through the aqueous electrolytes for at least 30 min before the CV experiments and maintained as a blanket over the solution during the experiments in order to eliminate oxygen exposure. A Pt plate (99.99 %, Alfa Aesar, US) was used as the counter electrode (CE), and $Hg/HgSO_4$ (Sat. K_2SO_4 , Radiometer Analytical, France) and Hg/HgO (0.1 mol dm^{-3} KOH , Radiometer Analytical, France) were used as reference electrodes for the acid and base electrolytes, respectively. The specific capacitances, C , were estimated by integrating the area under the cyclic voltammogram according to^[9]:

$$C = \frac{\int_{V_{cathodic}}^{V_{anodic}} i dV}{mv(V_{anodic} - V_{cathodic})} \quad (1)$$

where i is the current, V_{anodic} is the anodic limit, $V_{cathodic}$ is the cathodic limit, m is the mass of active material and v is the voltage scan rate.

The stable operating voltage windows were determined by cycling the materials in 0.1 mol dm^{-3} H_2SO_4 and 0.1 mol dm^{-3} KOH electrolytic solutions, at 2 mVs^{-1} . The voltage window was expanded from the Open Circuit Voltage (OCV) to more negative and positive voltages in increments of 100 mV until the material showed evidence of irreversible reactions or catalysis (e.g. H_2 or O_2 evolution).

3. RESULTS

3.1 PHYSICAL PROPERTIES

3.1.1 Synthesis conditions and phase purity

We examined five samples of VN. Synthesis conditions are showed in Table 1. The number after three alphabets in those materials name means their own surface area (m^2g^{-1}) measured by BET. XRD was used to confirm the materials had reacted with NH_3 completely, in other words, they were phase pure, as evidenced by the absence of oxide peaks.

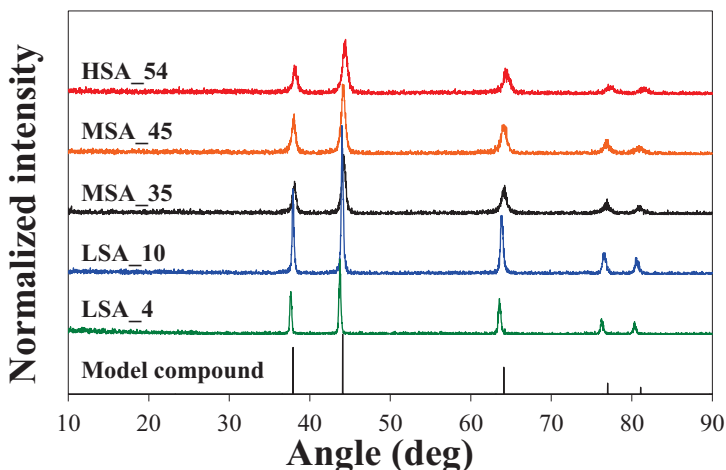


Fig. 2 XRD spectrum of model compound and using materials

Table 1 Synthesis conditions of using materials

Condition	Mass (g)	Flow Rate (ml min ⁻¹)	Spe. flow rate (ml min ⁻¹ g ⁻¹)	Heating Rate β ₁ (°C min ⁻¹)	Temperature T ₁ (°C)	Heating Rate β ₂ (°C min ⁻¹)	Temperature T ₂ (°C)	Heating Rate β ₃ (°C min ⁻¹)	Temperature T ₃ (°C)	Soak time (min)
HSA_54	0.2	2000	10000	-	-	-	-	0.80	650	0
MSA_45	0.4	1730	4325	3.61	350	0.67	450	1.66	700	60
MSA_35	0.4	1200	3000	5.00	350	5.00	450	5.00	750	60
LSA_10	0.5	400	1333	-	-	-	-	15.0	800	480
LSA_4	0.6	300	500	-	-	-	-	20.0	850	720

However, only in the case of LSA_4, we used a different XRD machine (Rigaku Rotating Anode) with a different λ setting, because the normal XRD machine (Rigaku Miniflex Diffractometer) had been down.

3.1.2 Pore size distribution

The pore size distributions of the five materials are shown below in Figures 3, 4 and 5. Fig. 3, Fig.4 and Fig.5 show distributions from 0.5 to 200 nm, 5 to 200 nm and 0.5 to 2 nm, respectively. However, micropore analysis of LSA_4 was not done. Table 2 shows the crystallite sizes, particle sizes, average pore sizes and micropore surface areas of these materials. Micropore surface areas were estimated by

$$S_{micro} (m^2/g) = \frac{V_{micro} (cm^3/g)}{d_{micro} (nm)} \quad (2)$$

where S_{micro} is micropore surface area, V_{micro} is the micropore volume and d_{micro} is the average micropore size. These were obtained through the Harvoth-Kawasoie method. Crystallite sizes were obtained by XRD. Particle sizes, average pore sizes and surface areas were obtained by BET.

As seen from Fig. 3, 4 and 5 mesopore and macropore distributions of HAS_54, MSA_35 and LSA_4 are different. Table 2 shows that average pore sizes of these materials are completely different. From Table 1 and Table 2, high specific flow rate, low heating rate, low final temperature (T_3) and short soak time produced VN with high surface areas.

Table 2 Materials properties

Material	Crystallite size (nm)	Particle size (nm)	Total Surface area (m ² g ⁻¹)	Micropore surface area (m ² g ⁻¹)	Average pore size (nm)
HSA_54	11.6	111	53.8	30.9	10.0
MSA_45	14.8	134	44.7	26.8	14.0
MSA_35	16.0	172	34.9	21.0	15.0
LSA_10	38.4	587	10.2	7.17	44.4
LSA_4	39.4	1641	3.65	2.78	56.4

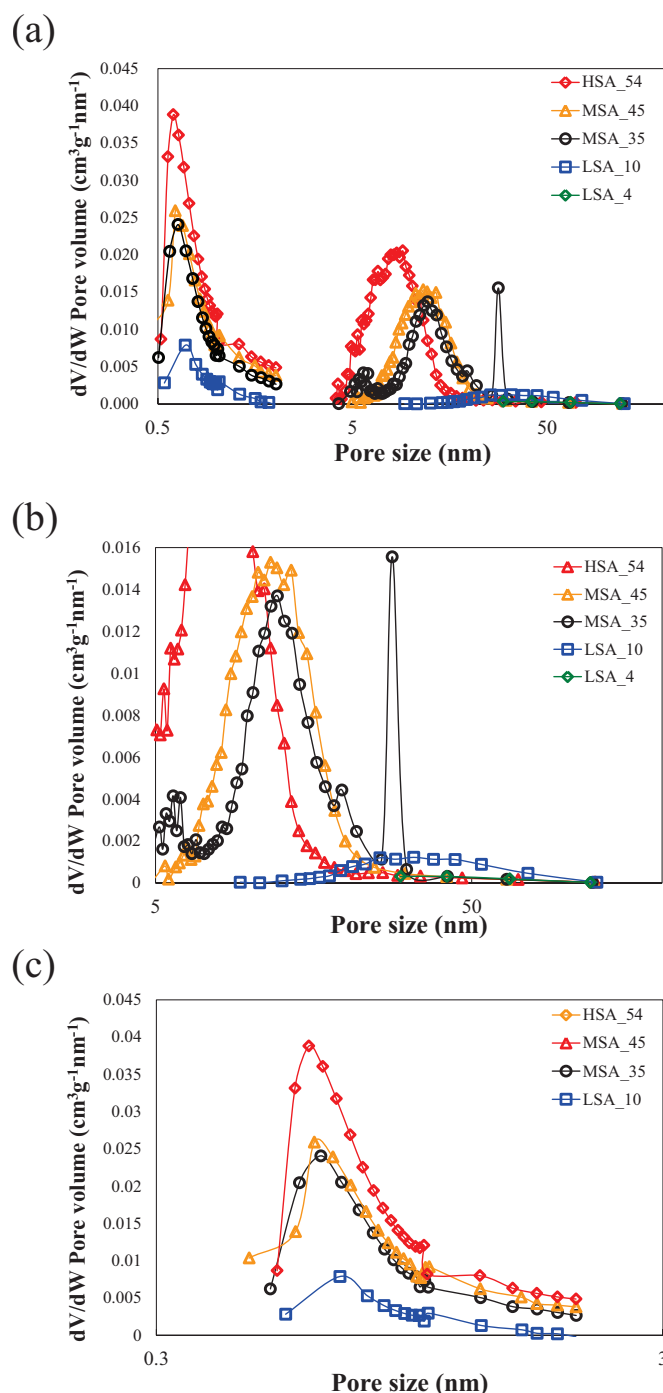


Fig. 3 Pore size distribution (a) whole pore size distribution, (b) expanded from 5 to 50 nm and (c) from 0.3 to 3 nm

3.2 ELECTROCHEMICAL PROPERTIES

Fig. 4 shows cyclic voltammograms, as well as capacitance and areal specific capacitance as a function of the scan rate in both acidic and basic electrolytes. Figs. 4 (c-f), are divided into three regimes for 2 mV/s to 10 mV/s, 20 mV/s to 200 mV/s and 500 mV/s to 2000 mV/s scan rates, namely the total capacitance region, transport limitation region and cell resistance region, respectively.

In basic electrolyte, voltage windows of all samples were 1 V (Fig. 4(b)), and the higher surface areas the materials showed, the larger the respective CV areas and the gravimetric capacitance of these materials. The areal

specific capacitances of HSA_54, MSA_45, MSA_35 and LSA_10 were comparable, but they were not comparable with that of LSA_10 (Fig.4 (f)), which had a different tendency and much higher specific capacitance than others.

In acidic electrolytes, the voltage windows of HSA_54, MSA_45 and MSA_35 were 1.0 V, but that of LSA_10 and LSA_4 were shrunk to 0.8 V and 0.9 V, respectively (Fig. 4 (a)). In terms of CV area the higher the surface area the VN showed, the higher the CV area measured. And the areal specific capacitance of LSA_10 and LSA_4 dramatically changed (Fig. 4 (e)).

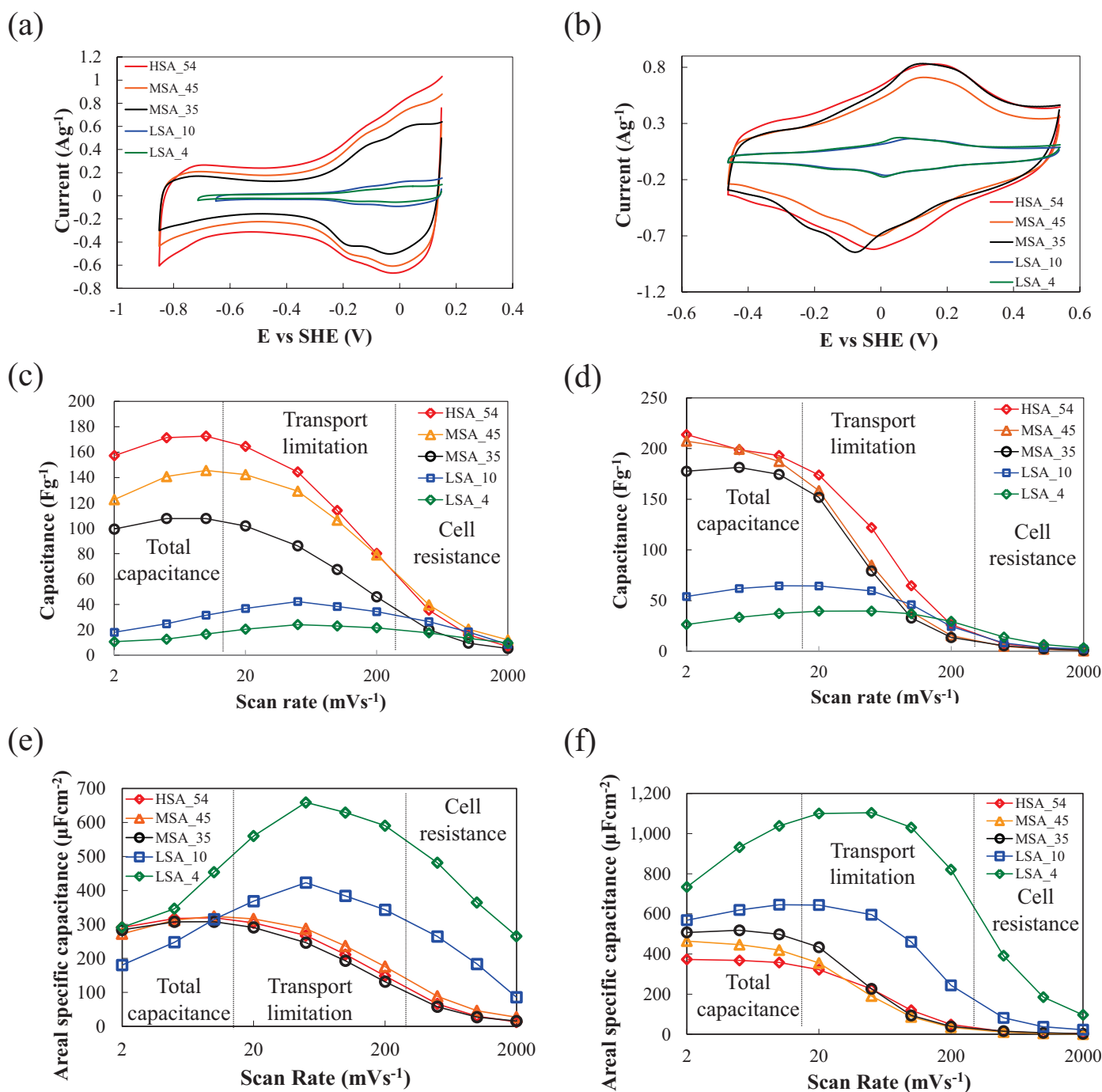


Fig. 4 Cyclic voltammogram (a) in acid and (b) in base, gravimetric capacitance (c) in acid and (d) in base and areal specific capacitance vs scan rate (e) in acid and (f) in base.

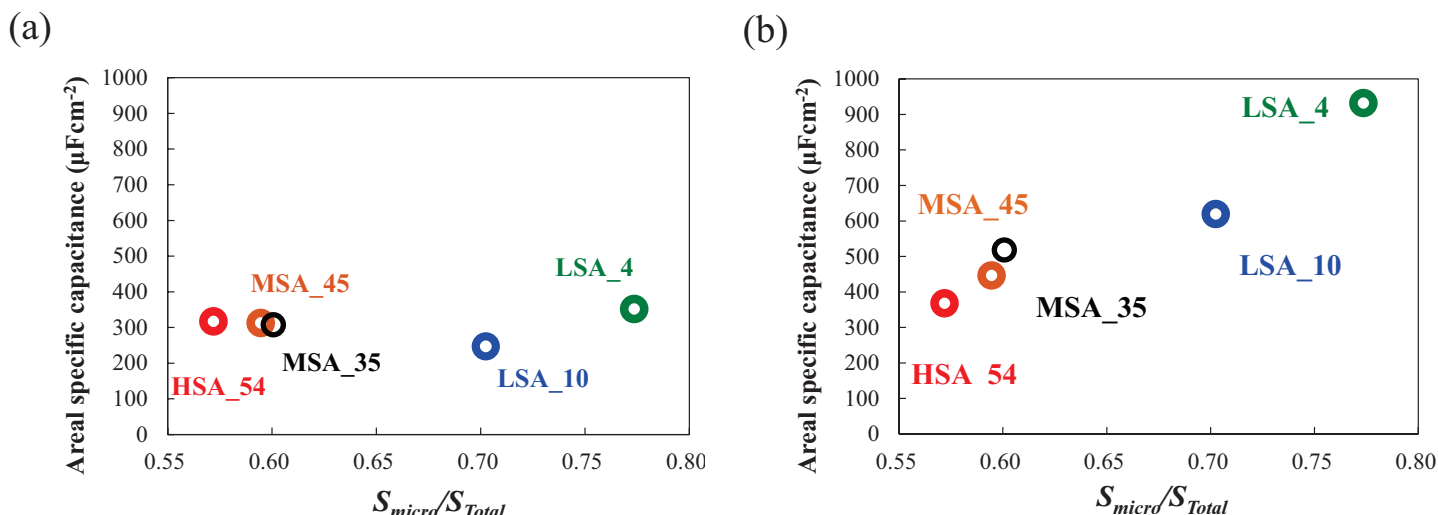


Fig. 5 Areal specific capacitance as a function of S_{micro}/S_{BET} (a) in acid and (b) in base at 5 mV/s scan rate

4. DISCUSSION

4.1 PHYSICAL PROPERTIES OF LSA_4

We were not able to get a pore size distribution in the micropore region by Harvorth-Kawasoie method because the machine for that measurement had been down.

And from Fig. 2, the XRD peaks of LSA_4 were slightly shifted to lower angles (about from 0.25 to 0.60 deg) due to an instrumental error between two XRD machines. So, XRD for LSA_4 needs to be re-done using a Rigaku Miniflex Diffractometer.

4.2 ELECTROCHEMICAL BEHAVIOUR

As seen from Fig. 4 (e), areal specific capacitance behaviour of LSA_10 and LSA_4 in acidic electrolytes is dramatically changed. It could be due to different surface morphology, but we didn't do any surface morphology measurement or observation. So, we need to redo electrochemistry about these materials and examine these materials' surface morphology.

4.3 EFFECTS OF MICROPORES ON PSEUDOCAPACITIVE CHARGE STORAGE

To consider the effect of micropores on pseudocapacitive charge storage in vanadium nitride, we introduce a new parameter, S_{micro}/S_M . S_{micro} is the micropores surface area of each material, which is same as in Equation (2). S_M is the rest of surface area of each material except for micropores surface area. This parameter is a measure of the percentage of micropore surface areas to mesopores and macropores surface areas.

Fig.5 shows areal specific capacitance as a function of S_{micro}/S_{BET} : in basic electrolytes, a linear relationship between areal specific capacitance and S_{micro}/S_{BET} was observed. Hence, in basic electrolytes, the higher the percentage of

micropores in surface area VN had, the larger areal specific capacitance they had.

5. CONCLUSION

We successfully shifted the average pore size of VN from 10 nm to 56 nm by changing the synthesis conditions. Also, by using VN with different pore size distributions, we revealed the linear correlation between the surface areas VN, and the gravimetric capacitance of VN.

Moreover, we showed that a higher percentage of micropores in surface area VN resulted in enhanced areal specific capacitances.

ACKNOWLEDGEMENTS

First, I would like to thank Prof. Levi Thompson for his support, guidance and chance to work in the Thompson Research Group.

I would like to thank my mentor, Abdoulaye Djire. He was a good teacher, a good friend and quite like a good elder brother for me. I really appreciate his guidance and kindness.

Next, I would also like to thank Tapiwa Mushove, Wei-Chung Wen and Jee-Jay Chen for their help.

And I would also like to thank Thompson group members for their kind help and advices.

And I appreciate my supervisor, Prof. Noritsugu Umehara, for allowing me to join this program.

Finally, I would like to thank JUACEP for the financial support and for giving me this precious opportunity.

REFERENCES

- [1] Patrice. S, Yury. G, Materials for electrochemical capacitors, Nature Materials, Vol.7, pp. 845-854 (2008).
- [2] Masanori. N, Present Status and Future Prospect on Electric Double-Layer Capacitors, http://www.fdk.co.jp/cyber-j/pi_technical09.html (available on Web).

- [3] Battery University, "How does a Supercapacitor Work?" http://batteryuniversity.com/learn/article/whats_the_role_of_the_supercapacitor (available on Web).
- [5] A. Djire et al., Charge-Storage Mechanisms in Nanostructured Carbides and Nitrides for Energy Storage, 227th ECS Meeting (2015). [6] Ali Izadi-N et al., Extracting the full potential of single-walled carbon nanotubes as durable supercapacitor electrodes operable at 4 V with high power and energy density, *Advanced Materials*, No. 22, pp. 235–241 (2010).
- [7] Priyanka.P, Investigation of charge-storage mechanism of early-transition-metal nitride and carbides as electrodes for electrochemical capacitors, Thesis of Ph.D, University of Michigan (2013).
- [8] Daiwan Choi et al., Fast and reversible surface redox reaction in nanocrystalline vanadium nitride supercapacitors, *Advanced Materials*, No.18, pp. 1178-1182 (2006).
- [9] B. E. Conway, *Electrochemical Supercapacitors*, Kluwer Academic/ Plenum Publishers (1999).

MICRO/NANO SENSING TECHNIQUE ON DIAMOND TIP USING MICROWAVE

Takahiro Hatano

Department of Mechanical Science and Engineering, Graduate School of Engineering, Nagoya University
hatano.takahiro@g.mbox.nagoya-u.ac.jp

Supervisor: Prof. Xiaochun Li

Department of Mechanical and Aerospace Engineering, Graduate School of University of California, Los Angeles
xcli@seas.ucla.edu

ABSTRACT

Single point diamond turning (SPDT) is a kind of turning process with diamond tool and key technology for rapid prototyping. SPDT enables us to get low surface roughness, and its roughness is a few nano meters. However even if turning condition is same, finished surface changes a little for the difference of the condition on diamond tip. Thus, new sensing technique is needed in order to obtain the data on diamond tool. In this investigation, new sensing technique of temperature and strain on diamond tip using frequency shift of microwave is suggested. When ion implanted into diamond tip reflects irradiated microwave, the frequency of microwave shifts. By measuring the frequency shift, we can monitor the conditions on diamond tip such as temperature and strain.

1. INTRODUCTION

The hardness of diamond makes it an ideal tool material for high-value, ultra-precision machining and grinding operations that influence a multi-billion dollar industry spanning key societal areas such as healthcare, defense, aerospace and transportation [1]. The main benefits of using diamond tools include the ease of cutting hard-to-machine materials and the ability to generate low surface roughness values on the ensuing workpiece surface [2, 3]. Surface roughness is of great importance for the performance of diamond turned components. For instance in optics, the light dissipation due to scattering will be unacceptable when the surface roughness is larger than a critical value.

Single point diamond turning (SPDT) is a kind of turning process with diamond tool and key technology for rapid prototyping or small volume production of spheres, aspheres, parabolic mirrors, cylinders, conical optics, plano optics, simple toroids and assemblies. Fig. 1 shows process of SPDT and a diamond tool [4]. SPDT enables us to get low surface roughness, and its roughness is a few nano meters. Diamond tip is used on SPDT, and surface roughness is affected by the conditions on diamond tip such as temperature and strain. The temperature and strain aren't

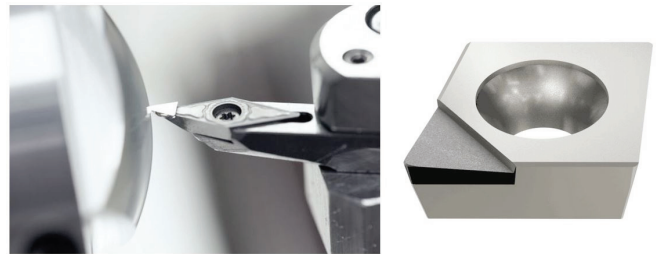


Fig. 1 Process of SPDT / Diamond tool

same during turning process, therefore finished surface becomes rough due to rapid change of temperature and strain on diamond tip. If we could monitor temperature and strain, we can control turning parameter and get smoother surface. To make surface more smoothly, we need a new sensing technique of temperature and strain on diamond tip.

To advance those machining processes, simulations have been performed by a number of research groups, but experimental data from the very close vicinity of the tool-workpiece interface to verify and/or improve simulation parameters are still lacking. Currently available sensors, however, are too large in size to provide valuable information fulfilling a minimum requirement of spatial and temporal resolution. Microsensors produced by thin film techniques known from the semiconductor industry had been investigated [5]. Due to the small dimension, they are able to provide data from the very close vicinity of the insert-workpiece interface. Unfortunately, they are not able to withstand the very harsh conditions such as high temperatures and the severe abrasive wear. To overcome this disadvantage, sensors integrated into the tool or into the workpiece had been researched [5]. They are very small and their size is about 50 micro meters in diameter, which is enable to measure close to the interface. In addition, sensors are protected from the harsh environment. Unfortunately, he measured data may be incorrect because they are destructively inserted. Thus, non-destructively new sensing technique is needed in order to obtain the data on tool or workpiece.

The objective of this research is to study the new sensing technique using frequency shift of microwave. As the first step, it needs to be cleared up that frequency shift is useful to get the information on diamond tip such as temperature and strain.

2. PRINCIPLE

2.1 FREQUENCY SHIFT

Microwave is used for sensing technique. Ion is implanted into diamond tip, and microwave is irradiated to the tip. When implanted ion reflects irradiated microwave, the frequency of microwave shifts. Fig. 2 and 3 show frequency shift is changed linearly due to temperature and strain. Thus, frequency shift is expressed as:

$$\Delta f = \alpha \Delta t + \beta \Delta \varepsilon \quad (1)$$

where f , t and ε are frequency, temperature and strain, respectively, α and β are constant. These relationship has been clarified from the research until now [6]. By measuring the frequency shift, the conditions on diamond tip such as temperature and strain are cleared.

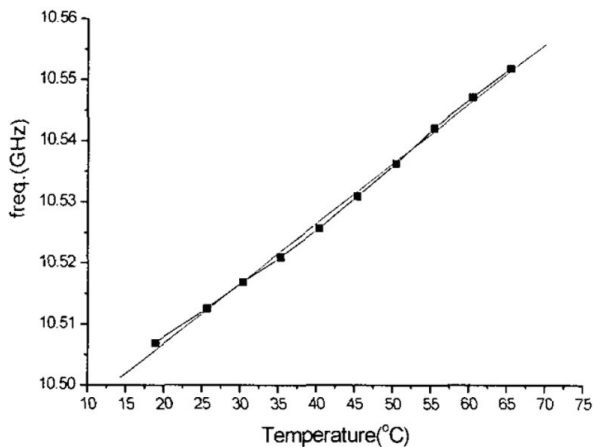


Fig. 2 Relationship between frequency shift and temperature

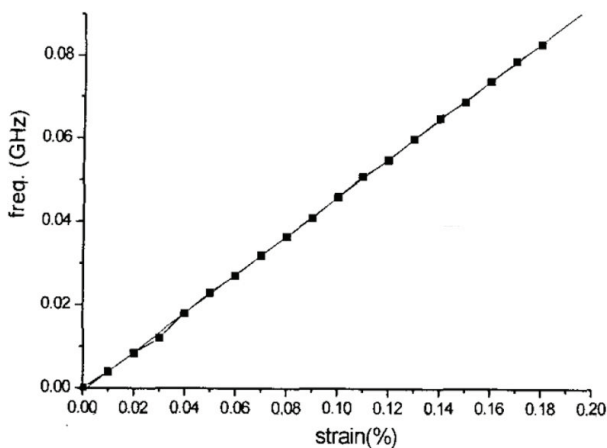


Fig. 3 Relationship between frequency shift and strain

2.2 ION IMPLANTATION

Ion implantation is a materials engineering process by which ions of a material are accelerated in an electrical field and impacted into a solid. Fig. 4 shows the schematic of ion implantation [7]. The kind of ion which is implanted into diamond is also important. In this research, nitrogen and silicon are chosen for ion source. Implanting nitrogen ion creates Nitrogen-Vacancy (NV) center in diamond, and implanting silicon ion creates Silicon-Vacancy (SiV) center in diamond. Fig. 5 shows structure of NV center in diamond and SiV center in diamond, respectively. [8]

NV center in diamond attracts great attention because they serve as a tool in many important applications. NV center might be employed as a sensor operating at the nanoscale. Recently the NV center in diamond has been investigated as promising nanoscale temperature sensors with both high temperature precision and high spatial resolution. Lately, SiV center in diamond has been reported as a good candidate for single-photon source due to its remarkable optical properties and electronic structure [9, 10]. The characteristic of SiV center in diamond and that of NV center in diamond are similar, so SiV center in diamond is expected to have a high temperature precision. That is the reason why silicon is chosen as ion source.

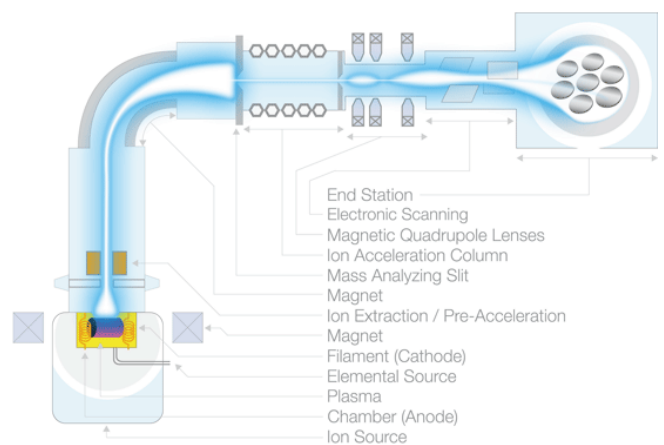


Fig. 4 Ion implantation

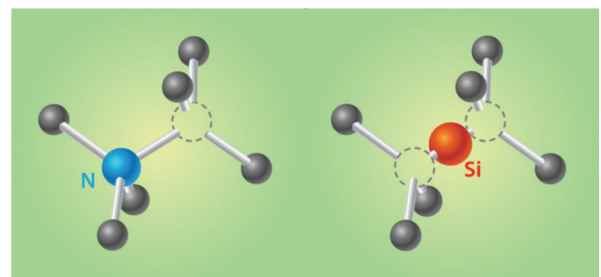


Fig. 5 Structure of NV and SiV

3. EXPERIMENTAL SETTING

3.1 ION IMPLANTATION

NV center in diamond and SiV center in diamond are produced by ion implantation. In the process of ion implantation, two parameters need to be determined: the energy and dosage of the ions. However ion implantation is a violent process. The high energy ion transfers its energy bit by bit to lattice atoms and thus produces a large number of defects. Ion implantation, in short, must always be followed by an annealing process which hopefully will restore a perfect crystal lattice and activate the implanted atoms. In the process of annealing, two parameters also need to be determined: the temperature and time. Table 1 and 2 show the parameter of ion implantation and annealing. High voltage can improve the yield efficiency, whereas it also makes more vacancy defects and larger straggling [11, 12]. Thus there should be an optimal voltage and dose to make the minimal un-demanded defects to NV center ratio. Annealing conditions can impact the NV yield efficiency and reduce the overall crystal damage defects for achieving a good NV yield efficiency. Proper annealing temperature is needed to reduce damage defects for achieving a good NV yield efficiency. Since NV centers are stable below 1600 °C, we can try to take the temperature higher more than 1000 °C to reduce defects more efficiently. Those values on creating SiV center in diamond are simulated with the Stopping and Range of Ions in Matter.

Table 1 NV center in diamond

Substrate material	Diamond
Isotope	14N
Dose [atoms/cm ²]	1 × 10 ¹³
Energy [keV]	15
Tilt angle [degree]	7
Annealing temperature [°C]	1000
Annealing time [min]	10

Table 2 SiV center in diamond

Substrate material	Diamond
Isotope	28Si
Dose [atoms/cm ²]	1 × 10 ¹¹
Energy [MeV]	1.5
Tilt angle [degree]	7
Annealing temperature [°C]	1000
Annealing time [min]	5

3.2 EXPERIMENTAL CONDITION

Firstly I investigated the temperature on diamond tip and the cutting force during turning process in order to approach the experimental condition toward actual turning process. Fig. 6 shows the finite element simulation result of temperature distribution in the cutting tool [13] and Fig. 7 shows the schematic of cutting test process and the distribution of cutting force [5]. Fig. 6 shows that the temperature on the edge of workpiece is about 500 °C to 800 °C. Fig. 7 shows that the cutting force on that is about 200 N. Thus, microwave measurement needs to be conducted under that condition, 500 °C and 200 N.

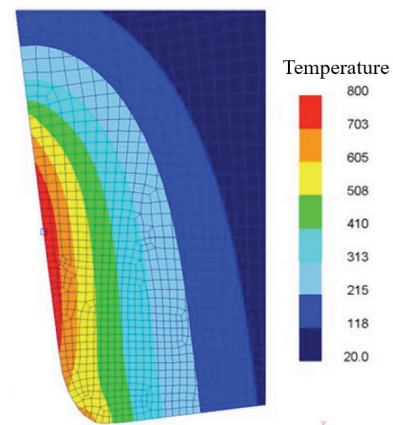


Fig. 6 Distribution of temperature

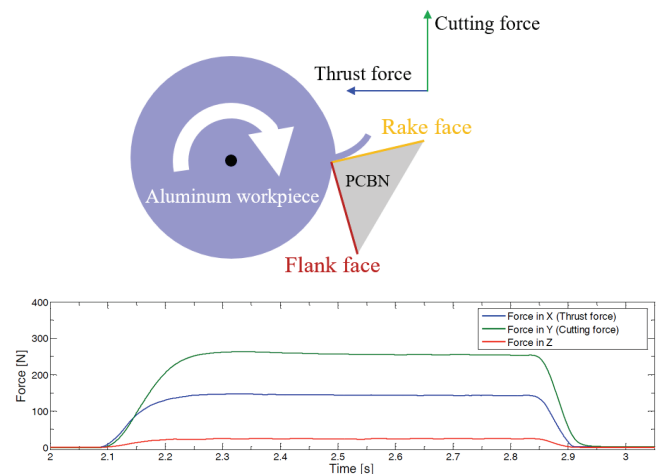


Fig. 7 Distribution of cutting force

4. CONCLUSION

This report shows the best experimental condition of measurement using microwave.

- New sensing technique of temperature and strain on diamond tip using frequency shift of microwave is suggested.

- Nitrogen-Vacancy (NV) center in diamond has high temperature precision and high spatial resolution. Silicon-Vacancy (SiV) center in diamond is expected to have a high temperature precision as with NV center in diamond.
- NV center in diamond and SiV center in diamond are created by ion implantation. The most effective experimental condition of ion implantation is listed on this report.
- In order to approach the experimental condition toward actual turning process, the temperature and cutting force of the tool in turning process is figured out.

New sensing technique on workpiece will be established by making this experiment and analyzing the result.

ACKNOWLEDGEMENTS

I would like to express my sincere gratitude to my supervisor, Professor Xiaochun Li for providing me this precious study opportunity and for giving advices and comments. I would like to thank all members of his laboratory for supporting this study. This study was also supported Japan-US Advanced Collaborative Education Program.

REFERENCES

- [1] Philip J. Smith, Bryan Chu, Eklavya Singh, Philippe Chow, Johnson Samuel, Graphene Oxide Colloidal Suspensions Mitigate Carbon Diffusion during Diamond Turning of Steel, *Journal of Manufacturing Processes*, 17, pp. 41-47 (2015).
- [2] Glabe R., Riemer O., Diamond Machining of Micro-optical Components and Structures, *Proc SPIE*, 7716, pp. 10 (2010).
- [3] Benjamin RJ, Diamond Machining Applications and Capabilities, *Proc SPIE*, 433, pp. 24-31 (1983).
- [4] Verwendung feinsten Diamant- Zerspanungswerkzeuge [Internet]. Viaoptic, <http://www.viaoptic.de/de/inhalk/kompetenzen/prototyping.html>
- [5] Dirk Werschmoeller, Measurement of Transient Tool Internal Temperature Fields by Novel Micro Thin Film Sensors Embedded in Polycrystalline Cubic Boron Nitride Cutting Inserts (2010).
- [6] Il-Bum Kwon, Chi-Yeop Kim, Seok-Beom Cho, Jung-Ju Lee, Temperature Compensation of a Strain Sensing Signal from a Fiber Optic Brillouin Optical Time Domain Analysis Sensor, *Journal of the Optical Society of Korea*, Vol. 7, No. 2, pp. 106-112 (2003).
- [7] Ion implantation [Internet]. Plansee, <http://www.plansee.com/en/products/components/spare-parts-for-ion-implantation.html>
- [8] Guido Burkard, Diamond Spins Shining Bright, *Physics* 7, 131 (2014).
- [9] Rogers L. J. *et al.*, Electronic Structure of the Negatively Charged Silicon-Vacancy Centre in Diamond, *Phys. Rev. B* 89, 235101 (2014).
- [10] Hepp C. *et al.*, Electronic Structure of the Silicon vacancy colour centre in diamond, *Phys. Rev. Lett.* 112, 036405 (2014).
- [11] Pezzagna S., Naydenov B., Jelezko F., Wrachtrup J., Meijer J., *New Journal of Physics*, 12, 065017 (2010).
- [12] Cui Jin-Ming, Chen Xiang-Dong, Fan Le-Le, Generation of Nitrogen-Vacancy Centers in Diamond with Ion Implantation, (2007).
- [13] Yigit Karpas, Predictive Modeling and Optimization in Hard Turning; Investigations of Effects on Cutting Tool Micro-Geometry, *JSME*, 69-686 B, pp. 2305-2312 (2007).

Study of Trapped Air under Shear Flow Using Transparent Single Trench

Yusuke Kasai

Department of Micro Nano Systems Engineering
Graduate School of Engineering, Nagoya University
kasai@biorobotics.mech.nagoya-a.ac.jp

Supervisor: Chang-Jin Kim

Department of Mechanical and Aerospace Engineering,
School of Engineering, University of California, Los Angeles (UCLA)
cjkim@seas.ucla.edu

Abstract

The existence of air trapped in superhydrophobic (SHPo) structures under water is essential for many applications. Following the successful study in static water using transparent single trench samples, I started an experimental study of how flows affect the lifetime of the trapped air. I have designed and constructed a water-circulating system that can control the shear rate on the flows. The state of the trapped air can be observed directly because the sample is transparent. The initial experimental results confirmed the effectiveness of the experimental system under both laminar and turbulent conditions with the shear rate ranging from 6314/s to 28452 /s.

Undisclosed

CHEMICAL VAPOR DEPOSITION OF MoS₂ THIN LAYERS

Taichi Nakao

Department of Micro-Nano Systems Engineering, Graduate School of Engineering, Nagoya University
nakao@ume.mech.nagoya-u.ac.jp

Supervisor: Suneel Kodambaka

Department of Materials Science and Engineering, University of California, Los Angeles
kodambaka@ucla.edu

ABSTRACT

MoS₂ has been one of the most studied 2D layered transition metal dichalcogenides (TMDCs). Monolayer MoS₂ is defined as a semiconductor which has a direct bandgap. Monolayer MoS₂ has many great properties and it's expected to be used in optoelectronic applications. But, the properties of MoS₂ strongly depend on the number of layer. In this research, MoS₂ growth was conducted in thermal Chemical Vapor Deposition (CVD) System by using MoO₃ and Sulfur powders as precursors. We investigated the effect of surface condition of substrate and the flux of MoO₃ to thickness and quality of MoS₂.

1. INTRODUCTION

Graphene, which is a familiar two-dimensional (2D) layered materials, has attracted attention from many materials scientists since the discovery in 2004^[1]. Monolayer graphene has unique and fascinating properties, such as high transparency, high thermal conductivity, high electrical conductivity, high Young's modulus and high specific surface area^{[2][3]}. These outstanding properties give graphene various applications such as Field Effect Transistor (FET)^[4], Single Electron Transistor (SET)^[5] and molecular spin device^[6].

However, the application of graphene in optoelectronics has been limited because most of optoelectronic applications require a bandgap, but graphene doesn't have a bandgap. Researchers tried to create a bandgap in graphene by developing graphene nano-ribbons^[7] and bilayer graphene^[8], but carrier mobility from getting these methods is lower than original graphene.

Recently, these reports about a bandgap of graphene motivated researchers to refocus on other 2D materials with the aim to overcome the weakness of graphene and to broaden its range of application^[9], for example hexagonal boron nitride (hBN)^[10] and molybdenum disulfide (MoS₂)^[11]. Especially, MoS₂ has been one of the most studied 2D layered transition metal dichalcogenides (TMDCs) because monolayer MoS₂ is defined as a semiconductor which has a large intrinsic bandgap of 1.8 eV^[12]. Due to this property, monolayer MoS₂ could complement graphene in optoelectronic applications. Actually a single-layer MoS₂ transistor was developed and

reported in 2011^[13]. Considerable researches have been reported to achieve the synthesis of high quality MoS₂ monolayers which are necessary to develop the electronic devices^{[14][15][16][17]}.

However, most of these efforts have not clarified the precise recipe and mechanism to synthesis of high quality MoS₂. Additionally, the properties of MoS₂ strongly depend on the number of layer^[18]. So, understanding the mechanism and developing the controlled processes about synthesis of MoS₂ are necessary to make MoS₂ used in practical devices.

In this research, we investigated the effect of surface condition of substrate and the flux of MoO₃ to thickness and quality of MoS₂ by changing the distance between substrates and precursors and how to evaporate of MoO₃.

2. EXPERIMENTAL

2.1 Chemical Vapor Deposition System

A schematic of Chemical Vapor Deposition (CVD) System are shown in Figure 1. All MoS₂ growth experiments in this research are carried out in this system. The CVD system consists of furnace, quartz tube, and precursor crucibles. The furnace can control the temperature from room temperature to around 950°C. One end of the tube is connected to gas inlet of argon (Ar) and the other end of tube is connected to mechanical pump. A boat crucible containing MoO₃ powder is made from Alumina (Al₂O₃). This boat crucible is placed at the center of the tube. A cup crucible containing sulfur powder is made from Alumina. This cap crucible is placed at the upstream of the tube. The

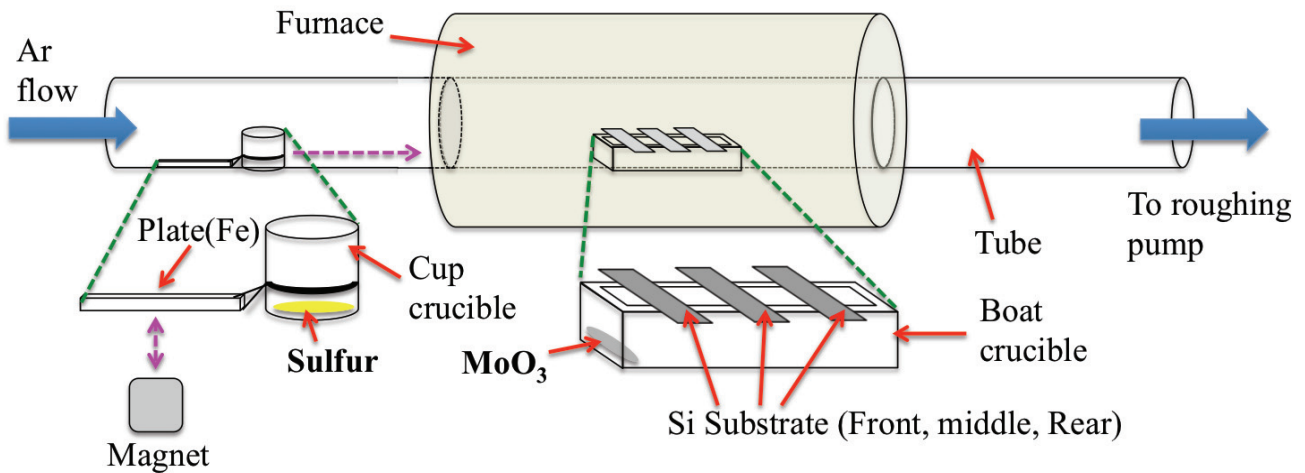


Fig. 1 Schematic of Chemical Vapor Deposition (CVD) System

cup crucible is attached to iron plate and is moved by magnet.

2.2 Substrate and Precursors

Si (001) is used as a substrate in all MoS₂ growth experiments. Si substrates are cleaned with acetone for 10 min and then isopropyl alcohol (IPA) for 10 min by using sonicator. As precursors, MoO₃ (Alfa Aesar© 99.5%) and Sulfur (Sigma-Aldrich© 99.9%) are prepared.

2.3 Deposition condition

At first, three substrates were placed on the top of boat crucible as shown in the Figure 1. These substrates were labeled as Front, Middle and Rear sample from the closest sample to MoO₃ powder. These three substrates on the top of boat crucible contained MoO₃ powder (5 mg) and the cup crucible contained sulfur powder (350 mg) were set in the tube. Substrates and MoO₃ powder were placed at the center inside the furnace. Sulfur powder was placed at the upstream outside the furnace. And then, Ar gas was introduced into the tube and controlled by mass flow controller. The furnace was turned on and furnace temperature is increased to the 400°C and is kept at 400°C for 10 min with Ar flow at 200 sccm. After that, Ar flow changed to 10 sccm and furnace temperature is increased to simultaneously vaporize MoO₃ powder and to heat the substrates. When furnace temperature reaches target temperature (850°C), the cup crucible contained sulfur powder was moved inside the furnace. Sulfur powder was vaporized and transferred to the downstream of the tube by Ar carrier gas at 50 sccm. Sulfur reacts MoO₃ to form MoS₂. Furnace temperature is kept at target temperature for 15 min. After the deposition, the furnace was turned off and was cooled to the room temperature with Ar gas at 50 sccm.

2.4 Scanning Electron Microscopy (SEM)

The morphology of samples was determined by using FEI Nova nano SEM 230. Scanning Electron Microscopy was used to study the morphology and the shapes of MoS₂ triangles.

2.5 Raman Spectroscopy

Raman Spectroscopy is a useful characterization method to demonstrate the structure of layered materials, which changes from 3D bulk structure to 2D layered structure. This method is popularly used to characterize the quality and the layer number of graphene. Similarly, monolayer and a few layer MoS₂ was characterized by using Raman Spectroscopy in 2010^[19]. Generally, two typical Raman peak E_{2g}¹ and A_{1g} are investigated to determine the crystal structure of MoS₂. E_{2g}¹ peak reflects the in-plane vibrational modes of S atoms, whereas A_{1g} peak reflects out-plane vibrational modes of S atoms as shown Fig. 2 (a)^[19]. From bulk MoS₂, E_{2g}¹ and A_{1g} peaks are observed at around 383 cm⁻¹ and 409 cm⁻¹ respectively. From monolayer MoS₂, these two peaks are observed at around 384 cm⁻¹ and 405 cm⁻¹. By changing from bulk MoS₂ to monolayer MoS₂, E_{2g}¹ peak shows a regularly blue-shift (shifting to higher frequency), whereas A_{1g} peak shows an opposite red-shift (shifting to lower frequency). And, the peak frequency difference between E_{2g}¹ and A_{1g} decreases with decreasing the layer number of MoS₂ as shown Fig. 2 (b)^[19]. It decreases from 25 cm⁻¹ to 19 cm⁻¹ with changing from bulk MoS₂ to monolayer MoS₂ respectively as shown Fig. 2 (c)^[19]. Additionally, these two peak intensities increase until four layers with increasing the layer number whereas, for thicker layers than four layers two peak intensities decrease as shown Fig. 2 (d)^[19]. The intensity ratio between E_{2g}¹ and Si substrate is related to the layer number of MoS₂^[20].

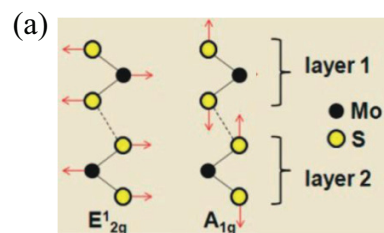


Fig. 2 (a) Schematic of the two typical Raman vibration modes (E_{2g}¹, A_{1g})

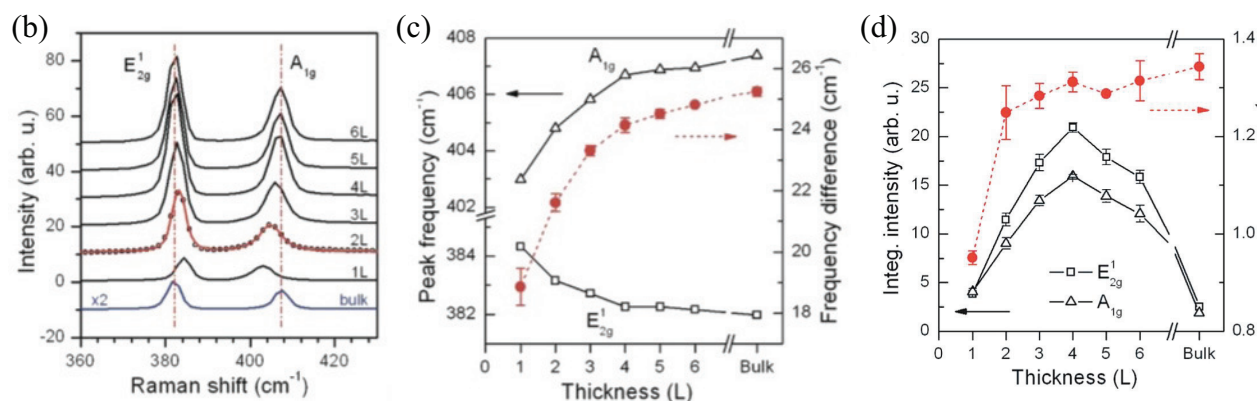


Fig. 2 (b) Raman spectra of monolayer, a few layer and bulk MoS₂. (c) Relationship between frequency difference and thickness of MoS₂. (d) Thickness dependence of integrated intensity and ratio of integrated intensity for the two Raman modes.

In this research, Raman Spectra was taken by using Renishaw In Via Raman Microscope. Generally, when the layer number of MoS₂ is determined by Raman Spectroscopy, the laser wavelength of 532 nm (Green laser) is used. But, in this research, the laser wavelength of 633 nm (Red laser) was used. So, Raman Spectra was shown to prove the existence of MoS₂ and to compare the thickness of MoS₂.

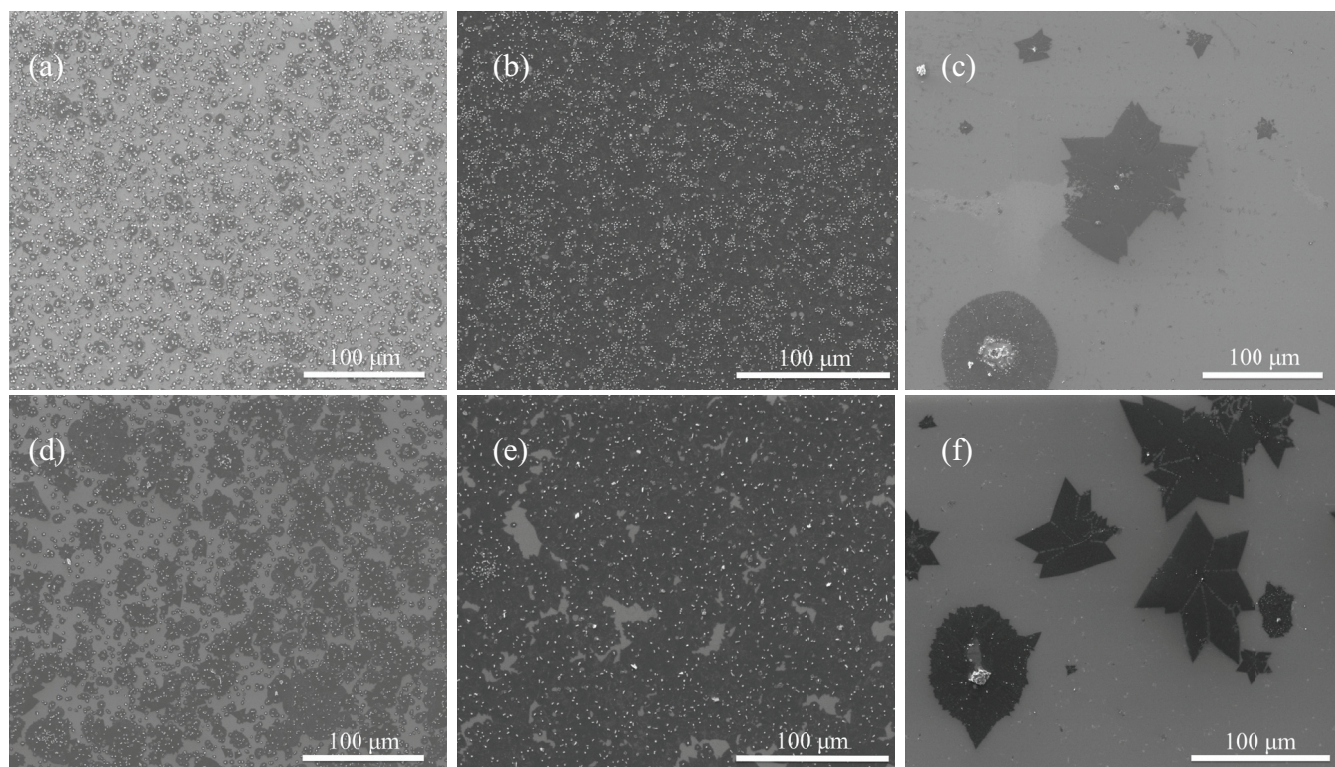
3. RESULTS AND DISCUSSION

3.1 Scanning Electron Microscopy (SEM)

Figure 3 shows SEM images obtained from samples after deposition of MoS₂. Fig. 2(a), (b) and (c) was taken from Front sample which is 0 cm away from MoO₃ powder.

Fig. 3(d), (e) and (f) was taken from Middle sample which is 2 cm away from MoO₃ powder. Fig. 3 (g), (h) and (i) was taken from Rear sample which is 4 cm away from MoO₃ powder. The area where is taken from one sample was classified under inside, border, and wall area as shown in Figure 4.

In Front sample, inside area (Fig. 3 (a)) had many three-dimensional (3D) structures like cubic and cuboid structures. Border area (Fig. 3 (b)) had two-dimensional (2D) structures like layered structures and also had cubic and cuboid structures on layered structures. Wall area (Fig. 3 (c)) had some triangle structures. In Middle sample, inside area (Fig. 3 (d)) had cubic and cuboid structures, and also had layered structure in a part of area.



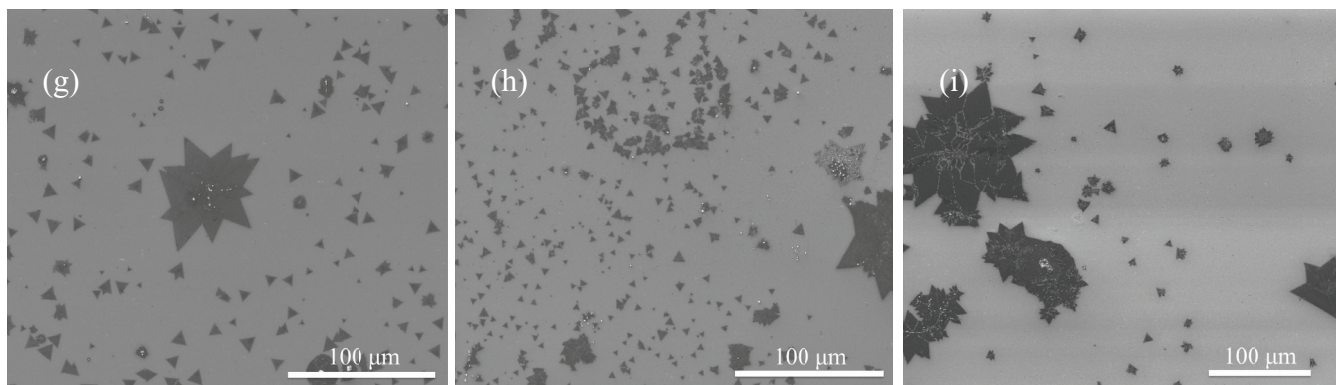


Fig. 3 (a) SEM image in inside area of Front sample. (b) SEM image in border area of Front sample. (c) SEM image in wall area of Front sample. (d) SEM image in inside area of Middle sample. (e) SEM image in border area of Middle sample. (f) SEM image in wall area of Middle sample. (g) SEM image in inside area of Rear sample. (h) SEM image in border area of Rear sample. (i) SEM image in wall area of Rear sample.

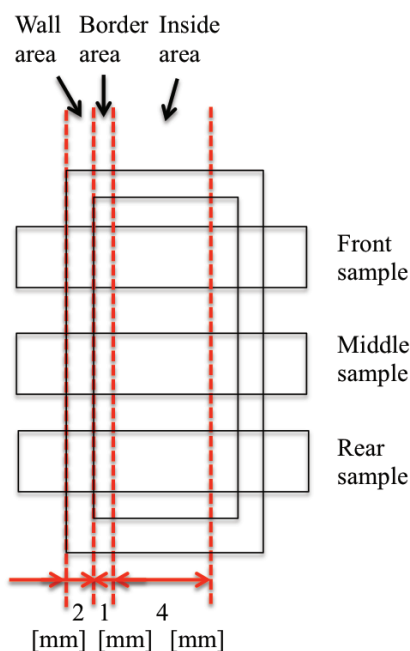


Fig. 4 Classification of area in one sample

Border area (Fig. 2 (e)) had cubic and cuboid structures on layered structure and wall area (Fig. 2 (f)) had some triangle structures same as Front sample. In Rear sample, all area had some triangle structures.

Figure 5 shows SEM images obtained from inside area of Rear sample in different deposition condition from Figure 3. In Fig. 3, MoO_3 powder was placed inside furnace while furnace temperature increases. But in Fig. 5, MoO_3 powder was placed at the upstream outside furnace. When furnace temperature reaches target temperature, MoO_3 powder was moved into the furnace. Other than that, deposition condition was same as shown in experimental section. Even in Rear sample, inside area had 3D structures like cubic and cuboid structures.

Moreover, Figure 6 shows SEM images of typical structures obtained from samples. Fig. 6 (a) shows typical 3D structures like cubic and cuboid structures which are observed in inside area of Front samples, and Rear sample shown in Fig. 5. Fig. 6 (b) shows typical 2D structures like layered structures with 3D structures which are observed in border area of Front and Middle samples, inside area of Middle sample. Fig 6 (c) shows typical triangle structures which are observed in wall area of all samples and all area of Rear sample.

3.2 Raman Spectra

Figure 7 shows Raman Spectra obtained from samples after deposition of MoS_2 . In Fig. 7 (a), three spectra were taken at the cubic and cuboid structure (Front sample), layered structure (Middle sample) and triangle structure (Rear sample) of inside area. Frequency difference between E_{2g}^1 and A_{1g} peaks decreases with going away the distance between precursors and substrates. E_{2g}^1 and A_{1g} peak positions in Front sample were 383 nm^{-1} and 408 nm^{-1} respectively. E_{2g}^1 and A_{1g} peak positions in Middle sample were 383 nm^{-1} and 407 nm^{-1} respectively. E_{2g}^1 and A_{1g} peak positions in Rear sample were 383 nm^{-1} and 405 nm^{-1} respectively.

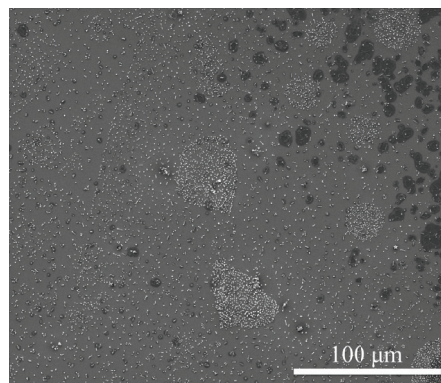


Fig. 5 SEM image at inside area of Rear sample when MoO_3 evaporated rapidly

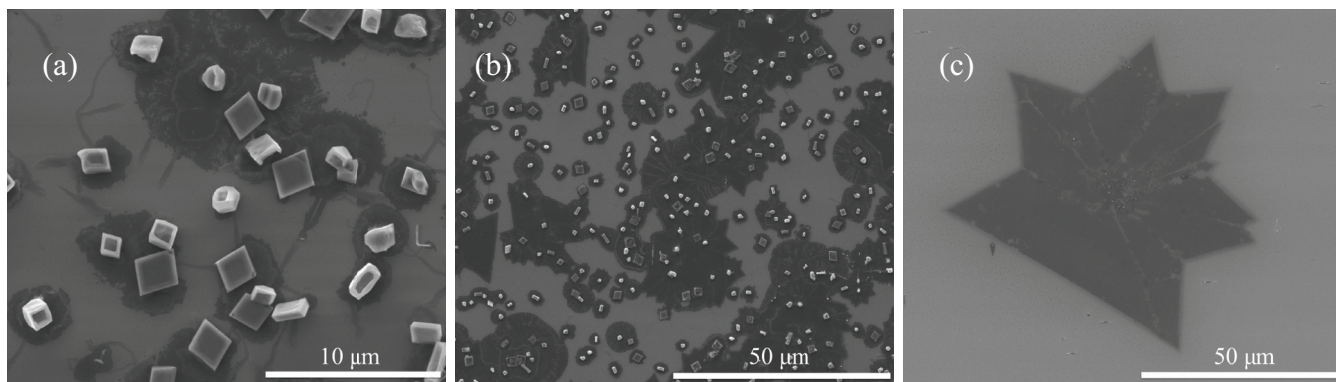


Fig. 6 (a) SEM image of typical cubic and cuboid structures. (b) SEM image of typical layered structures with cubic and cuboid structures. (c) SEM image of typical triangle structures.

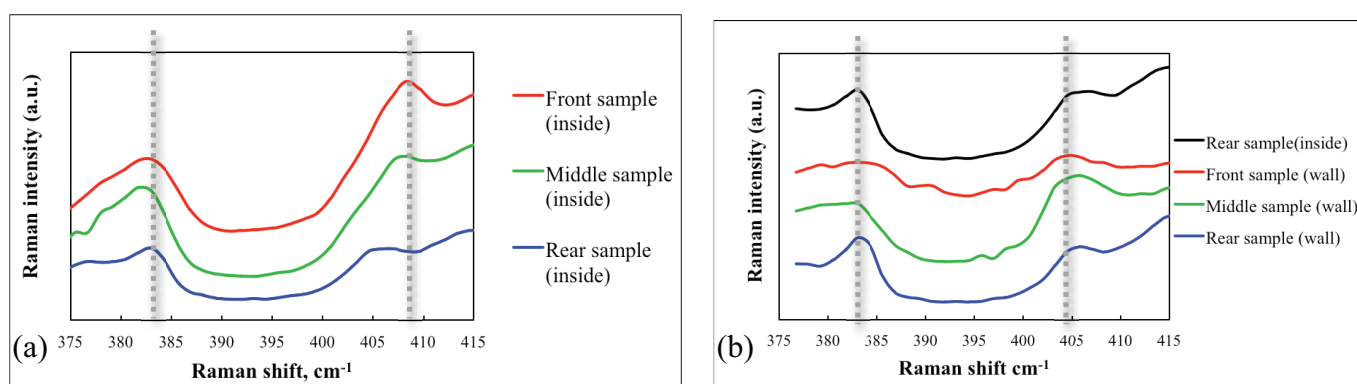


Fig. 7 (a) Raman Spectra at inside area (Front, Middle and Rear samples). (b) Raman Spectra at wall area (Front, Middle and Rear samples)

In Fig.7 (b), three spectra were taken at the triangle structures of wall area (Front, Middle and Rear samples). Frequency difference was independent on the distance. These peak positions were also same as that of Rear sample in Fig. 7 (a).

3.3 The effect of surface condition to the structure of MoS₂

As shown in Fig. 3 (a), (b), (c) and 6, inside area of Front sample had many cubic and cuboid structures. Border area had layered structures with cubic and cuboid structures. Wall area had some triangle structures. I think the reason why the difference of structure is like below. In wall area, MoO₃ vapor flux is limited because the crucible wall blocks to enter MoO₃ vapor into the wall area where is contacted with substrate. In border area, there is step edge between crucible wall and substrate. Step edge makes MoO₃ atoms create the nucleation easily. So, the layered structures are made from step edge.

3.4 The effect of flux of MoO₃ to the thickness of MoS₂

As shown in Fig. 3 (a), (d), (g) and Fig. 7 (a), the thickness of MoS₂ decreases with going away from MoO₃ powder. I think these results are related to the flux of MoO₃ because the flux decreases with decreasing the amount of MoO₃ reached to substrates per time and area. In these results, all conditions except the distance (total pressure, furnace temperature, deposition time and Ar flow) are same. So, the amount of MoO₃ reached to substrates per time and area decreases with going away from MoO₃ powder. Moreover, the thickness of MoS₂ in Fig. 3 (g) is thinner than that in Fig. 5. In condition of Fig. 5, MoO₃ was vaporized more rapidly than the condition of Fig. 3 because MoO₃ powder was placed inside the furnace in all time from room temperature to target temperature at the condition of Fig. 3, whereas MoO₃ powder was moved inside the furnace when the temperature reached to target temperature at the condition of Fig. 5. So, flux of MoO₃ at Fig. 5 is larger than that at Fig. 3.

The results of Front sample reflect the effect of the difference of surface conditions. But, the results of Rear sample are independent on surface conditions. From these results so far, the flux of MoO₃ is very important parameter to synthesize MoS₂ thin layers.

4. CONCLUSION

We demonstrated the synthesis of MoS₂ thin layers in thermal Chemical Vapor Deposition (CVD) System by using MoO₃ and sulfur powders as precursors. We investigated the effects of surface condition of substrate and the distance between MoO₃ powder and substrates to thickness and quality of MoS₂. From these investigations, there was high possibility that the flux of MoO₃ is key parameter to synthesize MoS₂ thin layers. However, flux is related to many other parameters (total pressure, deposition temperature, carrier gas flow). Future work is necessary to find out the more precise recipe or mechanism of MoS₂ synthesis.

ACKNOWLEDGEMENTS

I would like to thank Professor Suneel Kodambaka for giving me an opportunity to study in University of California, Los Angeles. I would like to thank Abbas Ebnonnasir for supporting this research. And I'm grateful to all members in in-situ microscopy laboratory for helping my work. This work was supported by Japan-US Advanced Collaborative Education Program.

REFERENCES

- [1] Novoselov KS, Geim AK, Morozov SV, Jiang D, Zhang Y, Dubonos SV, et al. Electric field effect in atomically thin carbon films. *Science* 306:666-9 (2004).
- [2] Allen MJ, Tung VC, Kaner RB. Honeycomb carbon: a review of graphene. *Chem. Rev.* 110:132-45 (2010).
- [3] Soldano C, Mahmood A, Dujardin E. Production, properties and potential of graphene. *Carbon* 48:2127-50 (2010).
- [4] Y. M. Lin, et al. "100-GHz Transistors from Wafer-Scale Epitaxial Graphene", *Science* 327:662 (2010).
- [5] L. A. Ponomarenko et al. "Chaotic Dirac Billiard in Graphene Quantum Dots", *Science* 320:356-8 (2008).
- [6] M. Ohishi et al. "Spin Injection into a Graphene Thin Film at Room Temperature", *Jpn. J. Appl. Phys* 46:605-7 (2007).
- [7] M. Y. Han et al. "Energy Band-Gap Engineering of Graphene Nanoribbons", *Phys. Rev. Lett.* 206805 (2007).
- [8] Y. Zhang et al. "Direct observation of a widely tunable bandgap in Bilayer graphene", *Nature* 459:820-3 (2009).
- [9] Sheneve Z. B, Shawna M. H, Linyou C, Yi C, Jay A. G, et al. "Progress, Challenges, and Opportunities in Two-Dimensional Materials Beyond Graphene", *ACS Nano* 7:2898-926 (2013)
- [10] A. Nagashima, N. Tejima, Y. Gamou, T. Kawai, and C. Oshirna. "Electronic Structure of Monolayer Hexagonal Boron Nitride Physisorbed on Metal Surfaces", *Phys. Rev. Lett* 75:3918-21 (2007).

- [11] Xiao Li, Hongwei Zhu. "Two-dimensional MoS₂: Properties, preparation, and applications", *Scie. Dire.* 1:33-44 (2015).
- [12] Mak, K. F., Lee, C., Hone, J., Shan, J. & Heinz, T. F. "Atomically thin MoS₂: a new direct-gap semiconductor", *Phys. Rev. Lett.* 105:136805 (2010).
- [13] B. Radisavljevic, A. Radenovic, J. Brivio, V. Giacometti and A. Kis. "Single-layer MoS₂ transistors", *Nature Lett.* 6:147-150 (2011).
- [14] Lee, Y.-H. et al. "Synthesis of Large-Area MoS₂ Atomic Layers with Chemical Vapor Deposition", *Adv. Mater.* 24, 2320–2325 (2012).
- [15] Dumitru D, Dmitry O, Kolyo M, Predrag L, et al. "Large-Area Epitaxial Monolayer MoS₂", *ACS Nano* 9: 4611-20 (2015).
- [16] Lin, Y. C. et al. "Wafer-scale MoS₂ Thin Layers Prepared by MoO₃ Sulfurization", *Nanoscale* 4, 6637–6641 (2012).
- [17] Jaeho J, Sung K. J, Su M. J, et al. "Layer-controlled CVD growth of large-area two-dimensional MoS₂ films", *Nanoscale* 7: 1688-95 (2015).
- [18] Jason K. Ellis, Melissa J. Lucero, and Gustavo E. Scuseria. "The indirect to direct band gap transition in multilayered MoS₂ as predicted by screened hybrid density functional theory", *App. Phys. Lett.* 99:261908 (2011).
- [19] Lee C, Yan H, Brus LE, Heinz TF, Hone J, Ryu S. Anomalous lattice vibrations of single and few-layer MoS₂. *ACS Nano* 4:2695-700 (2010).
- [20] Zhan Y, Liu Z, Najmaei S, Ajayan PM, Lou J. Large-area vapor-phase growth and characterization of MoS₂ atomic layers on a SiO₂ substrate. *Small* 8:966-71 (2012).

PROPERTY REVIEW AND THERMAL CONDUCTIVITY MEASUREMENT ON LUNAR REGOLITH AND REGOLITH SIMULANT

Shogo Okishio

Graduate School of Aerospace Engineering, Nagoya University
okishio@prop2.nuae.nagoya-u.ac.jp

Supervisor: Laurent Pilon

Mechanical and Aerospace Engineering, University of California, Los Angeles
pilon@seas.ucla.edu

ABSTRACT

The properties of lunar regolith and regolith simulant were reviewed by comparing the data from researches. Simultaneously, the property models were reviewed. After reviewing, the thermal conductivity measurement of regolith simulant (FJS-1) was conducted by using the guarded hot plate method, which was originally designed for measuring the thermal conductivity of solid materials. The application of this method to powder materials was challenged, maintaining the basic set up. The results were discussed from the perspective of excluding the effect of air with calculation or of adapting the measurement equipment under a vacuum, since the chosen specimen is mostly used in vacuum conditions. The experimental results appeared with some remaining problems; however, by reconsidering the experimental set up, there is a possibility of archiving powder material measurement by conducting single-sided measurement under the vacuum with the same material and a variety of densities.

1. INTRODUCTION

Recently, more and more lunar explorations have been planned all over the world. Most of the plans attempt to land and spend time on the lunar surface. For example, Japanese space agency JAXA is making plans to launch SELENE-2 and SLIM, Indian Space Research Organization is working on Chandryaan-2, Korea announced to reach the lunar surface by 2020, and European Space Agency has the HERACLES plan for lunar exploration. The most recent landing on the moon—the first in over 40 years—was achieved by China in 2013 with Chang'e 3. The next plans, Chang'e 4 and 5, have already come up. [1]

Also there is a private 30 million dollar competition named Google Lunar Xprize which has taken place since 2007. [2] This competition is about designing and manufacturing the lunar rovers capable of accomplishing

tasks set by the promoter. As necessary requirements, rovers need to travel 500 meters, and transmit back high definition video and images. There are also other bonus tasks as well. Moreover, the competition has announced their determination to launch the lunar rovers from the first and second prize winning teams in 2017. This public movement has played a role in increasing the common people's interest toward the moon.

However, the lunar environment is known to be a very severe one due to its large temperature fluctuation on the surface, which is in a range of -190°C to $+100^{\circ}\text{C}$. Therefore, it is important to understand well the thermal condition of the lunar environment to design and conduct the pre-test on lunar landers and rovers on earth before actually taking them into space. To make testing apparatuses while spacecrafts are on earth, the regolith simulant will be required to model the ground condition of lunar surface. Regolith simulant is made to imitate the lunar soil, which is commonly known as regolith. There are many types of regolith simulant in the world made by various countries.

Thermal conductivity measurements have been conducted on both lunar regolith and regolith simulant over the past 50 years. The apparatus was designed for in-situ measurement and for laboratory measurement as well. However, the regolith has some range of bulk density which seems to effect the thermal conductivity. Thus, thermal conductivity depends on both density and temperature, which makes the ideal measurement difficult. The obtained measurement data varies from research to research and method to method; the best possible way for measuring has not been determined yet.

Generally, thermal conductivity measurement methods can be classified into two types: steady state method and non-steady state method. As a steady state method, there are five basic types for materials with low thermal conductivity. [3] Those are: the guarded hot plate method, the comparative method, radial flow, calorimeter and photometer. All methods are based on Fourier's Law to

obtain the thermal conductivity. As a non-steady state method, there are: the thermal conductivity probe, the transient hot wire, differentiated line-heat source and the composite circular cylinder method. The details on these methods are described in Presley and Christensen (1997). [4] It is normally considered that these are simple, more efficient, better suited for small samples and they have short measurement periods. [3]

Despite the disadvantage of long equilibration times required for each single measurement, the steady state guarded hot plate method was chosen in the experiment for this research. The reason for this choice was that there were no former experiment examples with guarded hot plate on the thermal conductivity measurement of the same powder materials with a variety of densities. The first objective of this research is to organize and compare the data from relative researches and models. This will be useful in understanding the insufficiency of current research on lunar regolith, which has various thermal conductivity values depending on the measurement methods. The second objective is to make a set up for the measurement of powder material with a guarded hot plate. The regolith simulant FJS-1 was chosen as the specimen for the measurement to reveal the density dependence of thermal conductivity in lower temperature range. The reason for this choice is that there are only a few measurement data of FJS-1 thermal conductivity and there is no existing data in the lower temperature range below 20°C.

2. OBJECTS

2.1 Lunar Regolith

Lunar regolith is the name for the particle material which covers the lunar surface. It is a mixture of rock, mineral and glass fragments transformed into a distinctive material by the unique combination of space weathering processes. The main component of lunar regolith is SiO₂. Regolith is the byproduct of various sized meteorites crashing into the lunar surface, leaving relatively small particle sizes. The average particle diameter is 70 μm. The shape is angular because the moon lacks the flowing water and wind that causes rounding in terrestrial sediments. About 380 kg of lunar samples have been returned from the moon by Luna and Apollo missions. Rock and soil represent the samples of the mission site. Detailed description of minerals and lunar samples can be seen in Ref.5. [5]

2.2 Regolith Simulant

Regolith simulants have an artificially controlled component to resemble lunar regolith. Many kinds of regolith simulants are made around the world. For example, there are American simulants called JSC (Johnson Space Center) series, MLS (Minnesota Lunar Simulant) series and NU-LHT series which are developed by NASA, Australian simulant called ALRS-1 (Australian Lunar Regolith

Simulant) and Japanese simulant FJS (Fuji Japanese Simulant) series which are developed by the Japanese company Shimizu Corporation. All simulants are made to mimic the lunar regolith and are used for experimental environments for research on moon. Particle size of regolith upper data and lower data with regolith simulants data are shown in Fig. 1. [6] As it shows, the particle sizes of simulants are set inside the range of obtained data of lunar regolith. The component comparison between Apollo samples and regolith simulants are shown in Table. 1. The shapes of regolith simulants are classified and divided into six types: very angular, angular, sub-angular, sub-rounded, rounded and well rounded. [7] Then the weight percent of each simulant was analyzed. The results of JSC-1A and FJS-1 are shown in Fig. 2. However, there is analysis like this type conducted for the lunar regolith, and it is estimated only glass spherules are likely to be rounded or well rounded. [7] There are other researches about the strength, mechanical properties and grains. Measurement of thermal diffusivity and thermal conductivity of these materials is also important in discussing lunar thermal surface processes.

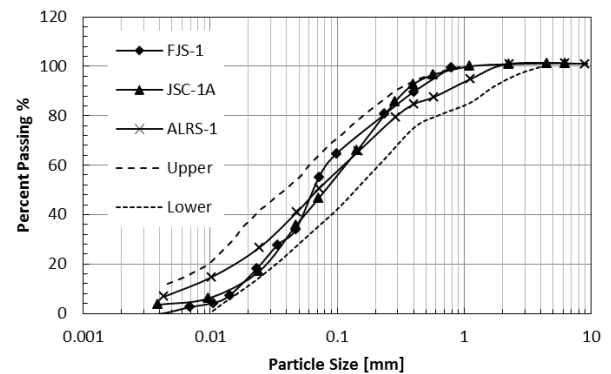


Fig. 1 Particle Distribution

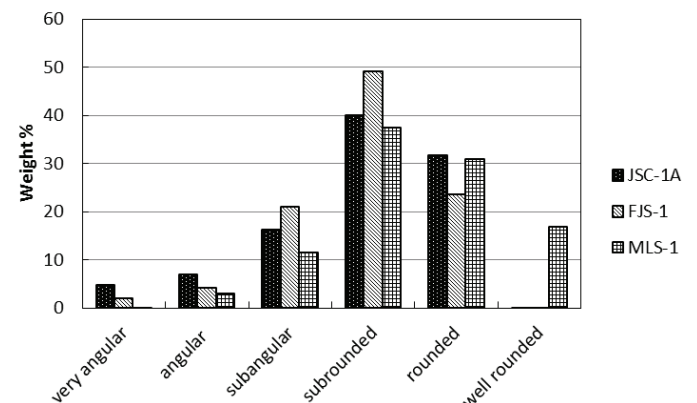


Fig. 2 Particle Shape of Regolith Simulant

Table. 1 Component of Apollo Samples and Regolith Simulant

Component	Lunar Regolith			Regolith Simulant			
	Apollo 11	Apollo 12	Apollo 14	MLS-1	JSC-1	FJS-1	ALRS-1
SiO ₂	42.20	46.2	48.10	43.9	47.7	49.14	42.36
TiO ₂	7.80	3.9	1.70	6.3	1.6	1.91	2.73
Al ₂ O ₃	13.60	12.5	17.40	13.7	15.0	16.23	13.48
Cr ₂ O ₃	0.30	-	0.23	-	0.0	0.00	-
FeO	15.30	19.4	10.40	13.4	7.4	8.30	0
Fe ₂ O ₃	0.00	0	0.00	2.6	3.4	4.77	12.55
MnO	0.20	0.24	0.14	0.2	0.2	0.19	0.18
MgO	7.80	5.70	9.40	6.7	9.0	3.84	10.23
CaO	11.90	11.33	10.70	10.1	10.4	9.13	8.61
Na ₂ O	0.47	0.29	0.70	2.1	2.7	2.75	3.29
K ₂ O	0.16	0.04	0.55	0.2	0.8	1.01	1.49
P ₂ O ₅	0.05	-	0.51	-	-	0.44	0.53
S	0.12	-	-	-	-	0	-
Total	99.90	99.6	99.83	99.2	98.2	97.71	95.45

3. PROPERTIES

The properties of lunar regolith and regolith simulant, for example, density, specific heat, thermal diffusivity and thermal conductivity will be mentioned in details below.

3.1 Density

Bulk densities of Apollo samples were determined from tube volume and weight of the cores inside. Starting from Apollo 11 to Apollo 17, sample name and densities are summarized in Table. 2. [8] The equation for the regolith density depending on the depth has been developed and modified by Mitchell and Houston. [9][10]

$$\rho = \rho_0 + \rho^* \ln(z + 1) \quad (1)$$

Where $\rho_0 = 1.27 \text{ g/cm}^3$, constant $\rho^* = 0.121$ for Apollo 15 and 17, $\rho_0 = 0.80 \text{ g/cm}^3$, constant $\rho^* = 0.225$ for Apollo 15. Character z refers to the depth from the surface in cm. There is another empirical equation from Apollo 15 in-situ density measurement. (Eq. (2)) [11]

$$\rho = 1.89 \times \frac{z + 1.69}{z + 2.9} \quad (2)$$

The characters in the equation represent the same units as the previous equation. ρ [g/cm³] represents density and z [cm] represents the depth from the surface. The plotted data of equations are shown in Fig. 3.

Table. 2 Bulk Densities of Apollo Samples

Sample Name	Bulk Density [g/cm ³]
10004	1.58 ± 0.04
10005	1.70 ± 0.04
12026	1.74
12028	1.97
14210	1.75
15001	2.15
15007	1.66 ± 0.02
15008	1.36 ± 0.05
15009	1.35
15010	1.85 ± 0.06
15011	1.69 ± 0.03

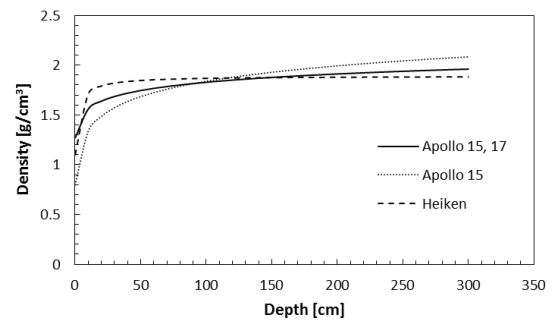


Fig. 3 Density of Lunar Regolith

3.2 Specific Heat

Specific measurements on Apollo samples were conducted by Hemingway in the range of 90-350K. [12] The equation was derived from the measurement results of 14163, 15031, 60601 and 10084, which are soil type samples. These samples showed a similar result despite being from different terrestrials.

$$C_p = -2.3173 \times 10^{-2} + 2.1270 \times 10^{-3} T + 1.5009 \times 10^{-5} T^2 - 7.3699 \times 10^{-8} T^3 + 9.6552 \times 10^{-11} T^4 \quad (3)$$

Also, there are measurement results from the Robie et al (1970, 1971). [13][14] The data was summarized in Horai. [8] The average of measurement results C_p [J/kgK] was calculated with log approximation to make it the function of temperature which showed in Eq. (4).

$$C_p = 436.69 \times \ln(T) - 1752.2 \quad (4)$$

With the specific measurement result of the FJS-1 [15] and equation for MLS-1 [16] which is Eq. (5), all results are plotted in Fig. 4.

$$C_p = -1.84585 + 1.04741 \times \log(T) \quad (5)$$

It did not show significant difference between lunar regolith and regolith simulant. It is also known that the difference between measuring the specific heat of the lunar regolith and regolith simulant under vacuum condition or ambient pressure does not produce large deviation. There are also some other empirical equations derived from measurements; however, the result of them does not differ much from those here. [17]

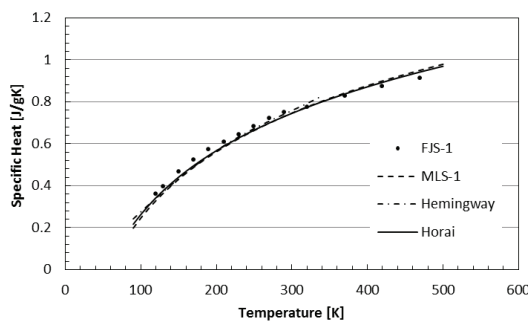


Fig. 4 Specific Heat of Lunar Regolith and Simulants

3.2 Optical Properties

The regolith reflectance depends on the angle of incident energy, local mineralogy, density as well as temperature. [17] It ranged from 0.076-0.297 in Apollo 11, 12 and 14 samples. [18-21] The absorptivity is 0.703-0.924 through solar spectrum.

Spectral infrared emissivity of Apollo 12 sample 12070 density 1910 kg/m³ ranged 0.903-0.965, Apollo 12 sample density 1600 kg/m³ ranged 0.933-0.976 and Apollo 14 sample 14163 density 1600 kg/m³ ranged 0.925-0.976 at 90K-400K respectively. [18-21] Results of the measurements are expressed as a function of temperature.

3.3 Thermal Conductivity

The properties of lunar regolith have been researched over the years. Thermal conductivity of lunar regolith has been measured both in-situ and in laboratories on earth. The in-situ measurement was conducted in Apollo missions. It measured heat flow by inserting probes into the regolith. Thermal conductivity was calculated from the obtained data using densities and heat capacities. Since some equipment was broken during the Apollo 16 mission, the effective data was taken in Apollo 15 and 17 missions. [22] The solid and dotted lines in Fig. 5 show the revised thermal conductivity from long term measurement. [22] It is known that the thermal conductivity of lunar regolith is extremely low because of its porous structure. From the result of in-situ measurement, the thermal conductivity depth dependency can be seen.

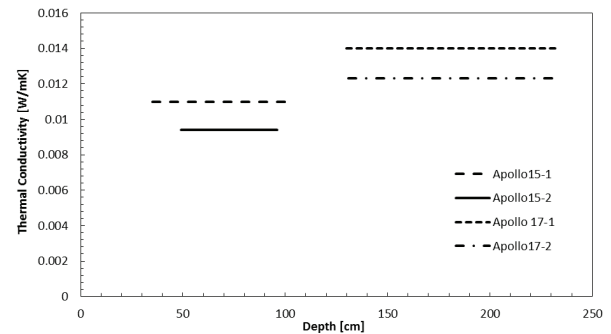


Fig. 5 Thermal Conductivity of Regolith (Depth)

To measure the thermal conductivity in the laboratory conditions many methods have been developed for various types of materials. For powder materials like lunar regolith, the most frequently used method seems to be the hot wire method. It is a transient measurement method which measures the temperature change of the hot wire set inside the specimen to work as a heater and thermometer. The merit of this method is that it does not require a large amount of time or specimen to conduct the measurement. Using the equation shown below, thermal conductivity will appear as a gradient of plotted data graph of logarithm of time t versus temperature T difference using known input q .

$$T_2 - T_1 = \frac{q}{4\pi k} \ln \frac{t_2}{t_1} \quad (6)$$

Thermal conductivity of granular materials k_{eff} is commonly expressed as it is shown in Eq. (7). The

characters k_c , k_g and k_r represent the conductive thermal conductivity through particles, thermal conductivity through filled gas between particles and via radiation respectively.

$$k_{eff} = k_c + k_g + k_r \quad (7)$$

Since there is no atmosphere on the lunar surface, it can exclude the effect of k_g . Therefore, the thermal conductivity under lunar condition will be expressed as:

$$k_{eff} = k_c + k_r \quad (8)$$

Since there were no significant changes in conductive thermal conductivity compared to radiative thermal conductivity, depending on temperature, as an empirical law, the effective thermal conductivity of powder material under vacuum can be expressed as a function of temperature. [23]

$$k_{eff} = A + BT^3 \quad (9)$$

A and B are the constants determined from the measurement result. By using the hot wire technique, which was mentioned above, thermal conductivity measurement of Apollo samples under vacuum condition were conducted by Cremers et. al. [24-27] The results of the measurement was summarized into equations by determining constants A and B which are shown in Table. 3. The graph of it is shown in Fig. 6. Caption of the graph corresponds to the written order in Table. 3. All constant values are in close order and the tendencies are similar.

Table. 3 Thermal Conductivity Constants of Lunar Regolith

Sample	A [W/mK]	B [W/mK ⁴]
Apollo 11 (1300 kg/m ³)	1.42×10^{-3}	1.73×10^{-11}
10084 (1640 kg/m ³)	1.87×10^{-3}	2.3×10^{-11}
Apollo 12 (1300 kg/m ³)	0.922×10^{-3}	3.19×10^{-11}
12001 (1640 kg/m ³)	0.985×10^{-3}	2.06×10^{-11}
14163 (1500 kg/m ³)	0.716×10^{-3}	2.54×10^{-11}
14163 (1800 kg/m ³)	1.43×10^{-3}	2.06×10^{-11}
15031 (1300 kg/m ³)	0.6246×10^{-3}	1.192×10^{-11}
68501 (1500 kg/m ³)	0.484×10^{-3}	1.11×10^{-11}

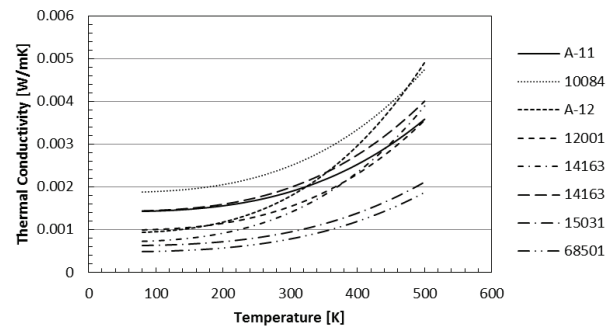


Fig. 6 Thermal Conductivity of Lunar Regolith (Temperature)

As one of the regolith simulants, thermal conductivity of Oregon basalt (grain size 37 to 62 μ m) has been measured with different densities, which are used as one of the regolith simulants. [8] Thermal conductivity measurement of JSC-1A was conducted with a cavity breadboard. [28] It is a steady state measurement conducted up to 900 $^{\circ}$ C. From both measurement results, constants A and B were determined. In the case of FJS-1, the thermal property of regolith simulant is partly revealed by the supplying company. In most often used ranges, the values can be picked up from the data. However, there is some lack of data in certain ranges of temperature. There is actual measurement data of above 20 $^{\circ}$ C existing in catalogue (25-800 $^{\circ}$ C) and Sakatani et. al (20 - 40 $^{\circ}$ C). [29][30] Therefore, the constants for Eq. (9) were estimated in this research to produce the equation for thermal conductivity versus temperature. The least square method was used for fitting. Solid lines in Fig. 7, Fig. 8 and Fig. 9 show the results of the fitting. The measurement values are plotted with black circles. The values of constants are in Table. 4 with all the other regolith simulant thermal conductivity measurements results of Basalts and JSC-1A. In Fig. 7, Fig. 8 and Fig. 9, calculation results of lunar regolith thermal conductivity model using the equation for porous media are also plotted. [31]

$$k_{eff} = k_c + k_r \quad (10)$$

$$k_c = k_s \left[\frac{3(1 - \mu^2) S_F P R}{4E N_A} \right]^{1/3} \frac{1}{0.531S} \left(\frac{N_A}{N_L} \right) \quad (11)$$

$$k_r = 4Fd\sigma T_m^3 \quad (12)$$

k_s is the thermal conductivity of solid, μ is Poisson's ration, P is pressure, F is radiative exchange factor, E is young's modulus, d is particle diameter, R is particle radius, σ is Stefan-Boltzman constant, T_m is mean temperature and S_F , N_A , S , N_L are the structural parameter depending on the packing arrangement. It is seen that these plots do not go along with the data of FJS-1, although it has been well suited with lunar regolith thermal conductivity data which is shown in Fig. 6. The result of the constants of FJS-1 shows that the thermal conductivity of the simulant is at a higher

order than the lunar regolith or basalts or thermal conductivity model. Sakatani measured the stress dependence of thermal conductivity of FJS-1 using the hot wire method. [30] This result is plotted in Fig. 10. This graph also shows the plotted data of the thermal conductivity of the in-situ lunar regolith result of the measurements against the depth converted into against pressure. This was done by calculating the static pressure by its own weight and the result of a same conversion adapted to lunar regolith model, which is drawn in a solid line. These results showed that the pressure dependent thermal conductivity of the regolith simulant FJS-1 is lower than that of lunar regolith or the regolith model and temperature dependent thermal conductivity is higher than that of lunar regolith or the regolith model. In the lunar regolith case, thermal conductivity of depth dependency and temperature dependency are about equal to that of the regolith model. Since the measurements of the thermal conductivity of lunar regolith are conducted with a few grams of samples, it is understandable to see the rise in values of depth depended thermal conductivity caused by pressure even though they have different bulk density values. This is applicable to the regolith model, which fit to both results of temperature and depth dependency. However, as in the case of FJS-1, temperature dependent thermal conductivities are higher than the result of pressure dependence. Even the measurements are conducted with 50ml of samples for temperature dependence and more for pressure dependence. This is not describable, and the measurement results of FJS-1 differs by double and has one order higher than lunar regolith measurement result. Even the components and particle sizes are similar. Moreover, there are no other data existing, which means the measurement data for comparison and correction are required for actual use. Therefore, the thermal conductivity measurement of FJS-1 was conducted using the guarded hot plate method.

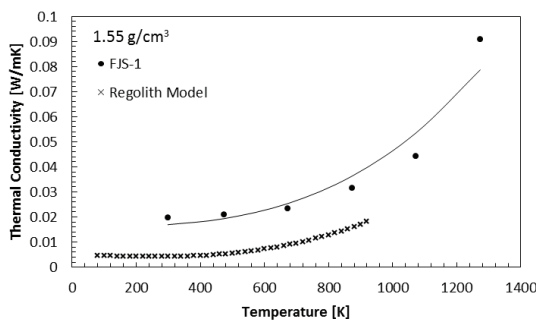


Fig. 7 Thermal conductivity of FJS-1 (1.55 g/cm³)

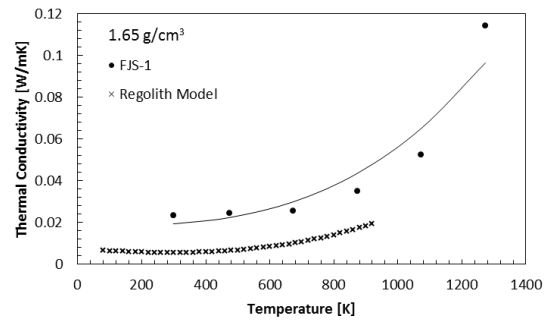


Fig. 8 Thermal conductivity of FJS-1 (1.65 g/cm³)

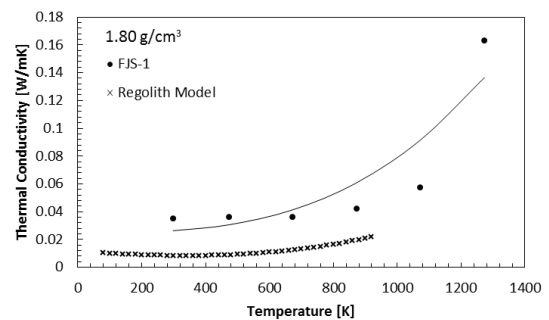


Fig. 9 Thermal conductivity of FJS-1 (1.80 g/cm³)

Table. 4 Constants of Regolith Simulants

Sample	A [W/mK]	B [W/mK ⁴]
Basalt (790 kg/m ³)	0.509×10^{-3}	1.69×10^{-11}
Basalt (1640 kg/m ³)	0.650×10^{-3}	1.67×10^{-11}
Basalt (1300 kg/m ³)	0.595×10^{-3}	1.72×10^{-11}
Basalt (1640 kg/m ³)	0.887×10^{-3}	1.9×10^{-11}
Basalt (1500 kg/m ³)	1.237×10^{-3}	2.34×10^{-11}
Basalt (1800 kg/m ³)	1.642×10^{-3}	3.43×10^{-11}
JSC-1A (1300 kg/m ³)	6.864×10^{-3}	3.52×10^{-11}
FJS-1 (1550 kg/m ³)	16.149×10^{-3}	3.03×10^{-11}
FJS-1 (1650 kg/m ³)	18.3×10^{-3}	3.78×10^{-11}
FJS-1 (1800 kg/m ³)	24.9×10^{-3}	5.41×10^{-11}

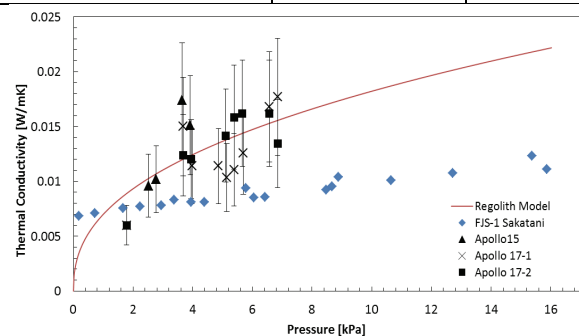


Fig. 10 Pressure Dependent Thermal Conductivity

4. GUARDED HOT PLATE METHOD

4.1 Method

The guarded hot plate method is a steady state thermal conductivity measurement. The setup is based on the ASTM C177-13. [32] This method is often used for evaluating the thermal conductivity of the heat insulator. It has a heated guard ring surrounding the metered section of the heating element to reduce the uncertainty in the thermal conductivity estimate. The gap is filled with either air or insulation in order to enhance lateral thermal resistance of the metered section. Also, the guard is maintained at the same temperature as the metered section by a separate heater. Fig. 11 shows its setup. It measures the temperature, calorific value, heating area and the thickness of the specimen to determine its thermal conductivity k_i [W/mK] from Fourier's Law. q_i [W/m²] is the heat flux applied to sample i , $T_{1,i}$, and $T_{2,i}$ [K] are the temperatures measured by thermocouples in sample i , and L_i [m] is the distance between these thermocouples in sample i .

$$k_i = \frac{q_i L_i}{T_{2,i} - T_{1,i}} \quad (13)$$

Under steady state conditions, heat flux applied to each sample q_i is estimated as Eq. (14). V is the voltage applied to the heater and R [Ω] is the resistance of it. A_m and A_g [m²] are the area of the meter section heater and gap section.

$$q_i = \frac{1}{2} \frac{V^2}{R} \frac{1}{A_m + A_g/2} \quad (14)$$

Voltage and resistance are measured with digital multimeter after reaching the steady state. Thermal conductivity of samples A and B under steady state are averaged over 30 minute intervals to determine the effective thermal conductivity. The number of measurement sets for k_A and k_B is n in the Eq. (15).

$$k_{eff} = \frac{1}{2n} \sum_{j=1}^n k_A(j) + k_B(j) \quad (15)$$

The uncertainty in thermal conductivity depends on the systematic error for each measurement, expressed as:

$$\frac{\Delta k_i}{k_i} = \sqrt{\Delta q_i^2 + \Delta L_i^2 + \Delta A^2 + \Delta T_i^2} \quad (16)$$

where Δx is the systematic error associated with quantity x , q_i refers to supplied heat flux, L_i refers to the vertical distance between sample thermocouples, A refers to the measurements area, and T_i refers to the measured temperature of sample i . Each error is given by:

$$\Delta q_i^2 = \left(\frac{\Delta V}{q}\right)^2 + \frac{1}{4} \left(\frac{\Delta R}{q}\right)^2 + \left(\frac{q_{loss,i}}{q}\right)^2 \quad (17)$$

$$\Delta L_i^2 = \left(\frac{\Delta L_{2,i}}{L_{2,i} - L_{1,i}}\right)^2 + \left(\frac{\Delta L_{1,i}}{L_{2,i} - L_{1,i}}\right)^2 \quad (18)$$

$$\Delta A^2 = \left(\frac{\Delta A_m}{A_m + A_g/2}\right)^2 + \frac{1}{4} \left(\frac{\Delta A_g}{A_m + A_g/2}\right)^2 \quad (19)$$

$$\Delta T_i^2 = \left(\frac{\Delta T_{2,i}}{T_{2,i} - T_{1,i}}\right)^2 + \left(\frac{\Delta T_{1,i}}{T_{2,i} - T_{1,i}}\right)^2 \quad (20)$$

where q_{loss} is the error due to heat losses. The error in voltage and resistance are 0.001V and 0.001 Ω respectively, based on the uncertainty from digital multimeter. Heat losses are calculated from the difference of supplied heat flux q and the heat flux removed by recirculating chiller water:

$$q_{loss,i} = \frac{V^2}{2R} - \dot{m}_i c_p (T_{w2,i} - T_{w1,i}) \quad (21)$$

$$q_{loss} = \frac{1}{2} (q_{loss,A} + q_{loss,B}) \quad (22)$$

where \dot{m} is the mass flow rate of the recirculating chiller to cold plate i , c_p is the specific heat of the chiller water, and $T_{w2,i}$ and $T_{w1,i}$ are the temperatures of the chiller water leaving and entering cold plate i . The uncertainty in the axial distance between the two thermocouples in each sample L_A and L_B are expected to be on the order of ± 0.1 mm. The uncertainty in the area measurements A_m and A_g are expected to be on the order of ± 0.1 mm². The thermocouple uncertainty is expected to be on the order of ± 0.5 °C. The effective thermal conductivity uncertainty is expressed as:

$$\frac{\Delta k_{eff}}{k_{eff}} = \sum_{j=1}^n \frac{1}{2n} \sqrt{\Delta k_A(j)^2 + \Delta k_B(j)^2 + 2cov(k_A, k_B)} \quad (23)$$

$$cov(k_A, k_B) = \frac{(k_A(j) - \bar{k}_A)(k_B(j) - \bar{k}_B)}{n}$$

where \bar{k}_A and \bar{k}_B are respectively the average thermal conductivity for sample A or B over n measurement sets and $cov(k_A, k_B)$ is the covariance of k_A and k_B .

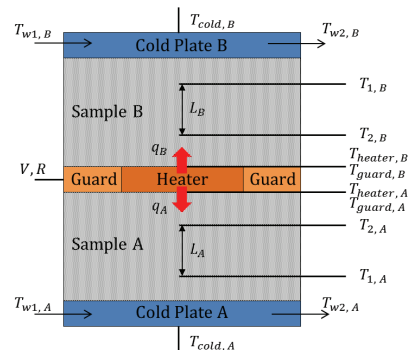


Fig. 11 Guarded Hot Plate Set Up

4.2 Sample Making

The first attempt at making the homogenous sample was to make a pellet. This failed because the FJS-1 was too fragile, even by pressurizing it with device's maximum pressure, which was 320 MPa. Secondly, using slurry to make the sample was tested, however it did not work from the view of obtaining the sample in designated height and amount in short time. Therefore, to define the sample, the density was used by preparing the constant volume container with weight measured FJS-1. FJS-1 was poured into a container using a funnel to make the homogeneous sample. [33]

4.3 Apparatus Setup (Double-sided)

Double-sided measurement set up is shown in Fig. 12. The reasons for this setup are to follow the basic setup for guarded hot plate and to check the possibility of excluding the effect of the upper side and the lower side of the setup. As a container, a 2 inch ID plastic tube was chosen to set plates inside the container to make direct contact to the sample. The height of the container was set to 2.5 cm to make it compatible with keeping thermocouple distance and making the sample as thin as possible. Plastic wrap was used to sustain the sample inside the container. Fishing line was set to hold the thermocouple in position.

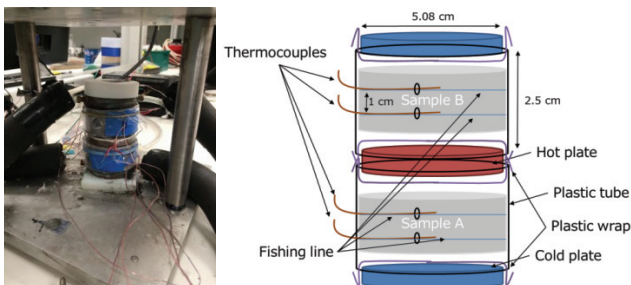


Fig. 12 View of Double-sided measurement

4.4 Measurement Result (Double-sided)

The measurement results of the double-sided setup are shown in Fig. 13, Fig. 14 and Table. 5. It was conducted twice and each set has three times the measurement with the sample density of 1.6 g/cm³. Fig. 13 shows the result of six measurements. The average thermal conductivity of the whole measurement was 0.19 W/mK. This value is similar to the results of JSC-1A thermal conductivity measurement in the atmosphere [34] or the other simulant measurement conducted in the atmosphere. [35][36] Fig. 14 shows the averaged result of each measurement, first time and second time. Deviation between two measurements was about 6%. However, in both measurements, the heat loss through the measurement was considerably high, which led to a high uncertainty of the measurement. Since the result of the first

measurement showed the high heat loss value, the second measurement was conducted with tight surrounding insulation to prevent the loss of heat. However, as it is seen from the result, the value of heat loss did not change. The possible paths of the heat loss are through the plastic tube (0.2 W/mK), plastic wrap (0.3 W/mK), thermocouple (211 W/mK) and fishing line (0.3 W/mK). The most considerable paths are caused by the plastic wrap between the plates and sample and the heat flowing through the plastic tube which prevents it from reaching the cold plate. These are the points which need improvement. Moreover, Table. 5 showed that the thermal conductivity of Sample A is higher than Sample B in all measurements. This is considered the effect of the setting sample in the lower or upper side of the hot plate. The weight of the cold plate, hot plate and other sample loaded on to the lower sample, which might have caused slight compaction of the designated density. The thermal conductivity of the sample with 1.8 g/cm³ was also measured to see the effect in reducing the deviation between Sample A and B. The sample with higher density than 1.8 g/cm³ was difficult to make by pouring and vibrating. Despite making the sample with higher density, the effect of setting remained. Therefore, this is also a point that requires improvement in the next setup.

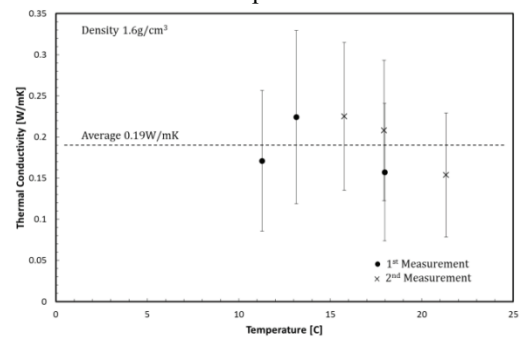


Fig. 13 Measurement Result

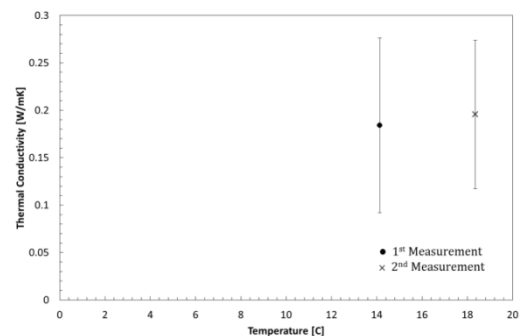


Fig. 14 The Averaged Measurement Result

Table. 5 Measurement Result

	T _{avg} [°C]	ΔT [°C]	k _A [W/mK]	k _B [W/mK]	k _{eff} [W/mK]	dq _{loss}	$\frac{\Delta k_{eff}}{k_{eff}}$
1 st	15.8	11.4	0.238	0.212	0.225	56%	40%
	17.9	13.2	0.219	0.197	0.208	58%	41%
	21.3	15.7	0.160	0.148	0.154	70%	50%
2 nd	13.1	8.51	0.254	0.195	0.224	66%	47%
	11.3	10.5	0.181	0.161	0.171	72%	51%
	18.0	12.5	0.167	0.148	0.157	75%	53%

4.5 Apparatus Setup (Single-sided)

The first measurement conducted with double-sided measurement with polycarbonate as the container ended with a large heat loss and higher thermal conductivity than estimated. Considering the points requires improvement from the former measurement result; the setup for the next measurement was planned. It was planned to conduct a single-sided measurement. The set up schematic is shown in Fig. 15. The merit of this measurement is that it does not require two identical samples. Also the width of the container was widened to prevent heat leakage through the container. Polystyrene was chosen for the material of the container, which has lower thermal conductivity (0.04W/mK) compared to the plastic tube. The FJS-1 is filled between the hot plate and cold plate of the non-active side. The largest improvement of this setup is the ability to enable direct contact between sample and plates. It will presumably help in reducing the heat loss of the measurement and increase the accuracy of the results. Three thermocouples were set into sample to check the effect of the weight and the averaged thermal conductivity from these thermocouples is used as the effective thermal conductivity to exclude the uncertainty of the sample homogeneousness. After the decrease of uncertainties of the measurement results due to the heat loss was confirmed, the whole setup is set inside the vacuum chamber to obtain the data under vacuum condition.

Although the container for setup has been made and was ready for measurement, unfortunately, the conduction of the measurements was not allowed due to various reasons.

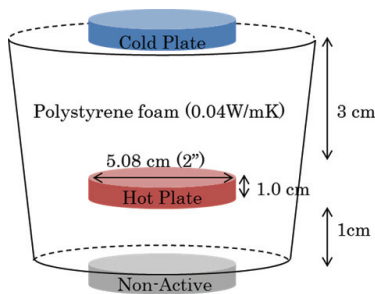


Fig. 15 Schematic View of Single-Sided Setup (i)

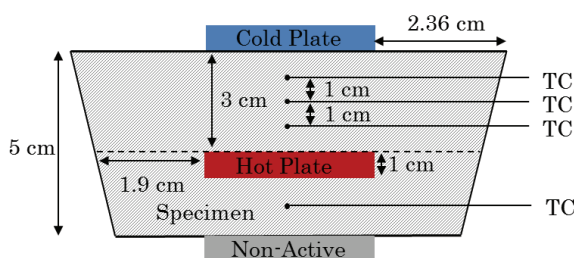


Fig. 16 Schematic View of Single-Sided Setup (ii)

5. DISCUSSION AND CONCLUSION

The thermal conductivity value obtained from the measurement was within the estimated range. The reason for the difference in thermal conductivity under vacuum and in the atmosphere is considered as the effect of conduction. Horai, who measured thermal diffusivity of regolith simulant under the atmosphere and vacuum, concluded that it cannot be explained with only the effect of k_g alone. [36] Also it cannot be described by k_r too. Under this circumstance, it is natural to think the change is caused by the variation of k_c . Conduction is in two parts: one is conduction through the mineral grains and the other is across the contact surface between the mineral grains. This contact across the interface of mineral grains is strongly influenced by gaseous pressure, and the absorption of gas by solid minerals would be better improved upon at a lower temperature. The measurement with single-sided setup could not be accomplished during this program; however, the problem from the conducted measurement led to a better setup.

ACKNOWLEDGEMENTS

I would like to thank Prof. Pilon for all the advice and support he gave me through the program.

REFERENCES

- [1] <http://news.mynavi.jp/series/southkorea/003/>
- [2] Google Lunar Xprize : <http://lunar.xprize.org/>
- [3] Presley, Marsha A., and Philip R. Christensen. "Thermal conductivity measurements of particulate materials: 4. Effect of bulk density for granular particles." *Journal of Geophysical Research: Planets* (19912012) 115.E7 (2010).
- [4] Presley, M. A. and Christensen, P. R., "Thermal Conductivity Measurements of Particulate Materials - 1. A Review," *Journal of Geophysical Research*, Vol. 102, 1997, pp. 65356549.
- [5] Sibille, Laurent, et al. "Lunar regolith simulant materials: recommendations for standardization, production, and usage." National Aeronautics and Space Administration: Marshall Space Flight Center (2005).
- [6] Bonanno, A., and L. E. Bernold. "Exploratory Review of Sintered Lunar Soil Based on the Results of the Thermal Analysis of a Lunar Soil Simulant." *Journal of Aerospace Engineering* (2014): 04014114.
- [7] Rickman, D. L., C. A. McLemore, and J. C. Fikes. "Lunar Regolith Simulant User's Guide". National Aeronautics and Space Administration, Marshall Space Flight Center, 2010.
- [8] Horai, Ki-Iti, and Naoyuki Fujii. "Thermophysical properties of lunar material returned by Apollo Missions." *The moon* 4.3-4 (1972): 447475.
- [9] Houston, W. N., J. K. Mitchell, and W. D. Carrier III. "Lunar soil density and porosity." *Lunar and Planetary Science Conference Proceedings*. Vol. 5. 1974.

- [10] Carrier III, W. David, James K. Mitchell, and Arshud Mahmood. "The relative density of lunar soil." Lunar and Planetary Science Conference Proceedings. Vol. 4. 1973.
- [11] Heiken, Grant, David Vaniman, and Bevan M. French. Lunar sourcebook: A user's guide to the Moon. CUP Archive, 1991.
- [12] Hemingway, B. S., R. A. Robie, and W. H. Wilson. "Specific heats of lunar soils, basalt, and breccias from the Apollo 14, 15, and 16 landing sites, between 90 and 350 K." Lunar and Planetary Science Conference Proceedings. Vol. 4. 1973.
- [13] Robie, R. A., B. S. Hemingway, and W. H. Wilson. "Specific heats of lunar surface materials from 90 to 350 K." Lunar and Planetary Science Conference Proceedings. Vol. 1. 1970.
- [14] Robie, R. A., and B. S. Hemingway. "Specific heats of the Lunar Breccia (10021) and Olivine Dolerite (12018) between 90° and 350° Kelvin." Lunar and Planetary Science Conference Proceedings. Vol. 2. 1971.
- [15] Shimizu Corporation FJS-1 Catalog Data
- [16] Richter, Scott W. Experimental determination of in situ utilization of lunar regolith for thermal energy storage. No. 929277. SAE Technical Paper, 1992.
- [17] Hager, P. B., D. M. Klaus, and U. Walter. "Characterizing transient thermal interactions between lunar regolith and surface spacecraft." Planetary and Space Science 92 (2014): 101-116.
- [18] Birkebak, Richard C., and Ariono Abdulkadir. "Total emittance of lunar fines." Journal of Geophysical Research 77.7 (1972): 1340-1341.
- [19] Birkebak, Richard C. "Apollo 12 thermal radiation properties." *The moon* 4.1-2 (1972): 128-133.
- [20] Birkebak, Richard C. "Spectral reflectance and emittance of Apollo 11 and 12 lunar material." AIAA Journal 10.8 (1972): 1064-1067.
- [21] Birkebak, Richard C., and James P. Dawson. "Thermal radiation properties of Apollo 14 fines." *The moon* 6.1-2 (1973): 93-99.
- [22] Langseth, Marcus G., Stephen J. Keihm, and Kenneth Peters. "Revised lunar heat-flow values." Lunar and Planetary Science Conference Proceedings. Vol. 7. 1976.
- [23] Watson, Kenneth. "I. The thermal conductivity measurements of selected silicate powders in vacuum from 150 350 K, II. An interpretation of the Moon's eclipse and lunation cooling as observed through the Earth's Atmosphere from 814 microns." California Institute of Technology (1964).
- [24] Cremers, C. J., and R. C. Birkebak. "Thermal conductivity of fines from Apollo 12." Lunar and Planetary Science Conference Proceedings. Vol. 2. 1971.
- [25] Cremers, C. J., and H. S. Hsia. "Thermal conductivity and diffusivity of Apollo 15 fines at low density." Lunar and Planetary Science Conference Proceedings. Vol. 4. 1973.
- [26] Cremers, C. J., and H. S. Hsia. "Thermal conductivity of Apollo 16 lunar fines." Lunar and Planetary Science Conference Proceedings. Vol. 5. 1974.
- [27] Cremers, C. J. "Thermophysical properties of Apollo 14 fines." Journal of Geophysical Research 80.32 (1975): 4466-4470.
- [28] Parzinger, S., et al. "Experimental Determination of the Thermal Conductivity of JSC-1A under Vacuum Conditions with a Cavity Receiver Breadboard Design for Regolith Heating." 42nd International Conference on Environmental Systems. 2012.
- [29] Sakatani, Naoya, et al. "Experimental study for thermal conductivity structure of lunar surface regolith: Effect of compressional stress." *Icarus* 221.2 (2012): 1180-1182.
- [30] Sakatani, N., et al. "Thermal conductivity measurements of glass beads and regolith simulant under vacuum conditions." European Planetary Science Congress 2013, held 8-13 September in London, UK.
- [31] Notsu, Ryota, Hosei Nagano, and Hiroyuki Ogawa. "A proposal of lunar long-duration method by using high heat storage capability of regolith." Proceedings of the 43rd International Conference on Environmental Systems. 2013.
- [32] ASTM Standard, "C177-13", Standard test method for steady-state heat flux measurements and thermal transmission properties by means of the guarded-hot plate apparatus. ASTM International, West Conshohocken, PA, USA, 2014
- [33] Gouache, Thibault P., et al. "Regolith simulant preparation methods for hardware testing." Planetary and Space Science 58.14 (2010): 1977-1984.
- [34] Yuan, Zeng-Guang, and Julie E. Kleinhenz. "Measurement of apparent thermal conductivity of JSC-1A under ambient pressure." 49th AIAA Aerospace Sciences Meeting. 2011
- [35] Bennett, E. C., Wood, H. L., Jaffe, L. D., and Martens, H. E., "Thermal properties of a simulated lunar material in air and vacuum," AIAA Journal, Vol. 1, No. 6, 1963, pp 1402-1407.
- [36] Horai, K., Simmons, G., Kanamori, H., and Wones, D., "Thermal diffusivity, conductivity and thermal inertia of Apollo 11 lunar material," Proceedings of the APOLLO 11 Lunar Science Conference, Vol. 3, Houston, Texas, January 5-8, 1970, pp. 2243-2249

Growth and Characterization of Single-Crystalline Zr (0002)/Al₂O₃ (0001) and ZrC (111)/Al₂O₃ (0001) Thin Films

Masaki Sato

Graduate School of Engineering, Nagoya University
Satou.masaki@j.mbox.nagoya-u.ac.jp

Supervisor: Suneel Kodambaka

Department of Material Science and Engineering,
Henry Samueli School of Engineering and Applied Sciences, University of California Los Angeles
kodambaka@ucla.edu

ABSTRACT

We investigated the effect of substrate temperature T_s on ultra-high vacuum dc magnetron sputter-deposition growth of Zr and ZrC thin films on Al₂O₃(0001) substrates. All the Zr and ZrC thin films were grown from a 99.9% pure Zr target in 99.999% purity argon and argon-ethylene gas mixtures maintained at 10 mTorr pressure with target-to-substrate separation of 28 cm. The as-grown film surface and bulk structure and composition were determined using a combination of low energy electron diffraction, Auger electron spectroscopy, x-ray diffraction, x-ray photoelectron spectroscopy. From high-resolution x-ray diffraction data, we found that all ZrC thin films are single-crystalline with (111) orientations at T_s between 1200°C and 1400°C. The best crystallinity, as determined by the full-width half maxima of the diffraction peaks, of the Zr and ZrC layers are obtained at films $T_s = 750$ °C and 1300 °C, respectively.

Undisclosed

Electrical Transport Properties of Undoped BaSi₂ Evaporated Thin Films

Takamichi Suhara

Department of Materials, Physics and Energy Engineering, Graduate School of Engineering, Nagoya University
suhara.takamichi@d.mbox.nagoya-u.ac.jp

Supervisor: Prof. Kang L. Wang

Department of Electrical Engineering, Henry Samueli School of Engineering and Applied Science, University of California, Los Angeles
wang@ee.ucla.edu

ABSTRACT

Semiconducting BaSi₂ is a novel material expected for solar cells application because of large absorption coefficient and suitable band gap for single-junction solar cells. In addition, it is attractive that all the constituent elements are earth-abundant. BaSi₂ films grown by molecular beam epitaxy have been used to investigate its various properties. Development of low cost method to grow BaSi₂ films is required for large-scale manufacturing. We study the electrical properties of BaSi₂ films grown by conventional vacuum evaporation method. We have succeeded in improvement of the quality of BaSi₂ film by post-anneal. The carrier density of BaSi₂ film drastically reduces after high temperature anneal and temperature dependency of carrier density turns into semiconducting behavior from metallic one. We speculate that post-anneal improves the crystal quality by decreasing both the density of grain boundaries and other phase in films such as unreacted Ba residues and other silicide compound than BaSi₂.

1. INTRODUCTION

Inorganic semiconductor materials such as Cu(In_xGa_{1-x})Se₂ (CIGS) and CdTe have increased the solar cells market share instead of most conventional crystalline silicon (c-Si) solar cells because of their possibilities for cost and resource savings. However, it is concerned that CIGS and GaAs contain rare metals and/or toxic materials. Recently, orthorhombic barium disilicide (BaSi₂) semiconductor has been attracted because of a numerous number of barium and silicon in the earth crust. The BaSi₂ films have been successfully grown by using molecular beam epitaxy (MBE) method on Si (111)^[1-3], and Si (001)^[4]. Various properties such as optical^[5-7] and electrical^[5] properties of epitaxial BaSi₂ films have been evaluated. According to previous reports, BaSi₂ epitaxial film has a bandgap (E_g) of 1.3 eV^[5], which is suitable for single-junction solar cells, and a large optical absorption coefficient (α) of $3 \times 10^4 \text{ cm}^{-1}$ for a photon energy of 1.5 eV^[5].

The MBE technique can grow a-axis-oriented BaSi₂ epitaxial films which have high crystal quality,^[3] however, this method requires high vacuum level as well as ultra high vacuum (UHV) 10^{-7} Pa. It is not suitable for mass-product with large scale. Alternatively, we proposed the vacuum evaporation method to grow BaSi₂ film. The vacuum evaporation requires vacuum level of 10^{-3} Pa, which is much lower than that of MBE growth. In addition, granule of BaSi₂ source, which is stable in the air, can be used. It should be noted that Ba is reactive in air. Moreover, the film-growth rate of the vacuum evaporation is much faster than that of MBE^[8]. These imply that the vacuum evaporation method would be a very easy and fast way to grow BaSi₂ films.

Using the vacuum evaporation method, so far BaSi₂ films have been grown on silicon^[9], glass^[10], CaF₂^[11] substrates and etc.. It is considered that the crystal quality of the evaporated films are inferior to the epitaxial films because of its fast growth-rate. In addition, it is reported that undoped BaSi₂ film grown by MBE is n-type. In this study, we studied electrical properties of undoped BaSi₂ evaporated films and compared with that of the epitaxial films. Post-anneal effects of BaSi₂ evaporated films will be also discussed.

2. EXPERIMENTAL METHOD

High resistive Si (111) substrates ($\rho > 1000 \text{ } \Omega\text{cm}$) were cleaned with 1% HF solution to etch native SiO₂ layer on the surface. 0.1 g of crushed BaSi₂ source (99% in impurity, Kojundo Chemical Lab.) were heated at over melting point^[12] by current-carrying through tungsten source boat in chamber vacuumed under 10^{-3} Pa. The substrates were heated at 550 °C during whole evaporation process. 100 nm-thick BaSi₂ films were deposited. Samples were taken from chamber after cooling to 40 °C (sample A). The XRD patterns of BaSi₂ evaporated films on silicon substrates are shown in **Fig. 1**^[9]. BaSi₂ films tend to grow orienting (100) on Si (111) because of their small lattice mismatch by MBE.^[3] In the case of the films grown by vacuum evaporation, however, the XRD pattern contains some orientation such as (301) and (211). It is considered that this would be due to high film-growth rate of the vacuum evaporation. In addition, substrate

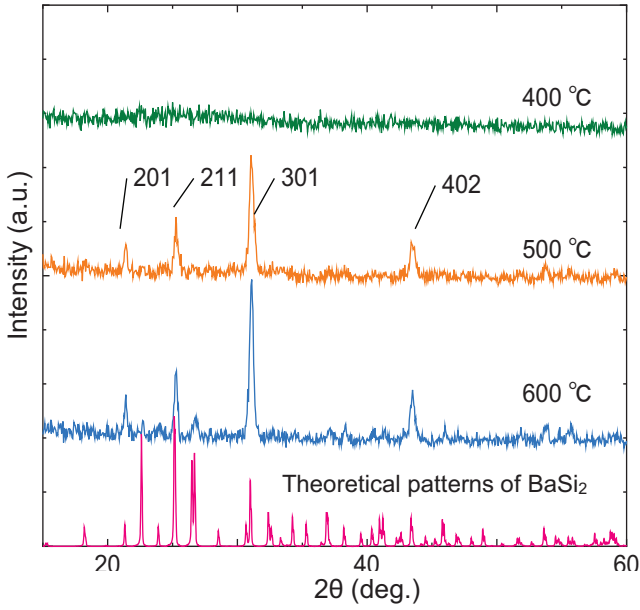


Fig. 1. XRD spectra of evaporated BaSi₂ films and theoretical patterns of powder BaSi₂.^[10]

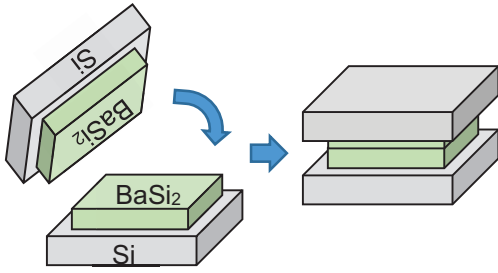


Fig. 2. Schematic draw of post-anneal at 1000 °C.

heating at 500 °C or more is necessary in order to obtain the BaSi₂ stoichiometry films by the vacuum evaporation.

Some samples were subjected to post-anneal in N₂ flow at 500, 1000 °C (sample B, C, respectively) for 5 minutes. It should be noted that Ba atoms are more easily to evaporate from films than Si atoms at high temperature ~1000 °C. In order to prevent the evaporation of Ba atoms from films during post-anneal, another BaSi₂/Si sample were placed upside down on top of the sample as shown in **Fig. 2**.

For transport study, Hall-Bar structures ($w=1$ mm, $L=2$ mm, $t=100$ nm) were fabricated by dry-etching as shown in **Fig. 3**. The labels on Hall-Bar indicate each contacts. Contacts were made by Indium paste and significant *Schottky* barrier were not observed as shown in **Fig. 4**. Hall measurement was carried out in Physical Property Measurement System (PPMS, Quantum Design, Inc) in the temperature range of 170 – 300 K. AC current of 1 μA was applied and longitudinal (V_{xx}) and Hall voltage (V_{xy}) were detected through lock-in amplifier. Out-of-plane external field was swept between -5000 Oe to 5000 Oe.

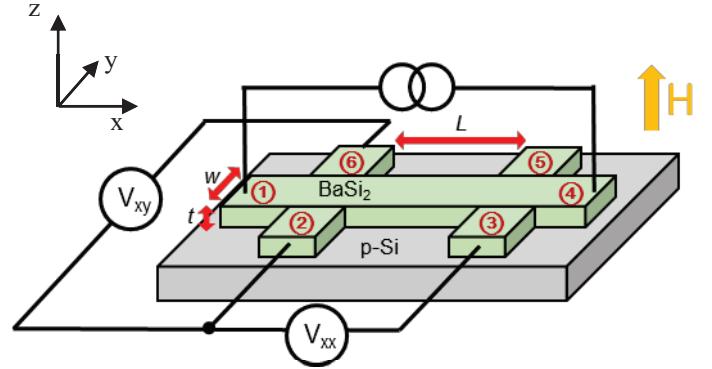


Fig. 3. Schematic draw of Hall-Bar.

Resistivity of films, ρ , is calculated using R_{xx} determined by this measurement.

$$\rho = \frac{tw}{L} R_{xx} \quad (1)$$

Conductivity of films, σ , is inverse number of ρ as shown in following equation.

$$\sigma = \frac{1}{\rho} \quad (2)$$

Hall coefficient R_H is given by

$$R_H = \frac{E_y}{BJ} = \frac{V_y w}{BI} = \frac{R_{xy} w}{B} \quad (3)$$

Here, E_y is the induced electric field when magnetron field, B , is applied. I is current flowed through films, 1 μA in this study. By deformation of equation (3),

$$R_{xy} = \frac{R_H}{w} B \quad (4)$$

electron density, n , is calculated by following equation.

$$n = \frac{1}{eR_H} \quad (5)$$

Here, e is elementary charge (1.602×10^{-19} C). Electron mobility, μ_e , is calculated by

$$\mu_e = \frac{\sigma}{ne} \quad (6)$$

3. RESULTS AND DISCUSSION

3.1. Temperature dependence of conductivity

Temperature dependence of σ was shown in **Fig. 5**. Sample A showed the less temperature dependence, which is like metallic behavior. On the other hand, after post-anneal at 1000 °C, the sample showed significant temperature dependence, in which the conductivity decreases as decrease of measurement temperature. This suggests that post-annealed sample has semiconductor behavior.

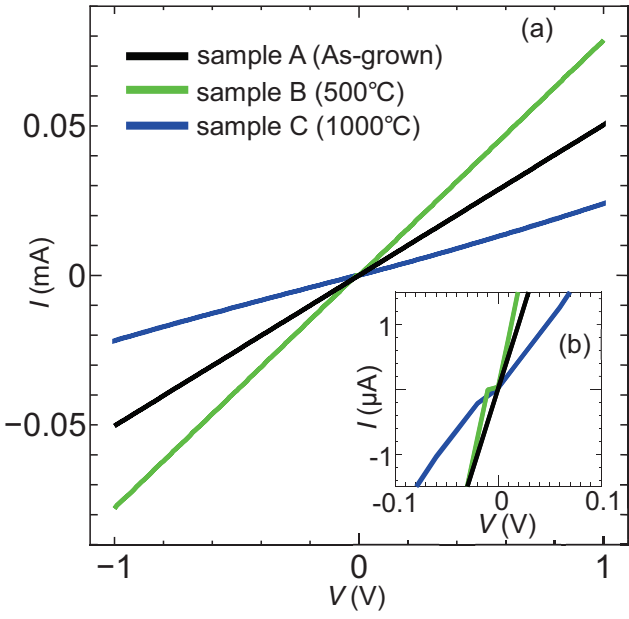


Fig. 4. (a) Contact check of each samples (b) enlarged region of small current

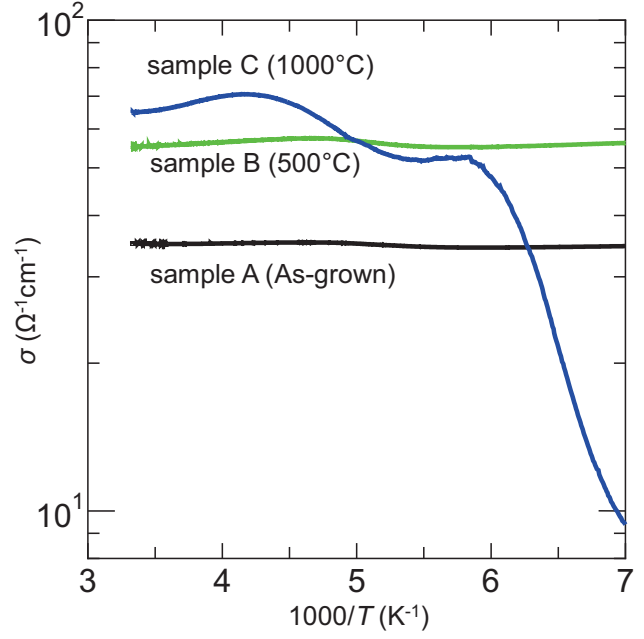


Fig. 5. Temperature dependence of conductivity.

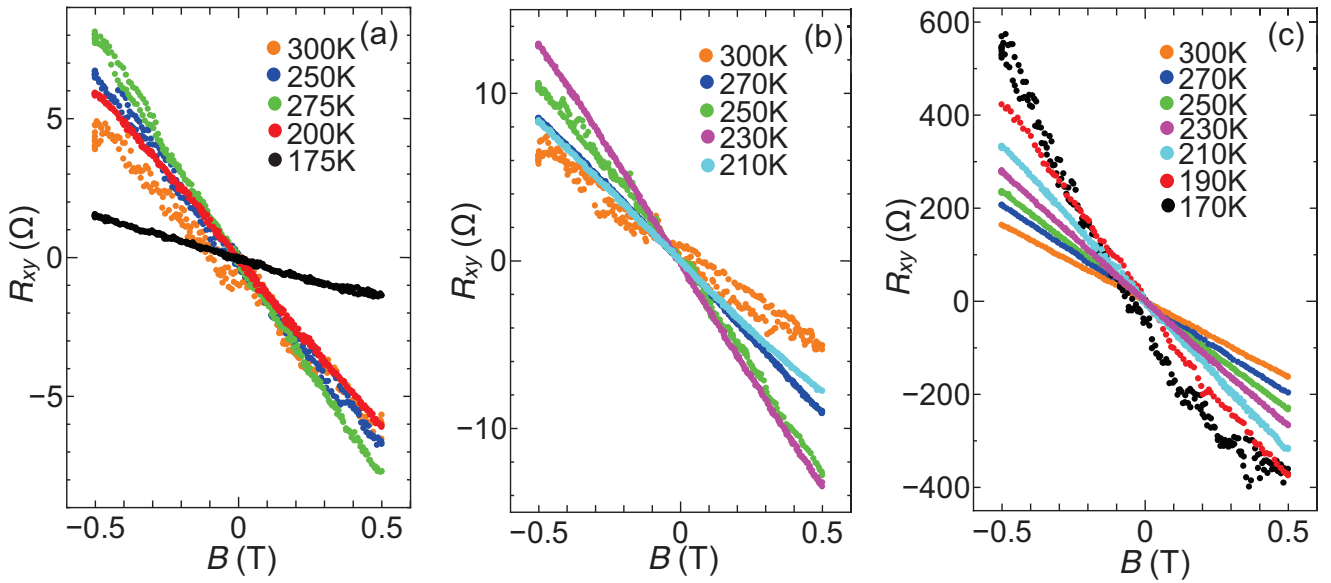


Fig. 6. Hall resistance's temperature dependence (a) sample A, (b) sample B, (c) sample C.

Magnetic field dependence of Hall resistance, R_{xy} , of samples are shown in **Fig. 6**. As remarked in former section, w is 1 mm by Hall-Bar size. Because R_H/w is corresponding to the slope of lines in **Fig. 6**, R_H can be calculated. Since all R_H are negative, therefore, it is turned out that the majority carrier is electrons. That implies undoped BaSi_2 evaporated films are n-type semiconductor as well as epitaxial films.

The electron density of each samples measured at 300 – 170 K are shown in **Fig. 7 (a)**. The electron density of the sample A is $5.6 \times 10^{18} \text{ cm}^{-3}$ at 300K. However, in comparison with sample C, the value is $1.9 \times 10^{17} \text{ cm}^{-3}$, which is lower than the sample A by more than one order of magnitude.

Furthermore, electron density decreases as decreasing temperature in the case of sample C. On the other hand, electron density slightly increases once it decrease in the case of sample A and B. **Figure 7(b)** shows *Arrhenius* plot of electron density of sample C. We attempted to obtain information of donor level, E_d , using this plot. n is drawn as following equation.

$$n = n_0 \exp\left(-\frac{\Delta E}{2kT}\right) \quad (7)$$

Here, n_0 is constant, k is Boltzmann's constant ($8.617 \times 10^{-5} \text{ eV K}^{-1}$). By deformation of equation (7), following equation is given.

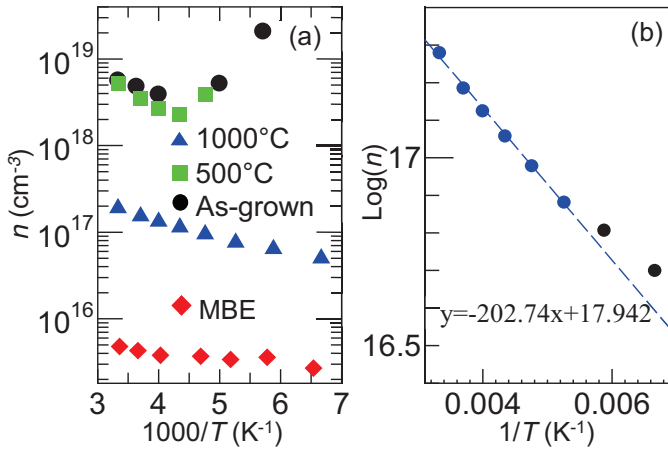


Fig. 7. (a) Electron density of each samples and (b) Arrhenius plot of sample C.

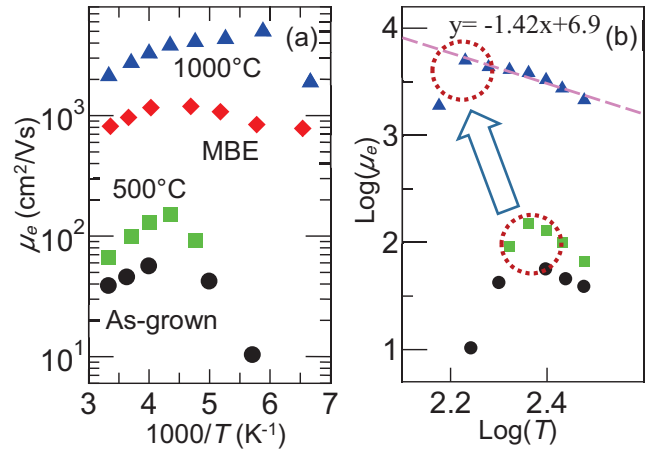


Fig. 9. Electron mobility of each samples (a) ($1000/T$) vs μ_e , (b) $\log(T)$ vs $\log(\mu_e)$

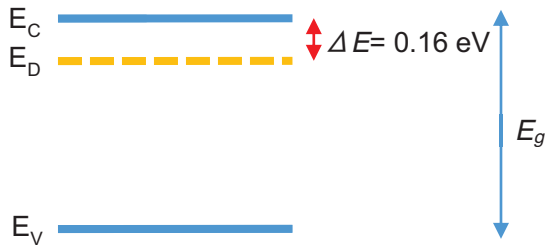


Fig. 8. The band structure of post-annealed BaSi₂ evaporated films

$$\log_{10} n = \log_{10} n_0 - \frac{1}{T} \times \frac{\Delta E}{2k} \log_{10} e \quad (8)$$

The slope of linier approximation of Arrhenius plot is equivalent to $(\Delta E/2k)\log_{10}e$. We obtained $\Delta E = -0.16$ eV as shown in **Fig. 8**. This value is similar to MBE films, whose donor level is -0.13 eV^[5] at the same temperature range.

Figure 9(a) shows the electron mobility of each samples. In comparison with sample A and C, the mobility of sample C is one order magnitude higher. The mobility of epitaxial films is also plotted in **Fig. 9(a)**. The mobility of sample C exceed epitaxial films. This suggests that conductivity of sample C is high. Remarkably the mobility of evaporated films approaches to that of MBE films. Typically temperature dependence of carrier mobility is dominated by two kinds of scattering mechanism. One is ionized impurity scattering, the other is phonon scattering.

$$\mu_i \propto m^{*- \frac{1}{2}} T^{\frac{3}{2}} \quad (9)$$

$$\mu_l \propto m^{*- \frac{5}{2}} T^{- \frac{3}{2}} \quad (10)$$

Here, μ_i is the mobility dominated by ionized impurity scattering, μ_l is the mobility dominated by phonon scattering. In high temperature region, μ_l is dominant, whereas μ_i is dominant in low temperature region. In addition, m^* is

effective mass of atoms. According to *Matthiessen's rule*, there is a relation below between μ_i and μ_l .

$$\frac{1}{\mu_e} = \frac{1}{\mu_i} + \frac{1}{\mu_l} \quad (11)$$

In order to obtain information of electron's scattering mechanism in BaSi₂ evaporated films using these relations, we replotted electron mobility as shown in **Fig. 9(b)**. As for sample C, linear approximation of a range where μ_l is dominant is shown in the graph. The slope of the linear approximation is similar to $-3/2$, so that equation (10) is able to be confirmed.

3.2. Possible mechanism of post-annealing effect

There are three possible reasons of post-anneal effects. One is that there is a lot of grain boundaries in non-post-annealed evaporated BaSi₂ films. During post-anneal, crystal reconstruction would occur and eventually the number of grain boundaries would decrease. Secondary, metallic Ba would remain in evaporated films. These remained Ba would contribute to non-semiconductor behavior. Chemical reaction in films and evaporation from the films by post-anneal at high temperature would reduce the density of metallic Ba residue. The last one is other silicide phase than BaSi₂ remained in the films. Post-anneal at high temperature contributed to reforming of the film, and good quality of BaSi₂ films can be obtained. For these reasons, it is considered that post-anneal at high temperature contributed to improvement of crystal quality of BaSi₂ evaporated films. In **Fig. 7(a)** also shows electron density data of BaSi₂ epitaxial films. Thanks to post-anneal, n become low values, however, epitaxial films have further lower electron density. Therefore, there is possibility that the length of post-anneal could affect to changing of crystal quality.

4. CONCLUSIONS

In this study, we studied electrical properties of undoped BaSi₂ evaporated films by Hall measurement. It revealed that

undoped BaSi₂ films are n-type and electron density is $6 \times 10^{18} \text{ cm}^{-3}$, which is much higher than that of epitaxial film $\sim 5 \times 10^{15} \text{ cm}^{-3}$. The possible reason of high carrier density of as-grown sample would be due to a lot of grain boundaries and metallic Ba residue. Thanks to post-anneal at 1000 °C, electron density decreases to 10^{17} cm^{-3} , which is one order magnitude lower and electron mobility increases two orders of magnitude after post-anneal at 1000 °C. Hence, our conventional and easy vacuum evaporation method with optimum post-anneal would provide the large-scale and high quality BaSi₂ thin films.

ACKNOWLEDGMENTS

Electron density and mobility data of epitaxial films were presented by Prof. T. Suemasu of University of Tsukuba.

This work was financially supported by the Core Research for Evolutionary Science and Technology of the Japan Science and Technology Agency (CREST, JST). Moreover, this work was realized by the Japan-US Advanced Collaborative Education Program (JUACEP), research internship program between Nagoya University and University of California, Los Angeles (UCLA).

I wish to thank Dr. K. Murata and Mr. A. Navabi of Device Research Laboratory (DRL) of UCLA for their affluent experimental helps and advices. I am also grateful to Mr. Y. Nakagawa of Nagoya University and X. Che of DRL for making BaSi₂/Si structures and Hall-bars, respectively. Very great supports by Prof. K. L. Wang of DRL and Prof. N. Usami of Nagoya University are particularly acknowledged.

REFERENCES

- [1] R. A. McKee, F. J. Walker, J. R. Conner, and R. Raj, *Appl. Phys. Lett.* **63**, 2818 (1993).
- [2] Y. Inomata, T. Nakamura, T. Suemasu, and F. Hasegawa, *Jpn. J. Appl. Phys.* **43**, 4155 (2004).
- [3] Y. Inomata, T. Nakamura, T. Suemasu, and F. Hasegawa, *Jpn. J. Appl. Phys.* **43**, L478 (2004).
- [4] K. Toh, K. O. Hara, N. Usami, N. Saito, N. Yoshizawa, K. Toko, and T. Suemasu, *J. Cryst. Growth* **345**, 16 (2012).
- [5] K. Toh, T. Saito, and T. Suemasu, *Jpn. J. Appl. Phys.* **50**, 068001 (2011).
- [6] K. Morita, Y. Inomata, and T. Suemasu, *Thin Solid Films* **508**, 363 (2006).
- [7] N. A. A. Latiff, T. Yoneyama, T. Shibutami, K. Matsumaru, K. Toko, and T. Suemasu, *Phys. Status Solidi C* **10**, 1759 (2013).
- [8] M. Baba, K. Nakamura, W. Du, M.A. Khan, S. Koike, K. Toko, N. Usami, N. Saito, N. Yoshizawa, and T. Suemasu, *Jpn. J. Appl. Phys.* **51**, 098003 (2012).
- [9] Y. Nakagawa, K. O. Hara, T. Suemasu, and N. Usami *Jpn. J. Appl. Phys.* **54**, 08KC03 (2015).
- [10] K. O. Hara, Y. Nakagawa, T. Suemasu, and N. Usami *Jpn. J. Appl. Phys.* **54**, 07JE02 (2015).
- [11] K. O. Hara, J. Yamanaka, K. Arimoto, K. Nakagawa, T. Suemasu, and N. Usami, *Thin Solid Films*. **595**, 68 (2015).
- [12] M. Pani and A. Palenzona, *J. Alloys Compd.* **454**, L1 (2008).

DYNAMICS OF A ROTATING SHAFT IN MAGNETIC BEARINGS

Junya Kato

(Affiliation) Department of mechanical and science engineering, Graduate School of Engineering, Nagoya University
j_kato@nuem.nagoya-u.ac.jp

Supervisor: Professor Tsu-Chin Tsao

(Affiliation) Mechanical and Aerospace Engineering Department, University of California Los Angeles
ttsao@seas.ucla.edu

ABSTRACT

In order to realize stable high-speed and high quality machining operation, the the accuracy of the spindle model in terms of physical and dynamic properties is essential to substantiate confidence in its predictive aptitude for subsequent analyses. This report addresses deriving natural frequency analytically for most simplified shaft model, and then the natural frequency is compared with the experimentally data.

1. INTRODUCTION

High-Speed Machining (HSM) spindles equipped with Active Magnetic Bearings (AMBs) are envisioned to be capable of autonomous self-identification and performance self-optimization for stable high-speed and high quality machining operation. High-speed machining requires carefully selected parameters for reliable and optimal machining performance. For this reason, the accuracy of the spindle model in terms of physical and dynamic properties is essential to substantiate confidence in its predictive aptitude for subsequent analyses.

The natural frequency is one of the most important properties of system, and for rotational shaft system it changes with changing rotational speed of shaft. This report addresses deriving natural frequency analytically for most simplified shaft model.

2. PREVIOUS RESERCH

Figure 1 illustrates the shaft shape and system structure of real magnetic bearing system. And Table 1 shows the natural frequency obtained experimentally. In the following section, It will be compared with the natural frequency derived analytically.

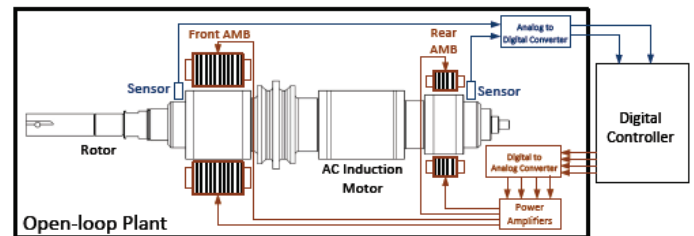


Fig. 1 Diagram of system structure in a single plane

Table 1 Natural frequency of system obtained experimentally

	Frequency [rad/s]
1 st Resonance	6.717×10^3
2 nd Resonance	1.228×10^4
3 rd Resonance	2.017×10^4

3. BASIC THEORY AND CALCULATION

3.1 EQUATION OF VIBRATION BEAM

The shaft model is simplified to a beam which is prismatic (i.e., the cross sections are all equal), homogeneous (i.e., with constant material characteristics).

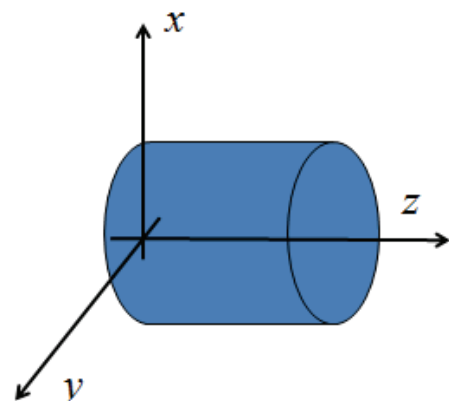


Fig. 2 Reference frame of a beam

(2)

Setting the z -axis of the reference frame along the axis of the beam (Figure 2), the six generalized coordinates of each cross section are the axial displacement u_z , the lateral displacements u_x and u_y , the torsional rotation ϕ_z about the z -axis, and the flexural rotations ϕ_x and ϕ_y about axes x and y . Displacements and rotations are assumed to be small, so that rotations can be regarded as vector quantities, which simplifies all rotation matrices by linearizing trigonometric functions. The three rotations will then be considered as components of a vector in the same way as the three displacements are components of vector u . The generalized forces acting on each cross section and corresponding to the six degrees of freedom defined earlier are the axial force F_z , shear forces F_x and F_y , the torsional moment M_z about the z -axis, and bending moments M_x and M_y about x - and y -axes.

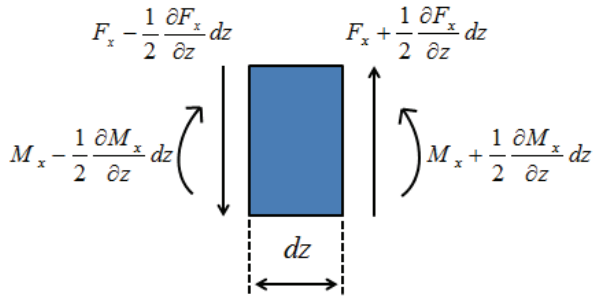


Fig. 3 Forces and moments acting on the length dz of the beam

The equilibrium equation for translations in x -direction and y -direction of the length dz of the beam is

$$\begin{cases} \rho A \frac{d^2 u_x}{dt^2} + EI_y \frac{\partial F_x}{\partial z} = 0 \\ \rho A \frac{d^2 u_y}{dt^2} + EI_y \frac{\partial F_y}{\partial z} = 0 \end{cases} \quad (1)$$

If the beam is axially symmetrical and no distributed bending moments act on the beam, the equilibrium equations for rotations about x - and y -axis of the length dz of the beam is

$$\begin{cases} F_y dz - \frac{\partial M_x}{\partial z} dz = -\rho I_y \frac{d^2 \phi_x}{dt^2} dz - 2\rho I_y \Omega \frac{d\phi_y}{dt} dz \\ F_x dz + \frac{\partial M_y}{\partial z} dz = \rho I_y \frac{d^2 \phi_x}{dt^2} dz - 2\rho I_y \Omega \frac{d\phi_x}{dt} dz \end{cases}$$

where Ω is the spin speed of the shaft and the polar moment of inertia of the cross section is $I_p = 2I_y$. Note that the first term of right-hand side of Eq. (2) means influence of inertia torques and the second term of right-hand side of Eq. (2) means influence of gyroscopic moments.

Applying Timoshenko beam model means taking into account the effect of shear deformation, therefore the flexural rotations ϕ_x and ϕ_y is yielded following.

$$\phi_y = \frac{\partial u_x}{\partial z} - \gamma_x, \phi_x = -\frac{\partial u_y}{\partial z} - \gamma_y \quad (3)$$

The shear strains γ_x and γ_y are linked to the shear forces by the relationship

$$\gamma_x = \frac{\chi F_x}{GA}, \gamma_y = \frac{\chi F_y}{GA} \quad (4)$$

where χ is a shear factor depends on the shape of the cross section, and for a circular beam it is shown

$$\chi = \frac{7 + 6\nu}{6(1 + \nu)} \quad (5)$$

where ν is Poisson's ratio.

The bending moment has no effect on the shear deformation: If the latter is accounted for, the relationship linking the bending moment to the inflected shape of the beam becomes

$$M_y = EI_y \frac{\partial \phi_y}{\partial z}, M_x = EI_y \frac{\partial \phi_x}{\partial z} \quad (6)$$

Eliminating $\phi_x, \phi_y, F_x, F_y, M_x, M_y, \gamma_x, \gamma_y$ from Eq.(1) ~ (6) and introducing the complex coordinate $u = u_x + iu_y$, yield the equation of vibration beam.

$$\begin{aligned} EI_y \frac{\partial^4 u}{\partial z^4} - \rho I_y \left(1 + \frac{E\chi}{G}\right) \frac{\partial^4 u}{\partial z^2 \partial t^2} + \frac{\rho^2 I_y \chi}{G} \frac{d^4 u}{dt^4} \\ + 2i\rho I_y \Omega \left[\frac{\partial^2}{\partial z^2} \left(\frac{du}{dt} \right) - \frac{\rho\chi}{G} \frac{d^3 u}{dt^3} \right] \\ + \rho A \frac{d^2 u}{dt^2} = 0 \end{aligned} \quad (7)$$

3.2 DERIVATION OF FREQUENCY EQUATION

By assuming that the solution of Eq. (7) is $u = q(z)e^{i\omega t}$, Eq. (7) becomes

$$EI_y \frac{\partial^4 q(z)}{\partial z^4} + \rho I_y \left[\omega^2 \left(1 + \frac{E\chi}{G} \right) - 2\omega\Omega \right] \frac{\partial^2 q(z)}{\partial z^2} + \rho \left(\omega^4 \frac{\rho I_y \chi}{G} - \omega^3 \frac{2\rho I_y \chi}{G} \Omega - \omega^2 A \right) q(z) = 0 \quad (8)$$

And then the characteristic equation

$$EI_y \left(\frac{p}{l} \right)^4 - \rho I_y \left[\omega^2 \left(1 + \frac{E\chi}{G} \right) - 2\omega\Omega \right] \left(\frac{p}{l} \right)^2 + \rho \left(\omega^4 \frac{\rho I_y \chi}{G} - \omega^3 \frac{2\rho I_y \chi}{G} \Omega - \omega^2 A \right) = 0 \quad (9)$$

The result of solving Eq. (9) for p is

$$p = \pm i p_1, \pm p_2$$

$$p_1 = \sqrt{\frac{\rho l^2}{2E} \omega \left\{ \left[\left(1 + \frac{E\chi}{G} \right) \omega - 2\Omega \right] + \sqrt{\left[\left(1 - \frac{E\chi}{G} \right) \omega - 2\Omega \right]^2 + \frac{4EA}{\rho I_y}} \right\}}$$

$$p_2 = \sqrt{\frac{\rho l^2}{2E} \omega \left\{ - \left[\left(1 + \frac{E\chi}{G} \right) \omega - 2\Omega \right] + \sqrt{\left[\left(1 - \frac{E\chi}{G} \right) \omega - 2\Omega \right]^2 + \frac{4EA}{\rho I_y}} \right\}} \quad (10)$$

By using p_1, p_2 the shape function $q(z)$ is

$$q(z) = C_1 \sin p_1 \frac{z}{l} + C_2 \cos p_1 \frac{z}{l} + C_3 \sinh p_2 \frac{z}{l} + C_4 \cosh p_2 \frac{z}{l} \quad (11)$$

Because boundary conditions on each ends of beam are free, $F_x = F_y = M_x = M_y = 0$ holds for $z = 0, l$. By substituting it to Eq.(2),(3),(6), the following condition for $q(z)$ is obtained

$$\frac{\partial^2 q(z)}{\partial z^2} = 0, \frac{\partial^3 q(z)}{\partial z^3} = Q \frac{\partial q(z)}{\partial z} \quad (z = 0, l)$$

$$\left(Q = \frac{\omega \rho (2\Omega - \omega)}{E} \right) \quad (12)$$

Applying these condition to Eq. (11) gives the equation of frequency

$$1 - \cos p_1 \cosh p_2 - \frac{p_2^2 (p_1^2 + l^2 Q)^2 - p_1^2 (p_2^2 - l^2 Q)^2}{2 p_1 p_2 (p_1^2 + l^2 Q) (p_2^2 - l^2 Q)} \times \sin p_1 \sinh p_2 = 0 \quad (13)$$

and the i th shape function

$$q_i(z) = \left[\sin p_{1i} \frac{z}{l} + \frac{p_{1i} p_{1i}^2 + l^2 Q_i}{p_{2i} p_{2i}^2 - l^2 Q_i} \sinh p_{2i} \frac{z}{l} - \frac{p_{2i} (p_{1i}^2 + l^2 Q_i) \sinh p_{2i} - p_{1i} (p_{2i}^2 - l^2 Q_i) \sin p_{1i}}{p_{1i} (p_{2i}^2 - l^2 Q_i) \cosh p_{2i} - p_{1i} (p_{2i}^2 - l^2 Q_i)} \cos p_{1i} \frac{z}{l} + \left(\frac{p_{1i}}{p_{2i}} \right) \cosh p_{2i} \frac{z}{l} \right]$$

Eq. (13) is used to describe a Campbell diagram and find natural frequencies.

4. RESULT

Table 2 Parameter

	Parameter	Value
ρ	Density	7850 [kg/m ³]
l	Shaft Length	0.22 [m]
A	Cross-sectional Area	1.54×10^{-2} [m ²]
I_y	Moment of Inertia of Area	1.8857×10^{-5} [m ⁴]
E	Young's Modulus	2.00×10^9 [N/m ²]
G	Transverse Elasticity Coefficient	7.6923×10^8 [N/m ²]
ν	Poisson's ratio	0.3
χ	Tymoshenko's Shear Coefficient	1.1282
u	Complex Expression of deflection	variable
z	Axial Displacement	variable
Ω	Rotational angular velocity	variable

Figure 4 illustrates the Campbell diagram of shaft and the natural frequency of 1st, 2nd and 3rd mode is shown Table 2.

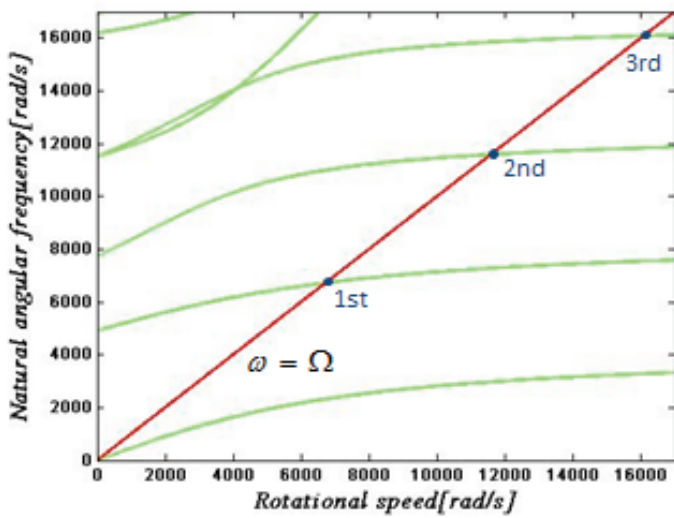


Fig. 4 Campbell diagram

Table 3 Natural frequency of system obtained experimentally

	Frequency [rad/s]
1 st Resonance	6.718×10^3
2 nd Resonance	1.157×10^4
3 rd Resonance	1.612×10^4

In order to match the result with experimental data, l and shaft radius (i.e. A and I_y) are adjusted when natural frequency is calculated. However, natural frequency of 3rd mode is not coincide with experimental data.

5. CONCLUSION

The rotational speed dependence of natural frequency is shown in the Campbell diagram. For 1st and 2nd mode with adjusting parameters, the natural frequency derived analytically is coincide with experimental data.

REFERENCES

- [1] Model identification, updating, and validation of an active magnetic bearing high-speed machining spindle for precision machining operation, Adam C. Wroblewski, August, 2011
- [2] Dynamics of Rotating Systems, Giancarlo Genta, Springer

OPTIMIZATION OF DEPOSITION CONDITIONS OF HCP Zr

Shunsuke Okumura

Graduate School of Engineering, Nagoya University

Okumura.shunsuke@j.mbox.nagoya-u.ac.jp

Supervisor: Suneel Kodambaka

Department of Material Science and Engineering,

Graduate school of Engineering, UCLA

kodambaka@ucla.edu

ABSTRACT

To deposit ZrC (111) that has variable resistances, Zr single-crystal which has hexagonal structure is needed as a buffer layer. To deposit this Zr that has high quality, it is necessary to optimize deposition temperature and time. 2 experiments showed that 750°C is the best deposition temperature and that it takes 120 min to deposit Zr completely. This will help to deposit ZrC (111).

Undisclosed

Laser beams for 2D and 3D Worm Tracker

Ikuya Onozato

Department of Mechanical engineering, Graduate School of Nagoya University
onozato@upr.mech.nagoya-u.ac.jp

Supervisor: Katsushi Arisaka

Professor of Physics and Astronomy, UCLA
arisaka@physics.ucla.edu

ABSTRACT

"Why are we conscious?" This is the most challenging question all scientific questions. At least we know that consciousness is somehow resulted from neural activities deep in our brain. But the neuron network of human is complicated, so we observed *C.elegans* which has very simple neuron network. To address these fundamental questions, we are trying to understand its behavior in 2D and 3D space under external physical stimulations, such as lights, electric, mechanical force, temperature and humidity. In addition, we are trying to understand the true origin of consciousness by physics laws. We chose light stimulation as the method to observe the behavior and the neuron network of *C.elegans* at the same time. We used 405 nm laser for this experiment and calibrated the laser. In this paper, we explained how to calibrate the laser and the worm tracker movies we took.

Undisclosed

Thermoresponsive NanoVelcro Substrate Technology for CTC Purification and AR-v7 Mutation Analysis of Castration-Resistant Prostate Cancer

Asami Yokoyama

(Affiliation) Graduate School of Engineering, Nagoya University
Yokoyama.asami@j.mbox.nagoya-u.ac.jp

Supervisor: Hsian-Rong Tseng

(Affiliation) Department of Molecular and Medical Pharmacology, UCLA
HRTseng@mednet.ucla.edu

ABSTRACT

Prostate cancer is the one of the common cancers in American male both for incidence and deaths. Androgen is deeply related to prostate cancer progression and AR-targeting agents (enzaltamide, abiraterone) are widely used for metastatic castrate-resistant prostate cancer (CRPC) treatment. But some patients have no response to these regents and this resistance is associated with expression of androgen-receptor splice variant 7 messenger RNA (AR-v7). We focused on circulating tumor cells (CTCs) which are found in the peripheral blood and easily accessed without invasive surgery. We have demonstrated that CTCs of CRPC patients who have shown resistance to the treatment of abiraterone or enzaltamide may have aberrant expression of AR-v7. However, detecting CTCs is still challenging due to the low concentration in blood. In the current study, we has demonstrated that CTCs isolation and the following mRNA mutational analysis for AR-v7 in CRPC using thermoresponsive NanoVelcro substrate is very effective strategy. Using this system we successfully detected expression of either AR-FL or AR-v7 from 8 prostate cancer patients' blood biopsies. This result would provide very useful information for patient care and development of treatment strategies.

Undisclosed

<3> Research Presentations

- For 2014 Long-term course
---The 13th JUACEP Workshop
- For 2015 Short-term course
---The 15th JUACEP Workshop
- For 2015 Medium-term course
---The 16th JUACEP Workshop

The 13th JUACEP Workshop

for the summer research course students of University of Michigan and a long-term course student of Nagoya University

Date: Thursday, August 6, 2015

Venue: VBL Hall

[Timetable]

- 13:40 - 13:45 **Opening address**
- 13:45 - 14:00 (1) **Fang Dai**, *Suzuki Lab, Mechanical Science and Engineering*
 “Implementation and Parameters Identification of Wiedemann Vehicle Following Model”
- 14:00 - 14:15 (2) **Ulka Dandekar**, *Asanuma lab, Molecular Design and Engineering*
- 14:15 - 14:30 (3) **Haodong Shen**, *Nishizawa Lab, Quantum Engineering*
 “All-Polarization-Maintaining Er-Doped Ultrashort-Pulse Fiber Laser Using Carbon Nanotube Saturable Absorber”
- 14:30 - 14:45 (4) **Hanyi Xie**, *Umehara Lab, Mechanical Science and Engineering*
- 14:45 - 15:00 (5) **Goutham Thangaraj**, *Shiokawa Lab, Solar-Terrestrial Environment Lab*
 “Extraction and Analysis of Trigger Rate and Pedestal Data from SciCRT”
- 15:00 - 15:10 Break
- 15:10 - 15:30 (6) **Emanuel Chirayath/ Chadwick Harvey**, *Kasahara Lab, Aerospace Engineering*
 “Design, Development, and Testing of a Rotating Detonation Gas-Turbine Engine”
- 15:30 - 15:45 (7) **Jiahong Ju**, *Matsumura Lab, Electrical Engineering and Computer Science*
 “Investigation of Performance of the Modified MCCB with A New-Developed Fault Current Limiter in Low Voltage DC Distribution System”
- 15:45 - 16:00 (8) **Chen Wang**, *Matsumoto Lab, Mechanical Science and Engineering*
 “A Study on Topology Optimization with FEM Based on Level Set Method”
- 16:00 - 16:15 (9) **Yuting Gao**, *Naruse Lab, Mechanical Science and Engineering*
 “Analytical Study on Combustion Kinetics of Various Solid Fuels/Waste Products”
- 16:15 - 16:30 Break
- 16:30 - 16:45 (10) Shun Arakane, mentored by Prof. J Guo, Univ. Michigan** N/A
 “Fabrication of Radio Frequency Devices by Use of 3D Printing Technology”
- 16:45 - 17:00 (11) **Yalim Yildirim**, *Hasegawa Lab, Micro-Nano Systems Engineering*
 “Quasi-Passive Elastic Exoskeleton Control Based on Mechanical Joint Kinematics”
- 17:00 - 17:15 (12) **Xudong Hao**, *Yamada lab, Mechanical Science and Engineering*
 “Evaluation of Contact States Using a Wound Testing System with Slip and Force Sensors for Estimating Skin Scratch Risks”
- 17:15 - 17:30 (13) **Andrea Manoppo**, *Arai Lab, Micro-Nano Systems Engineering*
 “The Fabrication of Tissue Engineered Small Blood Vessels via 3-Dimensional Cellular Self-Assembly and Organization In Vitro”
- 17:30 - 17:40 **Completion Ceremony**
- 18:00 - 20:00 **Farewell Banquet at VBL Hall**

**10 minutes presentation + 4 minutes Q&A each (except Presentation (6): 15 minutes presentation)*

The 15th JUACEP Workshop

--- 2015 Short-term Course at University of Michigan and UCLA---

~Open to all the JUACEP related labs and members~

Date & Time: Friday, 2nd October, 14:55~

Place: Lecture Room 231 (Room 351, 3rd floor, Eng. Bldg. 2)

Timetable:

Time	Name (Affiliation at NU)	Presentation title *tentative	US Advisor
14:55	Opening address by Prof. Umehara		
15:00	Asami Yokoyama (Baba Lab, Applied Chemistry)	“Thermoresponsive NanoVelcro Substrate Technology for CTC Purification and AR-v7 Mutation Analysis of Castration-Resistant Prostate Cancer” <div style="text-align: right; border: 1px solid black; padding: 2px;">N/A</div>	Prof. Hsian-Rong Tseng (Molecular and Medical Pharmacology, UCLA)
15:15	Junya Kato (Inoue Lab, Mech. Sci. and Eng.)	“Dynamics of A Rotating Shaft In Magnetic Bearings” <div style="text-align: right; border: 1px solid black; padding: 2px;">P.73</div>	Prof. Tsu-Chin Tsao (Mechanical and Aerospace Engineering, UCLA)
15:30	Ikuya Onozato (Shamoto Lab, Mech. Sci. and Eng.)	“Laser beams for 2D and 3D worm tracker” <div style="text-align: right; border: 1px solid black; padding: 2px;">N/A</div>	Prof. Katsushi Arisaka (Physics and Astronomy, UCLA)
15:45	Shunsuke Okumura (Umehara Lab, Mech. Sci. and Eng.)	“Deposition of Zr single-crystal” <div style="text-align: right; border: 1px solid black; padding: 2px;">N/A</div>	Prof. Suneel Kodambaka (Materials Science and Engineering, UCLA)
16:00	Shintaro Oyama (Umehara Lab, Mech. Sci. and Eng.)	“Effects of micropores on Pseudocapacitive Charge Storage in Vanadium Nitride” <div style="text-align: right; border: 1px solid black; padding: 2px;">P.75</div>	Prof. Levi Thompson (Chemical Engineering, U. Michigan)
16:20	Closing address by Prof. Umehara		

*10 mins. presentation + 4 mins. Q&A each

Attendees:

Prof. Yoshinobu Baba, Applied Chemistry

Prof. Tsuyoshi Inoue, Mechanical Science and Engineering

Prof. Takashi Ueda, Mechanical Science and Engineering

Prof. Noritsugu Umehara, Mechanical Science and Engineering (JUACEP Leader)

Prof. Yang Ju, Mechanical Science and Engineering (JUACEP Co-leader)

Assoc. Prof. Yasumasa Ito, Mechanical Science and Engineering (JUACEP)

Prof. Duane Kindt, Nagoya University of Foreign Studies (Academic English Lecturer)

The 16th JUACEP Workshop

--- 2015 Medium-term Course at University of Michigan and UCLA---

Date & Time: Thursday, 4th February, 2016 14:00~

Place: Lecture Room 241 (4th floor, Eng. Bldg. 2-South)



Timetable:

Time	Name (Affiliation at NU)	Presentation title	US Advisor
14:00	Opening address by JUACEP Leader		
14:10	Takamichi Suhara (Usami Lab., Materials, Physics and Energy Engineering)	Electrical Transport Properties of Undoped BaSi ₂ Evaporated Thin Films P.78	Prof. Kang Wang (Electrical Engineering, UCLA)
14:25	Masaki Sato (Kobashi Lab., Materials, Physics and Energy Engineering)	Growth and Characterization of Single-Crystalline Zr(0002)/Al ₂ O ₃ (0001) and ZrC(111)/Al ₂ O ₃ (0001) Thin Films N/A	Prof. Suneel Kodambaka (Materials Science and Engineering, UCLA)
14:40	Takahiro Hatano (Ju Lab., Mechanical Science and Engineering)	Micro/Nano Sensing on Diamond Tip Using Microwave P.80	Prof. Xiaochun Li (Mechanical and Aerospace Engineering, UCLA)
14:55	Michihiro Kanie (Hata Lab., Micro-Nano Systems Engineering)	3D-Printing of Porous and Solid Silicone Structure N/A	Prof. Albert Shih (Biomedical Engineering, U. Michigan)
15:10	Yusuke Kasai (Arai Lab., Micro-Nano Systems Engineering)	Duration of Trapped Air in Single Trench under Turbulent Flow N/A	Prof. C-J. Kim (Mechanical and Aerospace Engineering, UCLA)
15:25	Break		
15:40	Ryo Yamaguchi (Umehara Lab., Mechanical Science and Engineering)	Physical Aging of Star-Shaped Polymer Nanocomposites N/A	Prof. Peter Green (Materials Science and Engineering, U. Michigan)
15:55	Hiroto Izuoka (Umehara Lab., Mechanical Science and Engineering)	Nanofluidic Surface Enhanced Raman Scattering Detectors for Gas Sensing P.82	Prof. Xiaogan Liang (Mechanical Engineering, U. Michigan)
16:10	Taichi Nakao (Umehara Lab., Mechanical Science and Engineering)	Chemical Vapor Deposition of MoS ₂ Monolayers and Gr/MoS ₂ Bilayers P.84	Prof. Suneel Kodambaka (Materials Science and Engineering, UCLA)
16:25	Takamasa Horibe (Yoshikawa Lab., Aerospace Engineering)	Haptic Device with Series Elastic Actuator P.86	Prof. Brent Gillespie (Mechanical Engineering, U. Michigan)
16:40	Shogo Okishio (Nagano Lab., Aerospace Engineering)	Property Review and Thermal Conductivity Measurement on Lunar Regolith and Regolith Simulant P.89	Prof. Laurent Pilon (Mechanical and Aerospace Engineering, UCLA)
16:55	Kiichi Okuno (Umehara Lab., Mechanical Science and Engineering)	Vibration-Based Identification of Interphase Properties of Fiber Reinforced Plastics N/A	Prof. Bogdan Epureanu (Mechanical Engineering, U. Michigan)
17:10	Completion Ceremony Adjournment		

* 10 mins. presentation + 4 mins. Q&A each


The 15th JUACEP workshop
October 2, 2015

**Dynamics of a Rotating Shaft
in Magnetic Bearings**

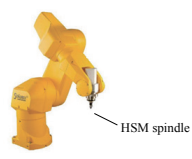

Mechanical and Aerospace Engineering Department Department of Mechanical Science and Engineering
 Mechtronics and Controls Laboratory Mechtronics and Dynamics Gr. Inoue Laboratory

Junya Kato


The 15th JUACEP workshop UCLA &  JUACEP 1

Introduction

- ✓ HSM (High-Speed Machining)
 - Shorter machining cycles
 - Higher part accuracy
 - Better surface finishes
 - Lower production costs
- ✓ AMBs (Active Magnetic Bearings)
 - Contactless
 - Active control capability

➡ High speed and High quality operation

The 15th JUACEP workshop UCLA &  JUACEP 2


Objective

- ✓ In order to realize reliable and optimal machining performance
 - Accuracy of the spindle model ➡ Necessary
 - Carefully selected parameters ➡ Necessary
- Natural Frequency ➡ Depends on rotational speed
- ✓ Previous research: Obtained experimentally

➡ By deriving Natural frequency analytically for simplified model

Objective:

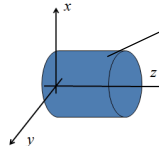
- Checking the rotational speed dependence
- Comparing experimentally data

The 15th JUACEP workshop UCLA &  JUACEP 3

Equation of A Vibration Beam

✓ Equilibrium equation in x, y


➢ For translations

$$\begin{cases} \rho A \frac{d^2 u_x}{dt^2} + EI_y \frac{\partial F_x}{\partial z} = 0 \\ \rho A \frac{d^2 u_y}{dt^2} + EI_x \frac{\partial F_y}{\partial z} = 0 \end{cases}$$


➢ For rotations

$$\begin{cases} F_x dz - \frac{\partial M_x}{\partial z} dz = -\rho I_y \frac{d^2 \phi_x}{dt^2} dz - 2\rho I_y \Omega \frac{d\phi_x}{dt} dz \\ F_y dz + \frac{\partial M_y}{\partial z} dz = \rho I_x \frac{d^2 \phi_y}{dt^2} dz - 2\rho I_x \Omega \frac{d\phi_y}{dt} dz \end{cases}$$

Inertia Torque Gyroscopic Moment

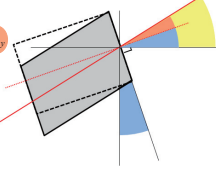
The 15th JUACEP workshop UCLA &  JUACEP 4

Equation of A Vibration Beam

✓ Timoshenko beam

- Flexural rotations $\phi_x = \frac{\partial u_x}{\partial z} - \gamma_x, \phi_y = \frac{\partial u_y}{\partial z} - \gamma_y$
- Shear strains $\gamma_x = \frac{\chi F_x}{GA}, \gamma_y = \frac{\chi F_y}{GA}$


$\chi = \frac{7 + 6\nu}{6(1 + \nu)}$ (For circular cross section)
Poisson's ratio



✓ Equation of motion of a vibration beam

$$EI_y \frac{\partial^4 u}{\partial z^4} - \rho I_y \left(1 + \frac{E\chi}{G} \right) \frac{\partial^4 u}{\partial z^2 \partial t^2} + \frac{\rho^2 I_y \chi}{G} \frac{d^4 u}{dt^4} + 2i\rho I_y \Omega \left[\frac{\partial^2}{\partial z^2} \left(\frac{du}{dt} \right) - \frac{\rho \chi}{G} \frac{d^3 u}{dt^3} \right] + \rho A \frac{d^2 u}{dt^2} = 0$$

(with the complex coordinate $u = u_x + iu_y$)

The 15th JUACEP workshop UCLA &  JUACEP 5

Variable Separation Method

✓ Equation of motion

$$EI_y \frac{\partial^4 u}{\partial z^4} - \rho I_y \left(1 + \frac{E\chi}{G} \right) \frac{\partial^4 u}{\partial z^2 \partial t^2} + \frac{\rho^2 I_y \chi}{G} \frac{d^4 u}{dt^4} + 2i\rho I_y \Omega \left[\frac{\partial^2}{\partial z^2} \left(\frac{du}{dt} \right) - \frac{\rho \chi}{G} \frac{d^3 u}{dt^3} \right] + \rho A \frac{d^2 u}{dt^2} = 0$$

Substitute: $u = q(z)e^{i\omega t}$ $q(z) = \exp(pz/l)$


✓ Characteristic equation

$$EI \left(\frac{p}{l} \right)^4 - \rho I \left[\omega^2 \left(1 + \frac{E\chi}{G} \right) - 2\omega\Omega \right] \left(\frac{p}{l} \right)^2 + \rho \left(\omega^4 \frac{\rho I \chi}{G} - \omega^3 \frac{2\rho I \chi}{G} \Omega - \omega^2 A \right) = 0$$

➡

✓ Eigenvalue $p = \pm i p_1, \pm p_2$

$$p_1 = \sqrt{\frac{\rho I}{2E} \omega \left[\left(1 + \frac{E\chi}{G} \right) \omega - 2\Omega \right] + \left[\left(1 - \frac{E\chi}{G} \right) \omega - 2\Omega \right]^2 + \frac{4EA}{\rho I}}; p_2 = \sqrt{\frac{\rho I}{2E} \omega \left[\left(1 + \frac{E\chi}{G} \right) \omega - 2\Omega \right] + \left[\left(1 - \frac{E\chi}{G} \right) \omega - 2\Omega \right]^2 + \frac{4EA}{\rho I}}$$

The 15th JUACEP workshop UCLA &  JUACEP 6

Equation of Frequency

✓ **Mode function**

$$q(z) = C_1 \sin p_1 \frac{z}{l} + C_2 \cos p_1 \frac{z}{l} + C_3 \sinh p_2 \frac{z}{l} + C_4 \cosh p_2 \frac{z}{l}$$

✓ **Boundary conditions** ($z = 0, l$)

$$F = M = 0 \rightarrow \frac{\partial^2 q(z)}{\partial z^2} = 0, \frac{\partial^3 q(z)}{\partial z^3} = Q \frac{\partial q(z)}{\partial z} \quad \left(Q = \frac{\omega l (2\Omega - \omega)}{E} \right)$$

✓ **Equation of frequency**

$$1 - \cos p_1 \cosh p_2 - \frac{p_2^2 (p_1^2 + l^2 Q^2) - p_1^2 (p_2^2 - l^2 Q^2)}{2 p_1 p_2 (p_1^2 + l^2 Q^2) (p_2^2 - l^2 Q^2)} \sin p_1 \sinh p_2 = 0$$

The 15th JUACEP workshop
UCLA & JUACEP 7

How to Obtain Natural Frequency

Eigen value

$$p_1 = \sqrt{\frac{\rho l^2}{2E} \omega \left[\left(1 + \frac{E\chi}{G} \right) \omega - 2\Omega \right] + \sqrt{\left(1 - \frac{E\chi}{G} \right) \omega - 2\Omega}^2 + \frac{4EA}{\rho l^2}}$$

$$p_2 = \sqrt{\frac{\rho l^2}{2E} \omega \left[\left(1 + \frac{E\chi}{G} \right) \omega - 2\Omega \right] + \sqrt{\left(1 - \frac{E\chi}{G} \right) \omega - 2\Omega}^2 + \frac{4EA}{\rho l^2}}$$

Equation of frequency

$$1 - \cos p_1 \cosh p_2 - \frac{p_2^2 (p_1^2 + l^2 Q^2) - p_1^2 (p_2^2 - l^2 Q^2)}{2 p_1 p_2 (p_1^2 + l^2 Q^2) (p_2^2 - l^2 Q^2)} \sin p_1 \sinh p_2 = 0$$

Implicit function: $f(\omega, \Omega) = 0$

Campbell diagram

The 15th JUACEP workshop
UCLA & JUACEP 8

Experimental Natural Frequency

	Natural Frequency [rad/s]
1 st Resonance	6.717×10^3
2 nd Resonance	1.228×10^4
3 rd resonance	2.017×10^4

cf. Model identification, updating, and validation of an active magnetic bearing high-speed machining spindle for precision machining operation, Adam C. Wroblewski, August, 2011

The 15th JUACEP workshop
UCLA & JUACEP 9

Result

✓ 1st and 2nd mode

⇒ Coincident

✓ 3rd mode

⇒ Not coincident

	Experimental [rad/s]	Analytical [rad/s]
1 st Resonance	6.717×10^3	6.718×10^3
2 nd Resonance	1.228×10^4	1.157×10^4
3 rd resonance	2.017×10^4	1.612×10^4

The 15th JUACEP workshop
UCLA & JUACEP 10

Conclusion

With simplified shaft model

- ✓ By applying Timoshenko beam model, the rotational speed dependence of natural frequency is checked
- ✓ The 1st and 2nd mode's natural frequencies obtained in this study are coincidence with the experimentally data

The 15th JUACEP workshop
UCLA & JUACEP 11

MICHIGAN ENGINEERING UNIVERSITY OF MICHIGAN

NAGOYA UNIVERSITY

Effects of Micropores on Pseudocapacitive Charge Storage in Vanadium Nitrides

Shintaro Oyama
1st Year Graduate Student in Mechanical Engineering, Nagoya University
Supervisor : Prof. Levi T. Thompson

Thompson Research Group

JUACEP

Background 2/16

Need for Energy Storage Devices

Applications

Power storage Electric vehicle Lap top Cell phone

↓

Currently available energy storage devices are **NOT enough!**

⇒ Demand High Power density electrical storage device
Energy

MICHIGAN ENGINEERING UNIVERSITY OF MICHIGAN JUACEP

Background 3/16

Need for Energy Storage Devices

Supercapacitors (Electrochemical Capacitors)

- High power density
- Short charge time
- Long cycle life

Specific energy vs Specific power [1]

[1] Patrice, S et al., Nature Materials, Vol.7, pp. 845-854 (2008).

MICHIGAN ENGINEERING UNIVERSITY OF MICHIGAN JUACEP

Background 3/16

Need for Energy Storage Devices

Supercapacitors (Electrochemical Capacitors)

- High power density
- Short charge time
- Long cycle life

☹ Low energy density

Need to boost energy density

Specific energy vs Specific power [1]

[1] Patrice, S et al., Nature Materials, Vol.7, pp. 845-854 (2008).

MICHIGAN ENGINEERING UNIVERSITY OF MICHIGAN JUACEP

Background 4/16

Early Transition Metal Nitrides and Carbides

Advantages

- ✓ Low cost
- ✓ High electronic conductivities
- ✓ High accessible surface areas
- ✓ High Capacitances (derived from pseudocapacitance)

Some group 4,5 & 6 early transition metals

Material	Electronic conductivity [S μ m]	Surface area [m ² /g]	Accessibility	Electrolyte	Capacitance [F/g]	Specific Capacitance [μ F/cm ²]	Charge Storage Mechanism
Mo ₂ N	50	150	○	H ₂ SO ₄	350	233	Double layer + Pseudocapacitance
VN	12	38	○	KOH	1340	3526	Double layer + Pseudocapacitance
Carbon(AC295)	< 0.3	3261	×	EMImBF ₄	350	11	Double layer

MICHIGAN ENGINEERING UNIVERSITY OF MICHIGAN JUACEP

Background 5/16

Pseudocapacitance Derives from Micropores

High density of H⁺ adsorption in micropores during charge storage

[1] A. Djire et. al., in preparation

MICHIGAN ENGINEERING UNIVERSITY OF MICHIGAN JUACEP

Purpose 6/16

Hypothesis
 High pseudocapacitances observed for nitrides in aqueous media derived from the insertion of H^+ & OH^- into small pores (micropores)

Material	Electrolyte	Capacitance c [F/g]	Specific Capacitance c^s [$\mu F/cm^2$]	Charge Storage Mechanism
Mo ₂ N	H ₂ SO ₄	350	233	Double layer + Pseudocapacitance
VN	KOH	1340	3526	Double layer + Pseudocapacitance

Yves et al. (Summer 2015)

This research

Approach
 Examine the effect of pore size on the pseudocapacitive storage for VN in aqueous media

M MICHIGAN ENGINEERING UNIVERSITY OF MICHIGAN JUACEP

Experimental methods 7/16

Material Synthesis
 Oxide precursor (V₂O₅) $\xrightarrow{NH_3}$ Vanadium Nitride (VN) $\xrightarrow{1\% O_2/He @ RT}$ Passivated VN

Temperature Programmed Reaction (TPR)

Physical Characterization
 XRD (X-Ray Diffraction) Phase purity
 Nitrogen Physisorption Surface area, Pore size distribution

Electrode Preparation
 Material mix with Super PLI and PVDF
 Ti Plate
 Active Material Coating
 Dry in vacuum @ 80°C for 8 hours

Electrochemical Characterization
 Electrochemical Cell
 Cyclic Voltammetry
 Redox activities, Stable operating window, Capacitance

M MICHIGAN ENGINEERING UNIVERSITY OF MICHIGAN JUACEP

Experiment 8/16

Synthesis Condition
 Precursor : V₂O₅
 Particle size : 125 – 250 μm
 \Rightarrow Vanadium Nitride (VN)

Condition	Spe. flow rate (ml min ⁻¹ g ⁻¹)	Heating Rate β_1 (°C min ⁻¹)	Heating Rate β_2 (°C min ⁻¹)	Heating Rate β_3 (°C min ⁻¹)	Temperature T ₃ (°C)	Soak time (min)
HSA_54	10000	-	-	0.80	650	0
MSA_45	4325	3.61	0.67	1.66	700	60
MSA_35	3000	5.00	5.00	5.00	750	60
LSA_10	1333	-	-	15.0	800	480
LSA_4	500	-	-	20.0	850	720

$T_1 = 350\text{ }^\circ C, T_2 = 450\text{ }^\circ C$

M MICHIGAN ENGINEERING UNIVERSITY OF MICHIGAN JUACEP

Result 9/16

Physical Properties
 Phase Pure Vanadium Nitrides

M MICHIGAN ENGINEERING UNIVERSITY OF MICHIGAN JUACEP

Result 10/16

Physical Properties

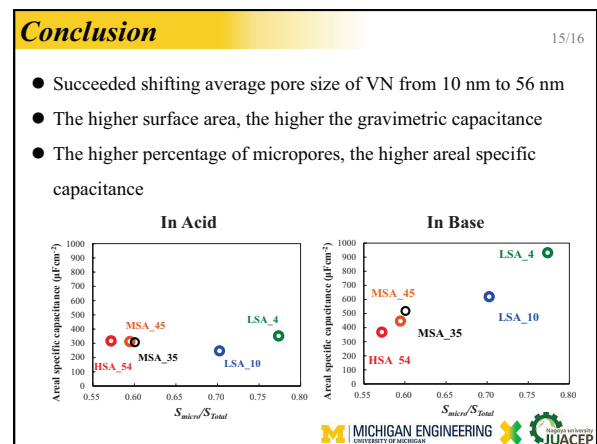
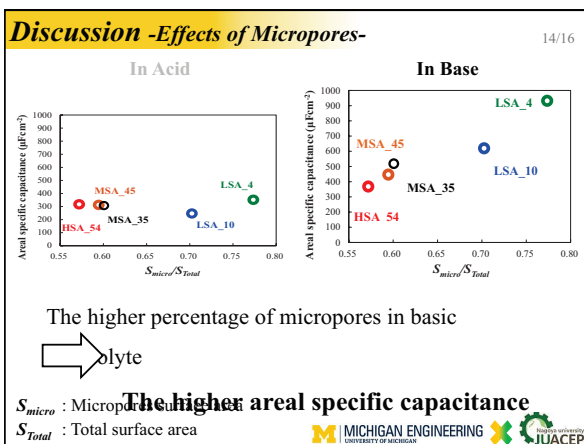
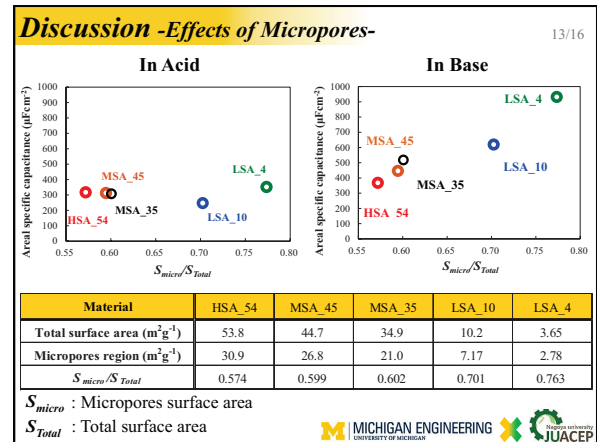
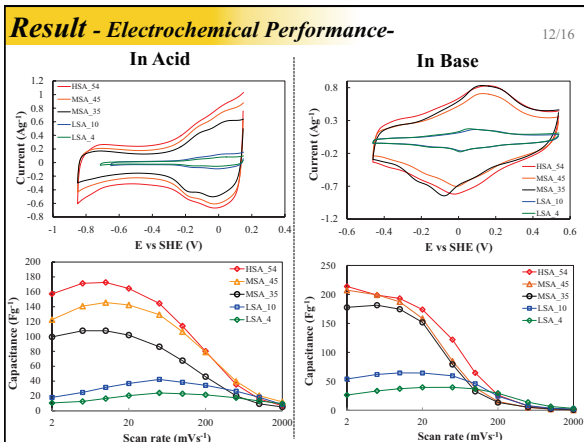
Material	Particle size (nm)	Average pore size (nm)	Total Surface area (m ² g ⁻¹)	Micropore surface area (m ² g ⁻¹)
HSA_54	111	10.0	53.8	30.9
MSA_45	134	14.0	44.7	26.8
MSA_35	172	15.0	34.9	21.0
LSA_10	587	44.4	10.2	7.17
LSA_4	1641	56.4	3.65	2.78

M MICHIGAN ENGINEERING UNIVERSITY OF MICHIGAN JUACEP

Result 11/16

Pore Size Distribution

M MICHIGAN ENGINEERING UNIVERSITY OF MICHIGAN JUACEP




Acknowledgements

16/16

- Professor Levi T. Thompson and his research group
- Abdoulaye Djire for his mentorship
- Tapiwa Mushove, Wei-Chung Wen for their help
- Japan-US Advanced Collaborative Education Program (JUACEP)


M MICHIGAN ENGINEERING UNIVERSITY OF MICHIGAN JUACEP



Electrical Transport Properties of Undoped BaSi₂ Evaporated Thin Films


Supervisor: Professor Kang L. Wang
(Department of Electrical Engineering, UCLA)

Takamichi Suhara
(Department of Materials, Physics and Energy Engineering, Nagoya University)



Introduction

- Types of Solar Cells
 - Silicon
 - Crystalline Si
 - Mono crystalline
 - Poly crystalline
 - Thin film
 - Amorphous Si
 - Chemical compound
 - Inorganic
 - GaAs
 - CIGS
 - ???
 - Organic
 - Dye-sensitized
 - Organic polymer

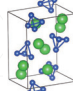


Introduction

[1] K. Toh, et al., Jpn. J. Appl. Phys. 50, 068001 (2011).

- BaSi₂ (Barium-disilicide)
 - Advantages
 - Large Optical Absorption Coefficient (10^4cm^{-1} @ $1.5 \text{eV}_{[1]}$)
 - Suitable Bandgap ($1.3 \text{eV}_{[1]}$) for single-junction solar cells
 - Ba and Si are rich in the earth

Material for **high efficient** and **low cost** solar cells.




Introduction

Growth Method of BaSi₂

MBE ↔ Thermal Vacuum Evaporation

OBJECTIVE

Evaluation of Electrical property of BaSi₂ evaporated films and Effects of post-anneal on films



Experiment

Vacuum Evaporation (Nagoya)

- Substrate - High resistance p-Si substrate ($\rho > 1000 \Omega \text{cm}$)
- Substrate temperature - 550°C
- Source - 99% BaSi₂ 0.1g → estimated thickness 100nm
- Vacuum level - under 10^{-3}Pa

↓

Post-anneal (LA)

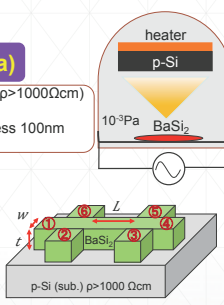
500°C 1000°C

Sample A Sample B Sample C

Electrical Evaluation (LA)

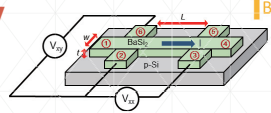
- Fabricate Hall-Bars
- Conductivity @ $1 \mu\text{A}$, 300K-100K
- Hall measurement @ $\pm 0.5 \text{T}$, $1 \mu\text{A}$, 300K-170K
 - Carrier density
 - Carrier mobility

Hall-Bar size
z: 100 nm
w: 1 mm
L: 2 mm



Conductivity

$\sigma = 1/\rho$ $\rho = tw/L R Lxx$



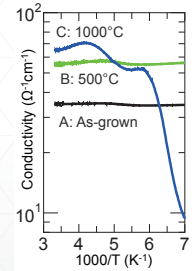
- Sample A, B: No temperature dependence
- Sample C: Conductivity decreases about one order

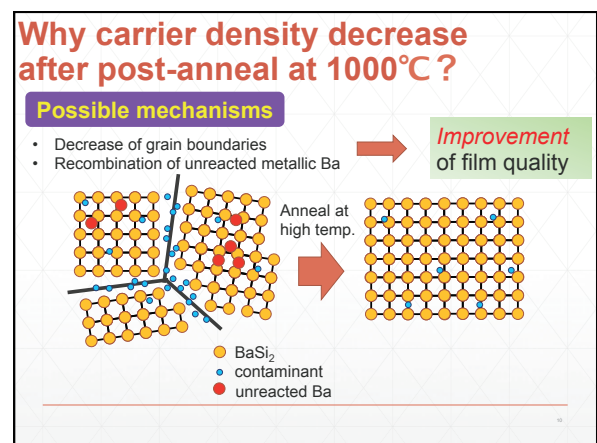
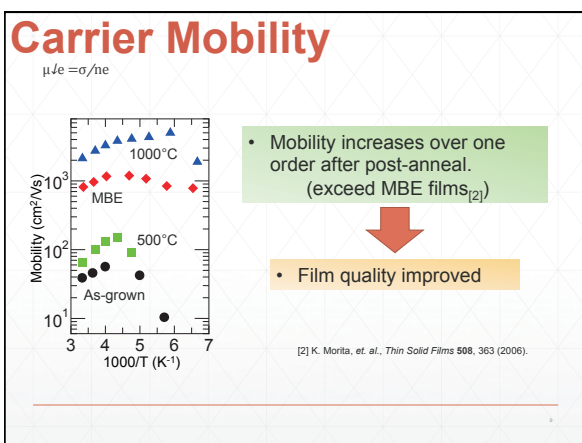
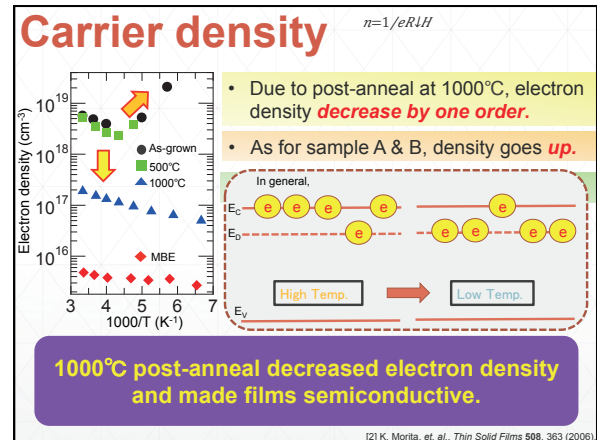
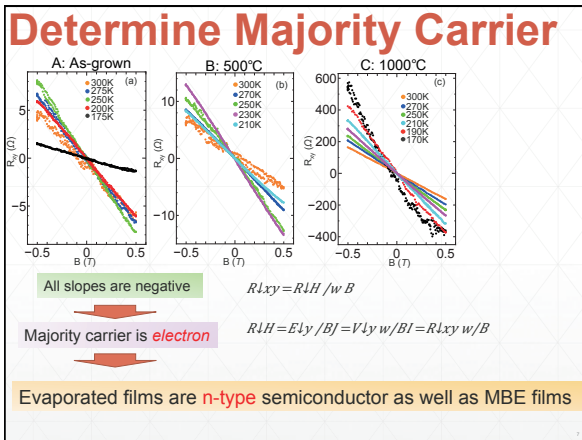
↓

Effects of post-anneal

1000°C - Films became semiconductive
= Improve film quality??

500°C - No effects
= Because 500°C is lower than growth temp.





Conclusion

- Evaporated BaSi₂ film is n-type.
- By post-anneal at 1000°C, film turn into semiconductive behavior.
- Electron density reduce due to improvement of film quality by post-anneal at 1000°C.
- Electron mobility reach MBE films after post-anneal at 1000°C.

↓

Got beneficial results for application of BaSi₂ evaporated film.

Thank you for your attention.


Micro/Nano Sensing on Diamond Tip Using Microwave

Supervisor: Prof. Xiaochun Li
2016/02/04
Takahiro Hatano

Motivation

Single Point Diamond Turning (SPDT) is key technology for rapid prototyping or small volume production of

- Spheres
- Aspheres
- Parabolic mirrors
- Cylinders
- Conical optics
- Plano optics
- Simple toroids
- Assemblies



Process of SPDT / Diamond tool

- Roughness : a few nano meters
- Object : metals, crystals, and plastics

Micro/Nano Sensing on Diamond Tip

Why do we need micro/nano sensing on diamond tip?

- The roughness of SPDT is very small; a few nano meters
- Even if the turning parameter is same, the finished surface changes a little for the difference of the conditions on diamond tip.

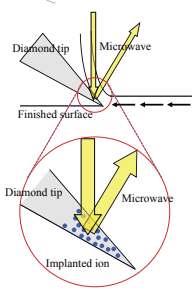
e.g. Without control With control

Temperature Temperature

Finished surface Finished surface

- To control the turning parameter and get smoother surface, we need a new sensing technique of temperature and strain on diamond tip.

Principle



- i. Ion implantation into diamond tip
- ii. Microwave irradiation to the tip
- iii. Frequency shift due to reflection by implanted ion

Microwave : low energy
Implanted ion : high energy depended on temperature and strain

When microwave is reflected by implanted ion, frequency changes.

- iv. Measurement of frequency shift

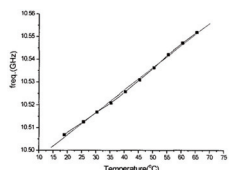
↓

By measuring the frequency shift, the conditions on diamond tip are cleared.

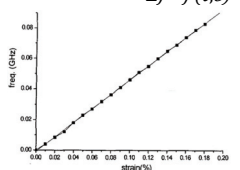
Frequency Shift

How do we know the conditions on diamond tip?

Frequency shift of microwave : Distributed temperature and strain $\Delta f = f(t, \epsilon)$



Relationship between frequency shift and temperature^[1]



Relationship between frequency shift and strain^[1]

$$\Delta f = \alpha \Delta t + \beta \Delta \epsilon \quad (\alpha, \beta : const.)$$

[1] Ji-Bum Kwon, Journal of the Optical Society of Korea, Vol. 7, No. 2, pp. 106-112 (2003)

Ion Implantation

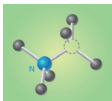
Ion Source : Nitrogen → Nitrogen-Vacancy (NV) center in diamond
Silicon → Silicon-Vacancy (SiV) center in diamond

NV center in diamond^[2]

Nanoscale temperature sensor
High temperature precision
High spatial resolution

▶ Ion implantation parameter^[2]

- Isotope : ¹⁴N
- Energy : 15 keV
- Dosage : 1×10^{13} atoms/cm²

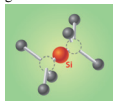


SiV center in diamond^[3, 4]

Characteristic is similar to NV center in diamond
High temperature precision

▶ Ion implantation parameter^[5]

- Isotope : ²⁸Si
- Energy : 1.5 MeV
- Dosage : 1×10^{11} atoms/cm²



[2] Pezzagna S., New Journal of Physics, 12, 065017 (2010) [3] Rogers L. J., Phys. Rev. B 89, 235101 (2014) [4] Hepp C. et al., Phys. Rev. Lett. 112, 036405 (2014) [5] Cui Jin-Ming, Generation of Nitrogen-Vacancy Centers in Diamond with Ion Implantation (2007)

Anneal

Annealing conditions can impact the NV/SiV yield efficiency and reduce the overall crystal damage defects for achieving a good NV/SiV yield efficiency.

NV center in diamond

► Annealing parameter^[2]

- Temperature : 1000 °C
- Time : 10 min

SiV center in diamond

► Annealing parameter^[5]

- Temperature : 1000 °C
- Time : 5 min

[2] Pezzagna S., New Journal of Physics, 12, 065017 (2010) [5] Cui Jin-Ming., Generation of Nitrogen-Vacancy Centers in Diamond with Ion Implantation (2007)

Simulation of Conditions on Work Tool

[6] Dirk Werschmoeller, Measurement of Transient Tool Internal Temperature Fields by Novel Micro Thin Film Sensors Embedded in Polycrystalline Cubic Boron Nitride Cutting Inserts (2010) [7] Yigit Karpat, JSME, 69-686 B, pp. 2305-2312 (2007)

Experimental Setting

1. Ion implantation

Isotope	¹⁴ N	²⁸ Si
Substrate material	Diamond	Diamond
Dose [atoms/cm ²]	1×10 ¹³	1×10 ¹¹
Energy [keV]	15	1500
Tilt angle [degree]	7	7
Annealing temperature [°C]	1000	1000
Annealing time [min]	10	5

2. Microwave measurement

Under environments as follows:

- Temperature : 500 °C
- Force : 200 N

Conclusion

- New sensing technique of temperature and strain on diamond tip using frequency shift of microwave is suggested.
- Nitrogen-Vacancy (NV) center in diamond has high temperature precision and high spatial resolution. Silicon-Vacancy (SiV) center in diamond is expected to have a high temperature precision as with NV center in diamond.
- NV center in diamond and SiV center in diamond are created by ion implantation. The most effective experimental condition of ion implantation is shown.
- In order to approach the experimental condition toward actual turning process, the temperature and cutting force of the tool in turning process is figured out.

THANK
YOU
FOR
YOUR
ATTENTION!!

Nanofluidic-Flow-Assisted-Assembly (NFAA) of Plasmonic Structures into Nanoslit Sensors

Presenter
Hiroto Izuoka
 Department of Mechanical Science and Engineering,
 Graduated School of Engineering, Nagoya University

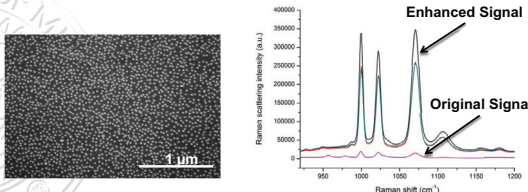
Advisor
Xiaogan Liang
 Mechanical Engineering, University of Michigan, Ann Arbor

MECHANICAL ENGINEERING UNIVERSITY OF MICHIGAN

The 16th JUACEP Workshop, 4th February 2016

Noble Metal Nanoparticles (NPs) for Plasmonic Sensing

Plasmonic Surfaces - Solid surfaces coated with NPs



Arrays of spherical AuNPs with diameter of 20 nm

Surface-enhanced Raman Scattering (SERS)

Enhanced Signal

Original Signal

Raman shift (cm⁻¹)

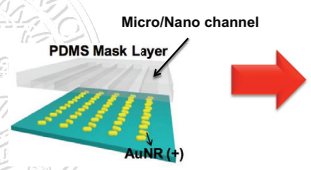
Raman scattering intensity (a.u.)

Plasmonic sensing has high detection sensitivity and low limit-of-detection (LOD) (Sensitivity can be enhanced by up to 10⁶ in SERS detection)

MECHANICAL ENGINEERING UNIVERSITY OF MICHIGAN

Problem of Integration of NPs Plasmonic and Micro/Nano fluidic Structures

Integration with Micro/Nano channel



Micro/Nano channel

PDMS Mask Layer

AuNR (+)

Low density of NPs

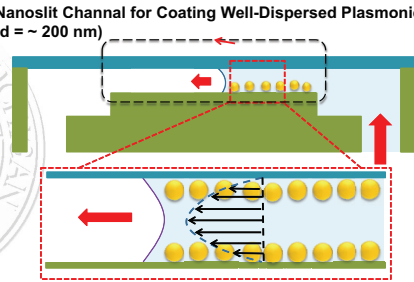
Aggregation of NPs

Chen, Pengyu, et al. "Multiplex serum cytokine immunoassay using nanoplasmonic biosensor microarrays." ACS nano 9.4 (2015): 4173-4181.

High coating density and a good dispersion of NPs stand in a trade-off to each other when NPs is integrated with micro/nano channel

MECHANICAL ENGINEERING UNIVERSITY OF MICHIGAN

Nanofluidic-Flow-Assisted-Assembly (NFAA) for Plasmonic Nanoparticles



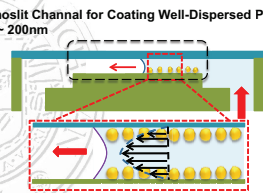
Nanoslit Channel for Coating Well-Dispersed Plasmonic NPs (d ~ 200 nm)

Highly viscous flows in nanoslit channels can result in a selective deposition of plasmonic nanoparticles from the colloidal solution into nanoslits.

MECHANICAL ENGINEERING UNIVERSITY OF MICHIGAN

Purpose of this work - Integration of Nanochannel and Plasmonic Structures

Demonstration of NFAA



Nanoslit Channel for Coating Well-Dispersed Plasmonic NPs d ~ 200nm

Spherical NPs 5 nm

Nanorods (NRs) 40 nm x 80 nm

Demonstrated Nanofluidic-Flow-Assisted-Assembly (NFAA) for AuNPs and AuNRs for subsequent plasmonic sensing

MECHANICAL ENGINEERING UNIVERSITY OF MICHIGAN

Fabrication of Nanoslit Sensors

- Starting wafer (Quartz or Si)
- Nanoslit channels with depth of d = 20-200 nm
- Microfluidic inlet/outlet structures
- Accessing holes drilled by sandblasting
- Plasma-assisted sealing
- Quartz Coverslip
- Nanofluidic-Flow-Assisted-Assembly (NFAA) for plasmonic NPs into nanoslits
- Nanoslit detector ready for plasmonic sensing

MECHANICAL ENGINEERING UNIVERSITY OF MICHIGAN

Nanoslit Channels and Microfluidic Inlet/Outlet Structures

Accessing Holes

Microfluidic Inlet/Outlet Structures

Nanoslit channel with depth of $d \sim 200$ nm and width of $w = 50$ μm

❑ We cannot use flexible films (PDMS) for sealing, because of the low aspect-ratio of nanoslit channels.

Setup for Nanofluidic-Flow-Assisted-Assembly (NFFA)

Loading Reservoirs (1 atm)

Vacuum Pressure

Acrylic Jig

3 mm

O-rings

Post Array Chip

Cover Slip

Metal Clamp

❑ Backside Nanoslit device

❑ Frontside Mini-Vacuum Chamber

Pump

Nanofluidic-Flow-Assisted-Assembly (NFAA) for 5 nm AuNPs into 90 nm Deep Nanoslit Channels

Nanoslit Channel Coated with 5 nm Au NPs

NP Solution

Microfluidic Inlet/Outlet Structures

Flow direction

5 nm Au NPs

❑ Au NPs are uniformly coated into blank nanoslit channels for subsequent sensing. (~ 200 NP/ μm^2)

Nanofluidic-Flow-Assisted-Assembly (NFAA) for 5 nm AuNPs into 90 nm Deep Nanoslit Channels

Nanoslit Channel Coated with 5 nm Au NPs

NP Solution

Microfluidic Inlet/Outlet Structures

Flow direction

5 nm Au NPs

❑ Au NPs are uniformly coated thoroughly from inlet to outlet channel

Nanofluidic-Flow-Assisted-Assembly (NFAA) for 80 nm long AuNRs into 200 nm Deep Nanoslit Channels

Nanoslit Channel Coated with 80 nm Au NRs

NR Solution

Microfluidic Inlet/Outlet Structures

Flow direction

80 nm Au NRs

❑ Au NRs are uniformly coated into blank nanoslit channels for subsequent sensing. (~ 20 NR/ μm^2)

❑ Current coating method : (~ 0.2 NR/ μm^2)

Summary and Next challenge

Summary

- fabrication/packaging of micro-/nanofluidic channel structures of the proposed detectors
- demonstrated a new nanofluidic method for selectively coating plasmonic nanoparticles into active device areas (NFAA) and successfully deposited.

5 nm Au NPs

Next challenge

- The controlling the areal density of NPs
- Evaluate the optical property, such as Quality factor and Enhancement factor, of plasmonic structures coated using NFFA

02/04/2016 JUACEP presentation

Chemical Vapor Deposition of MoS₂ Thin Layers

In situ microscopy Laboratory
 Department of Materials Science and Engineering
 University of California, Los Angeles
 Visiting Graduate Researcher
 Taichi Nakao

Advisor: Abbas Ebnonnasir
 Supervisor: Prof. Suneel Kodambaka

1.1 Two-dimensional monolayer materials

Graphene

The discovery in 2004

- High transparency
- High thermal conductivity
- High electrical conductivity
- High Young's modulus

In electronic application...
Problem
Zero bandgap material

<Trial to create a bandgap>

- Graphene nanoribbon No methods for mass-production
- Bilayer graphene

⇒ but still, there is a problem

Researchers refocus on the other 2D monolayer materials
 - to overcome the weakness of graphene for applying industry fields

In situ microscopy laboratory, University of California, Los Angeles 2/10

1.2 Transition metal dichalcogenides

Molybdenum disulfide (MoS₂)

- Semiconductor
- Monolayer MoS₂ has direct bandgap

Single-layer MoS₂ transistor in 2011

The properties of MoS₂ strongly depend on the number of layer

Understanding the mechanism and controlled synthesis of MoS₂ is necessary to make it used in practical devices

In situ microscopy laboratory, University of California, Los Angeles 3/10

1.3 Research objectives

Investigating the influence of deposition parameters to the quality of MoS₂ for developing the methods used in field of industry

Basic parameters to synthesize MoS₂ have reported (total pressure, deposition temperature, etc...)

still, we are not sure....

What's key parameter?
 What's parameter should we control?

We investigated the effects of

- surface condition
- the distance between precursors and substrates

for getting MoS₂ thin layers

In situ microscopy laboratory, University of California, Los Angeles 4/10

2.1 Thermal CVD system

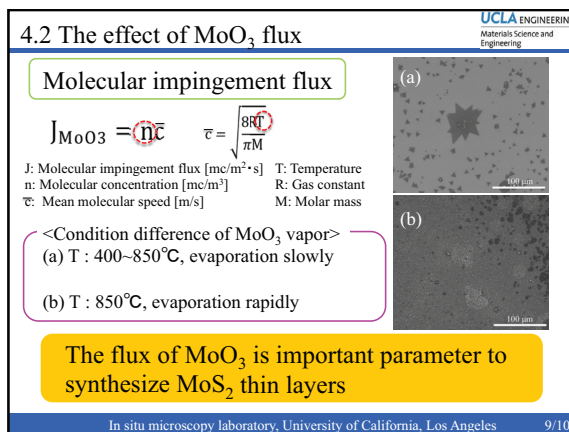
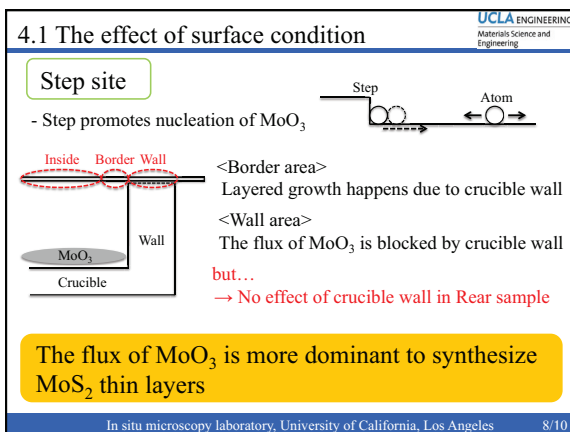
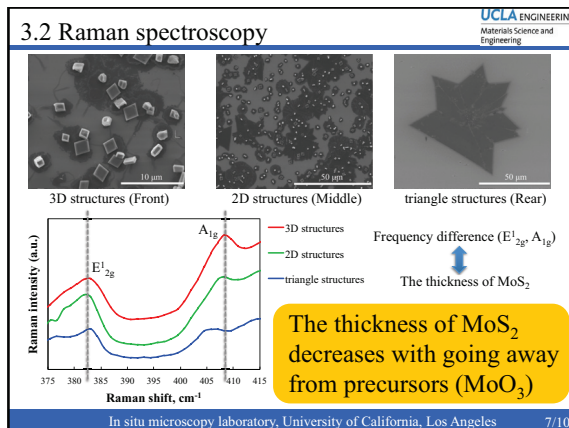
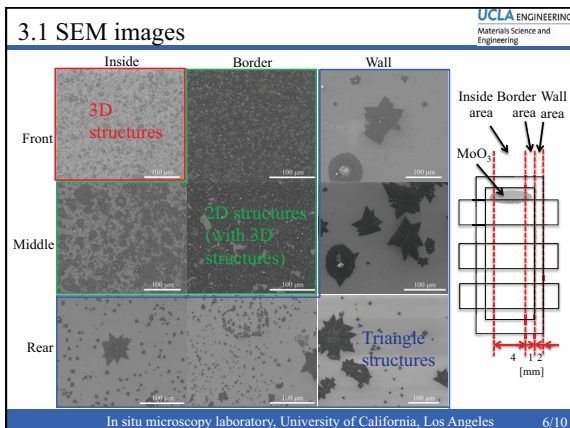
<Deposition condition>

- (i) **Pre-annealing**
 - T : 400°C, t : 10 min, Ar flow: 200 sccm Pressure : Atmosphere
- (ii) **MoO₃ deposition**
 - T : 400~850°C, t : 30 min, Ar flow: 10 sccm MoO₃ : 5 mg
- (iii) **Sulfidation**
 - T : 850°C, t : 15 min, Ar flow: 50 sccm Sulfur : 350 mg

In situ microscopy laboratory, University of California, Los Angeles 5/10

3.1 SEM images

In situ microscopy laboratory, University of California, Los Angeles 6/10



5. Conclusions

UCLA ENGINEERING
Materials Science and Engineering

- We demonstrated the synthesis of MoS₂ thin layers in thermal Chemical Vapor Deposition (CVD) System by using MoO₃ and sulfur powders as precursors.
- We investigated the effects of surface condition of substrate and the distance between MoO₃ powder and substrates to thickness and quality of MoS₂.
- We showed the high possibility that the flux of MoO₃ is key parameter to synthesize MoS₂ thin layers.

In situ microscopy laboratory, University of California, Los Angeles 10/10

Series Elasticity for Haptic Interface

Takamasa Horibe
Aerospace Engineering, Nagoya Univ.
Supervisor: Brent Gillespie
Mechanical Engineering, UoM

1
JUACEP at University of Michigan

- **Haptics:** sense of touch, human-computer interaction technology that includes the force rendering

Haptics interface: a system that allows a human to interact with a virtual environment through bodily sensations and movements

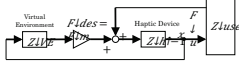


2
JUACEP at University of Michigan

- **Control Architectures for Haptic Interface**

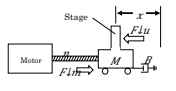
Impedance control

Force sourcing
Motion sensing



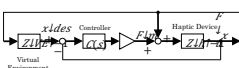
Free motion

Virtual stiffness



Admittance control

Motion sourcing
Force sensing



Free motion

Virtual stiffness

3
JUACEP at University of Michigan

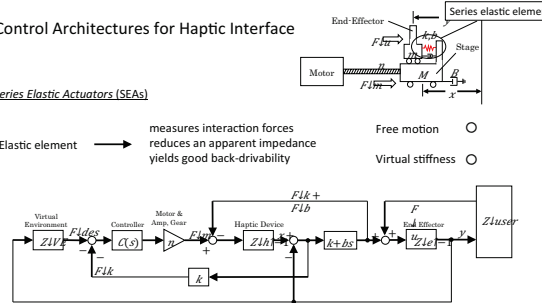
- **Control Architectures for Haptic Interface**

Series Elastic Actuators (SEAs)

Elastic element \rightarrow measures interaction forces
reduces an apparent impedance
yields good back-drivability

Free motion


Virtual stiffness



4
JUACEP at University of Michigan

- **Our Previous study**

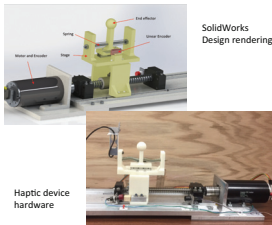
Applied the SEA idea to a rehabilitation device



Exoskeleton using pneumatic actuator

Need more basic study about "SEA for haptic interface"

- **Apparatus design**




SolidWorks Design rendering

Haptic device hardware


5
JUACEP at University of Michigan

- **Experiment**

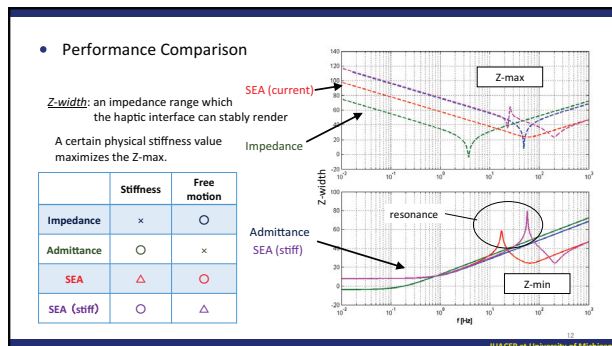
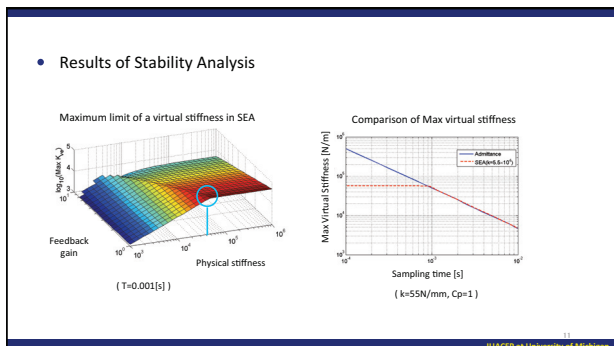
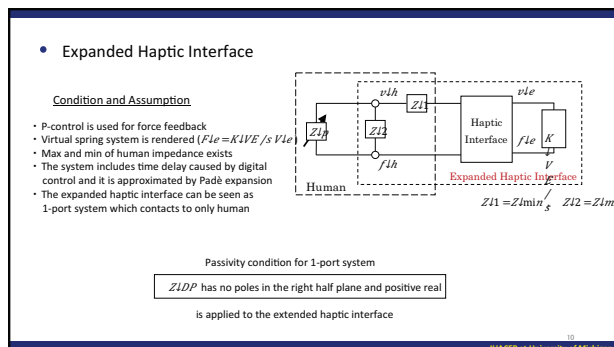
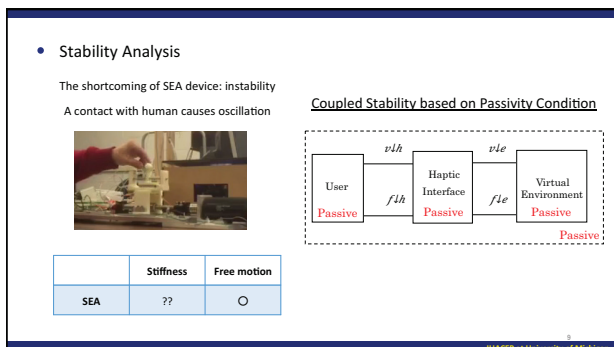
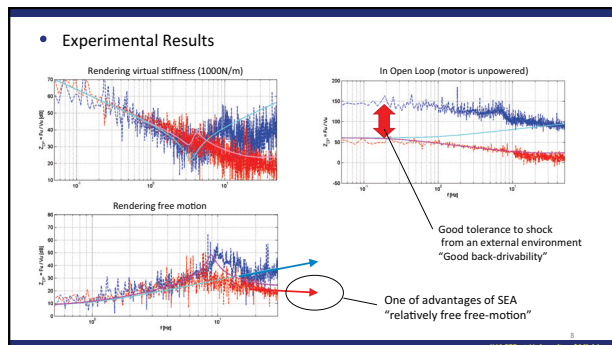
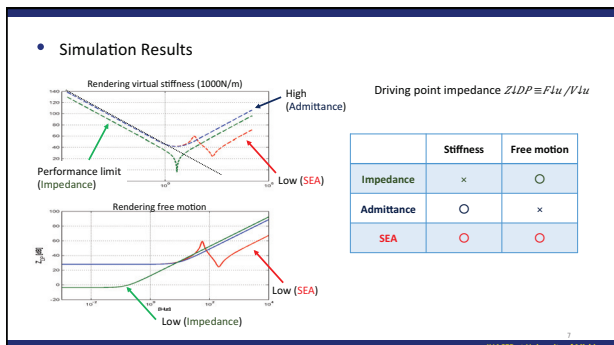
Rendering virtual spring by Admittance control



Rendering free motion by SEA



6
JUACEP at University of Michigan



- Conclusion

- Simulation and experiment validated the advantages of SEA.
- Compare the performance limit of haptic architectures based on Z-width.

- Future objective

- Applying the Series Elasticity to practical devices such as exoskeleton.

13


EMACEP at University of Michigan



Properties Review and Thermal Conductivity Measurement of Lunar Regolith and Regolith Simulant


2016/02/04
 Shogo Okishio
 Supervisor : Laurent Pilon



Contents

1. Objectives
2. Lunar Regolith and Regolith Simulant
3. Thermal Conductivity
4. Thermal Conductivity Measurement
5. Results
6. Conclusion



Objectives of This Research

Thermal conductivity measurement of powder sample using guarded hot plate method

Brief background


- The method is originally used for measuring thermal conductivity of solid materials
- Some measurements were conducted with powder materials
 - No measurements have been conducted with same powder material of different densities

Thermal conductivity measurement of regolith simulant

Regolith simulant : FJS-1 (Fuji Japanese Simulant-1)

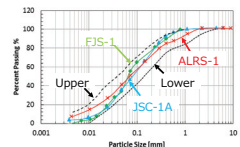
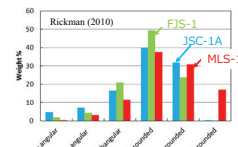
Why FJS-1?

- Only few measurements data exist and value varies
- Thermal conductivity has a pressure dependence




Lunar Regolith and Simulant

- Lunar regolith covers the lunar surface
Average particle diameter is 70 μm; angular shape; limited amount on earth
- Simulants are made to use for lunar environmental experiments
 - Simulants are made all over the world : USA, Japan, Australia etc
 - Simulants have similar components to lunar regolith
 - The particle sizes are set within the range of lunar regolith

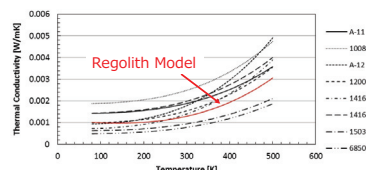
Measurements of thermal properties of these materials are important to discuss lunar thermal surface processes



Properties of Regolith


Thermal Conductivity of Lunar Regolith (Reference Research)

- Thermal conductivities of lunar regolith have been measured*
- Thermal conductivity of powder materials under vacuum can be expressed as** : $k_{eff} = A + BT^3$
- Regolith model is calculated from equation of porous media***



The model and measurement result matches well

*Cremers et al. (1970-1976) **Watson (1964) ***Notsu et al. (2014)



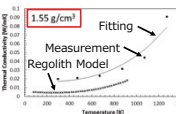
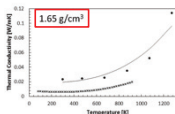
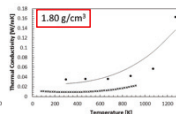
Thermal Conductivity of FJS-1

- In this research, temperature and pressure dependence of thermal conductivity of FJS-1 will be considered

Temperature Dependence

FJS-1 catalogue from the supplier had thermal conductivity measurement plot data for three densities

- Fitting was conducted : $k_{eff} = A + BT^3$
- A and B was determined for FJS-1 in each density

- Regolith model and measurement results have deviation
- Thermal conductivities of FJS-1 are higher than regolith model
- Thermal conductivity of FJS-1 differs from that of lunar regolith

Thermal Conductivity of FJS-1

➤ In this research, temperature and pressure dependence of thermal conductivity of FJS-1 will be considered

Pressure Dependence
 Results of lunar regolith, FJS-1 and regolith model were compared
 Lunar regolith : vs Depth (Langseth et al.1972) ➤ vs Pressure
 FJS-1 : Measurement by Sakatani et al (2013)

- Tendency agrees well with all results
- Pressure depended thermal conductivity of FJS-1 is lower than results of lunar regolith or regolith model

Opposite to the result of temperature dependence

The difference exist between two measurements of FJS-1
 Lack of data ➤ **FJS-1 Thermal conductivity measurement is needed**

Measurement Method

Guarded Hot Plate Method

➤ Steady state thermal conductivity measurement method

➤ Using hot plate and cold plate, the temperature gradient is made across the samples set between them

Thermal conductivity is calculated from Fourier's law

$$k_i = q_i L_i / (T_2 - T_1)$$

k_i: thermal conductivity, q: heat input, L: length between thermocouples, T: temperature

The average of the results from sample A (*k_{1A}*) and B (*k_{1B}*) is used as effective thermal conductivity (*k_{1eff}*) of the material

$$k_{1eff} = 1/2n \sum_{j=1}^{2n} k_{1j} = 1/2n (k_{1A} + k_{1B})$$

First Setup

➤ First setup was coordinated basing on the standard set up

- Plastic tube was used as the container for FJS-1
- The inner diameter of the tube was set to the diameter of plates
- Sample height was determined by considering the setting of thermocouples and creating the required temperature difference
- Both ends of tubes were sealed with plastic wraps
- Fishing lines were used to hold the thermocouples in position

First Setup

Results

➤ Density of the sample : 1.6 g/cm³

➤ Each measurement obtained three results × 2

Average 0.19W/mK

- ✓ The average value was 0.19 W/mK
- ✓ Values of thermal conductivity is compatible with other research results in atmosphere

All results showed large uncertainties

Results

Result of each measurement : Sample A and B

	T_{avg} [°C]	ΔT [°C]	k_a [W/mK]	k_b [W/mK]	k_{eff} [W/mK]	dq_{loss}	$\Delta k_{eff} / k_{eff}$
1 st	15.8	11.4	0.238	> 0.212	0.225	56%	40%
	17.9	13.2	0.219	> 0.197	0.208	58%	41%
	21.3	15.7	0.160	> 0.148	0.154	70%	50%
2 nd	13.1	8.51	0.254	> 0.195	0.224	66%	47%
	11.3	10.5	0.181	> 0.161	0.171	72%	51%
	18.0	12.5	0.167	> 0.148	0.157	75%	53%

The heat loss was calculated by subtracting heat removed by chiller water at cold plate from input heat

$$q_{loss,i} = VT / 2R - m_i c_p (T_{w2,i} - T_{w1,i}) = q_{loss} / q_{input}$$

V: Voltage, R: Resistance, m: mass flow rate, c_p: specific heat, T_{w1}: temperature of chiller water

Problems to solve

- Large heat loss causes the large uncertainty
- *k_{1A}* is always larger than *k_{1B}*
- The effect of the position in setup

Second Setup

➤ After first measurement, second setup was created

Schematic of second setup

Change from First Setup	Merit
Single-sided measurement	Only one sample is required
Direct contact between plates and sample	Prevent the heat loss from contact surface
Polystyrene for container	Lower thermal conductivity than plastic tube
Wider diameter container	Reduce the effect from outer layer
Three thermocouples per sample	Average of three results

Conclusion

- The guarded hot plate method was conducted with samples made of powder material (FJS-1)
- The result of the measurement had compatible values to other research results, however it had large uncertainty due to the heat loss
- The second setup was built considering the result of the first measurement

Thank you!



<4> Findings through JUACEP

(a) Students' reviews

(b) Questionnaires (in Japanese)

(a) Students' reviews

Super Great Experience in Michigan

Name: Shun Arakane

Affiliation: Micro-Nano System Eng. Nagoya Univ.

Participated program: Long 2015

Research theme: FABRICATION OF RADIO FREQUENCY DEVICES BY USE OF 3D PRINTING TECHNOLOGY

Advisor at Univ. Michigan: Prof. L. Jay. Guo

Affiliation: Electrical Electronics and Computer Science



My research topic in University of Michigan is fabrication of radio frequency devices by use of 3D printing technology. I learned basic knowledge about RF device and considered about how to make that kind of devices. I think it was precious experience that I could do a research which is different from what I have done in Nagoya University. I also think it was lucky I joined a big research group because almost all of members are Ph.D students or visiting scholar, so I could be inspired those people who had a lot of experience.

I lived with Taiwanese and Chinese roommates during staying in Michigan. Therefore, I had a lot of chance to speak English on a daily basis and that help me to improve my language ability. I also felt different culture from these roommates. At first, I confused the different life and attitude, but I gradually understood their culture. Also, I was able to meet so many people who have different cultures by joining meet up and conversation circle. I learned a lot of things from students because people living in US, even they are younger than me, have individual opinion and will. Their way of thinking increased my motivation.

When I had free time, I traveled many places in US. I visited magnificent palaces such as Grand Canyon, Grand Teton, Niagara falls and Yellow stone. These experiences were so good because I love nature. Moreover, I became to like American personality because when we went these places, many people greeted us. They are so bright and friendly.

Finally, I would like to thank many people involved in JUACEP. They gave me a chance to study in UM and planed our stay in US very well. I also appreciate great help from Prof. Guo group member. They helped and taught me when I was in trouble. Without their help, I would not have done anything. I definitely would like to go back Ann Arbor not in winter but in summer.



Grand Teton national park



Drinking with roommates and friends

What I learned from the diversity of cultures

Name: Takamasa Horibe

Affiliation (Dept & Univ): Aerospace Engineering, Nagoya University

Participated program: Medium 2015

Research theme: Series Elasticity for Haptic Interface

Univ. Michigan: Prof. Brent Gillespie

Affiliation (Dept.): Mechanical Engineering



The reason I applied to this program is to enlarge my view field. Before I participated in this program, I have been experienced many opportunities that totally changed my stereotype. When I was in Nagoya University, I met many friends who have different way to think from what I did and they changed my university life. They have a bottomless curiosity and are so active to learn not only in the lecture but also out of the lecture. They invited me to join some activities taken by foreign students and it was a first time for me to be involved foreign culture. I learned a diversity of idea and got to want to know what I do not know. Since then I got to try to know and accept the wide knowledge.

I experienced tons of culture shocks through this program. What I thought at first time in America is that there are still a lot of things I don't know. Actually the way to research of American people is completely opposite from that in Japan. They focus on how to make projects success and tackle researches so speedy. While when I did my research in Japan I often used to be stuck in a small problem and stop there in order to know the every little details, which is probably the basic style of Japanese researcher. I still don't know which style is better however I even have never thought deeply about my stile because I have no idea that there are the other stiles. Such an experience dramatically enlarged my idea or how I think. Of course I learned a lot of things in the American laboratory though I could also contribute for them as a Japanese student. We don't move speedy but we can see the detail and notice what they never notice. They told me that my style is typical Japanese style and it is new thing for them. By seeing the Japanese culture from out of Japan, I noticed many aspects that I never know if I didn't go out from Japan.

What changed my way of think is not only research. I talked a lot with my friends or my roommates and they are very ambitious. One of them studies international culture and we discussed each other about our culture. He told me what he knows about Japan or what he feels for Japan. It was very interesting because he told me not only a good thing but also a bad thing in Japan and I can't know how foreign people think of Japan.

Of course I went to travel somewhere on weekend and every places were amazing. The scale was totally different from Japanese one. I saw the real space shuttle at NASA's museum and I cannot forget about the scenery. That is one of the best trip for me as a student in aerospace engineering.

I could have a lot of friends in America and they all inspired my ideas and viewpoints. This is exactly what I wanted to learn through this program and I feel I could grow up and next step is not only be inspired by others but also inspire others. In addition I could also re-recognized a goodness of Japan, for example how delicious the Japanese food is! Hamburgers, steaks, BBQ, they were very good, however I always missed traditional Japanese food rice and miso soup.

Findings through JUACEP

Name: Hiroto Izuoka

Affiliation : Mechanical Science and Engineering, Nagoya University

Participated program: Medium 2015

Research theme: Nanofluidic-Flow-Assisted-Assembly of Well-Dispersed Plasmonic Nanostructures into Nanoslit Sensors

Advisor at Univ. Michigan: Prof. Xiaogan Liang

Affiliation (Dept.): Department of Mechanical Engineering



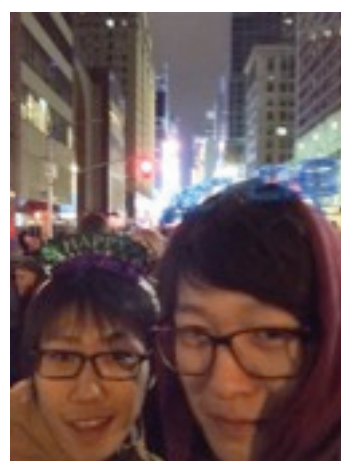
The whole experience I had through the JUACEP program is amazing. I really believe the experience in the US changed my perspective a lot. The stay in the US made me realize so many things that I would never realize without JUACEP.

I belonged to the Nanoengineering and Nanodevices laboratory Prof. Xiaogan Liang supervises at University of Michigan. The research project I was assigned to is establishing a new coating method of plasmonic nanoparticles on solid surfaces for biosensors. I spent most of my working time in cleanroom. The cleanroom in University of Michigan is a huge facility which has literally any equipment needed for the research. I also felt that collaboration between laboratories is stronger regardless of department than in Japan. My group also collaborates with other groups, actually. Opinions from the outside of the group definitely helped to make the progress. Of course, I sometimes faced difficulty in my research, but I felt satisfaction I've never had every time I overcame such challenges. You might know that JUACEP program is not for English training. I'm pretty sure JUACEP gave me a great experience I wouldn't get through any other programs.

One more thing I really want to share is about a lot of Asian students studying in the US. The most interesting characteristic of our lab is that all of the students are from Asian countries. I didn't know that such many Asian students are studying abroad until I went to the US. Once you get there, you must realize the number of Japanese students in US is still small. I hope more Nagoya University students get to have some interest in studying abroad and decide to go. I promise your decision will help you in different ways and you'll never regret it.

In addition, I enjoyed traveling in the US during my stay. I went to New York to celebrate the New Year with my roommate who is from Mongolia. We are standing in front of the Times Square for 8 hours. Although such kind of experience seems stupid, I recommend you to try something you can't do in Japan.

Finally, I really appreciate JUACEP for giving me such a wonderful time.



Findings through JUACEP

Name: Michihiro Kanie

Affiliation: Department of Micro-Nano Systems Engineering,
Graduate School of Engineering, Nagoya University

Participated program: Medium 2015



Research theme: • 3D-Printing of Porous & Solid Silicone Structure,
• Pin-on-disk Wear Study of the Fused Deposition
Modeling Materials

Advisor at Univ. Michigan: Prof. Albert J. Shih

Affiliation: Department of Mechanical Engineering, University of Michigan

I belong to the group of Prof. Albert J. Shih lab for 6 months in JUACEP program. He continuously supported my study and research. I joined the project of "Silicone Printing". Originally, I do research for 3D-printing in Japan. That's why I am very interested in his lab. I got a lot of knowledge about 3D-printing Systems, Software, Code and Materials.

He is really kind to share a lot of things not only research with me like house party. It was so great time. I remember I was very surprised when I went to his house first time because his house is so big. We took a walk around his house and took 30 minutes. Also, the dishes of his wife were really delicious. I ate a lot of traditional Taiwanese dishes.

Also, I really like lab-mate. Not only research, we often went to lunch and dinner, were chatting, played foosball and held a party. They absolutely made my life in Ann Arbor wonderful. They should definitely play a great role around the world in the future. I will meet them in the future.

Actually, this is the first time to go abroad for me. Everything is new for me like view, road and food. When I went to a restaurant just after I arrived at Ann Arbor, I was surprised because a clerk started to clean up floor when I still was eating. Almost Japanese should think it is very rude. Of course, I don't care that too much now. I mean it is easy to get used to the atmosphere in America for me. Because of my personality like talkative and outgoing, I made a lot of friends here. I often joined parties and events like Halloween, Thanksgiving, Christmas and New Year. Fortunately, there are many people from different countries. It was so nice chance to know their culture and teach Japanese one. Now, I care not to see everything based on only Japanese values. It is very important to keep Japanese values like polite, kind and respectful, and understand other culture. For example, American are really aggressive and outgoing unlike Japanese are shy. We should not be shy not to be able to say our opinion. I want to be a person with good point of personality in each country.

Also, I tripped to many places in America like New York, Boston, Las Vegas, Los Angeles and San Diego. Each place has each specialty. Especially, I like Boston because the view of seaport and glass buildings at night was so beautiful, and a clam chowder was really tasty.

At last, I would sincerely like to thank the Japan-US Advanced Collaborative Education Program (JUACEP) and staff for giving me the great experience. I will greatly take advantage of this experience. Thank you.



Prof. Shih's Group



Thanksgiving



Halloween



Lunch & Dinner

Findings through JUACEP

Kiichi Okuno

Dept. of Mechanical Science and Engineering

Graduate School of Engineering, Nagoya University, Japan

Participated program: 6-month stay 2015



Research theme: Vibration-Based Identification of Interphase Damping of Bamboo FRP

Advisor at University of Michigan: Prof. Bogdan Epureanu

Affiliation: Dept. of Mechanical Engineering

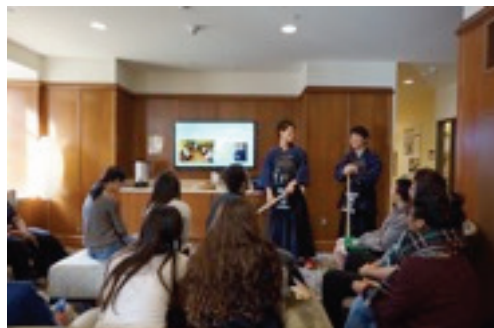
Firstly, I'd like to mention my research project at University of Michigan. During the stay, I worked on modeling the vibration phenomena of unidirectional FRP (Fiber Reinforced Plastics) and clarifying the interphase damping of the materials. Since neither vibration nor modeling is related to my research project in Japan at all, it was hard to understand things at first. But I studied hard to acquire new knowledge, tried hard to complete modeling the complicated phenomena and worked hard to get a good result. Thanks to my professor's professional and kind support, I made a good progress in my research and gained a lot of skills necessary to be a better engineer in the future. In addition to my own research project, I also joined weekly research meetings in my lab, and it was a great opportunity to get to know how the students in one of the best ME program in the world would approach their own problems and solve them. I was very surprised and inspired by their wide knowledge and experiences gained by intense studies for classes and several internships.

Other than the research, I've got too many to share in this report. This was my first time living abroad, and I had a lot of experiences that I had never had before. Let me list up some of the things I experienced for the first time in my life through this program; having a roommate (actually I had two during the stay), living in a college dorm, some foods that I had never had (turkey on Thanksgiving for example), going to a church, going to a house party, giving a Kendo lecture to non-Japanese people, watching a football game at an insanely big stadium, NBA games, driving a left-wheel car on the right side of a road,,, I could just keep going on and on like this. And more than anything, I made some close friends there! It was amazing to share my surprise, confusion, excitement, and joy with them. I'd like to thank all of them for the awesome days we spent together. I will never forget them. I'm looking forward to seeing them again when they come to Japan, or maybe when I visit the states.

Through these experiences, I've realized how unique and closed Japan is, how different and difficult it is to live in a foreign country with people from different backgrounds, and also the importance of being aware of these things. I'd always thought these convenient systems in clean cities, society with politeness and privacy, and people working until very late night are normal. But everything normal in Japan is not necessarily normal, sometimes even extraordinary, in other countries. I feel a little more confident now that I've got this completely different perspective because I'm sure this will help me go up my career ladder faster.



With one of my best



Kendo lecture



My laboratory

Findings through JUACEP

Name: Ryo Yamaguchi

Affiliation (Dept & Univ): Mechanical Science and Engineering,
Graduate School of Engineering,
Nagoya University

Participated program: Medium 2015

Research theme:

Advisor at Univ. Michigan: Prof. Peter F. Green

Affiliation (Dept.): Material Science and Engineering, University of Michigan



I spent 6 months in Ann Arbor, Michigan. First, I explain my research work that I had done in University of Michigan. I belonged to the laboratory for complex materials and thin film research. In this laboratory I examined the glass transition temperature and the physical aging rate of the star shaped polystyrene (SPS) and SPS nanocomposites which contain polystyrene grafted gold nanoparticles. Because no one has examined nanocomposites system before, I had to look for the annealing condition to bring nanocomposite films to equilibrium state. Therefore I could not acquire enough data that I expected.

Secondly, I would like to share what I learned from my daily life in Ann Arbor. Although there are not many Japanese students in University of Michigan, there a lot of students who are interested in Japanese culture such as animations and comics. I bitterly regret that I had not watched Japanese animations and read Japanese comics. While I lived with Chinese students, we talked about history education that we had gotten in each country. There should be only one fact, but we learned completely different history. We realized that we have to think from several points of view to understand each other. From these experiences, I strongly felt that I should have learned about Japanese culture and history before studying abroad.

Thirdly I introduce some pleasant memories. I enjoyed watching a football game and a NBA game. As for the football game, there were over 100,000 people in the stadium although the game was the university football game. I also enjoyed traveling in U.S.A. such as New York, Pittsburgh San Francisco and Los Angeles. Each city has distinctive culture and atmosphere. However, people were kind to help me whenever I went. To be honest, there are still a lot of places where I want to visit hopefully I will come back someday.

Finally, I would like to express gratitude to the persons concerned. Especially I appreciate JUACEP to give me such a precious opportunity and kindly support, Prof. Umehara to send me on studying abroad and Prof. Green to accept me and give me a lot of invaluable advice. I will try to make use of this experience in the future.



Home party with lab mates



Metropolitan Museum of Art, NY

The life in Ann Arbor and my experience

Name: Shintaro Oyama

Affiliation: Mechanical Science and Engineering, Nagoya University

Participated program: Short 2015

Research theme: Effects of Micropores on Pseudocapacitive Charge Storage in Vanadium Nitrides

Advisor at Univ. Michigan: Prof. Levi Thompson

Affiliation: Department of Chemical Engineering



I had spent in the University of Michigan for 2 months and researched about electrochemistry under Prof. Levi Thompson and with Thompson group. I would like to introduce the life in Ann Arbor and share my experience.

The University of Michigan is located in Ann Arbor, Michigan. It takes 45 minutes from Detroit to Ann Arbor, and Ann Arbor is one of college town in USA. I rarely felt in danger for 2 months, so I could say that Ann Arbor is one of the best cities to live in. And there are some grocery store dealing with Japanese food, drink, seasoning in Ann Arbor, so I was able to make and eat Japanese dishes by myself.

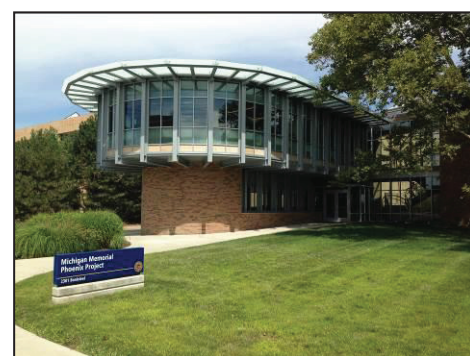
In the University of Michigan, I studied about electrochemistry, especially supercapacitors, in Thompson group, and the research region is completely different from my major in Japan. Firstly, I thought it was difficult to study under him, but Prof. Thompson readily complied with my request to join his group. Thanks to Prof. Thompson, my mentor and Thompson group members, I was able to study and progress my research project in UM. I really appreciate them.

I played badminton with many Taiwanese every Monday, and played soccer with many people from many kinds of countries every Thursday. It was very exciting. I can make many friends there. On some weekend, I went BBQ with other laboratory members, went to Chicago with Japanese friends, watched football game at "Big House" or drank with laboratory members. I really enjoyed whole of life in Ann Arbor.

Finally, I would like to thank JUACEP for Financial support to my study-abroad life, and thank my supervisor, Prof. Noritsugu Umehara for allowing me to join this program. I'm sure this study-abroad life has changed my life.



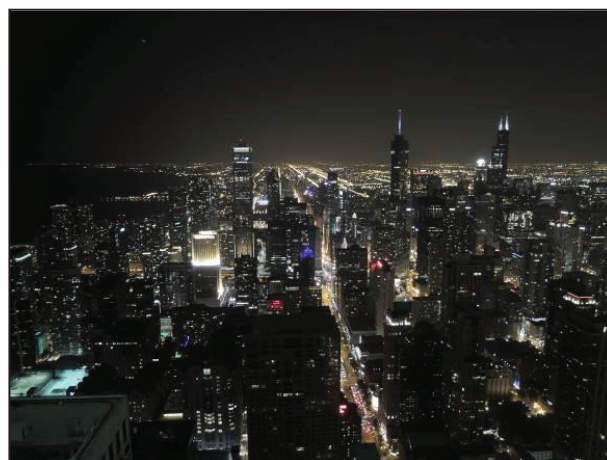
Mentor and me



Laboratory building



Friends who played soccer together



Chicago's night view

Findings through JUACEP

Name: Takahiro Hatano

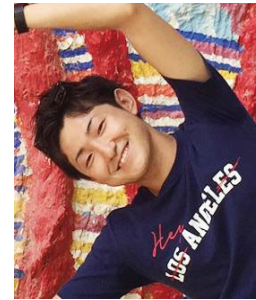
Affiliation: Mechanical Science and Engineering, Nagoya University

Participated program: Medium 2015

**Research theme: Micro/Nano Sensing Technique on Diamond Tip
Using Microwave**

Advisor at UCLA: Prof. Xiaochun Li

Affiliation: Mechanical and Aerospace Engineering



This 6 months I had lived in Los Angeles are irreplaceable time for me. Los Angeles has a variety of races and wonderful climate. This is the reason why I chose to study at UCLA. There were many excellent students in UCLA. However, their vision of the future was different from the one of excellent Japanese students. Some of them said to me, "Will you start to work right away after finishing university? There might be more important thing you should for your future." Therefore, I became to think that I broke a shell of the sense of values which rooted in myself and I wanted to think about how I live in the life.

In my research, I studied micro/nano sensing technique. In the first several months, I had gained knowledges on my research theme. As the next step, I set up experimental condition. However, I had some troubles. The apparatus which I wanted to use didn't exist. So I asked private company to do the experiment, but it cost too high. Finally I could not conduct an experiment, but I gained various knowledges and learned attitude towards research.

In my daily life, I usually go to university on weekdays and hung out or go to trip with my friends on weekends. UCLA has a well-equipped gym, so I often go there after finishing researching. Furthermore, Los Angeles has a lot of funny places, such as Santa Monica, Hollywood, Beverly Hills, Venice beach and Universal Studios. It is also easy to go to Las Vegas, Grand Canyon, San Diego, San Francisco and Disneyland Resort. Therefore I spent a very satisfying weekend. It rains little, and Los Angeles has a comfortable climate.

I would like to thank JUACEP for providing me this precious study opportunity. This exchange program gave me a chance to think about how to live my life properly.



UCLA



Driving around Los Angeles



Farewell dinner with lab members

Findings through JUACEP

Name: Yusuke Kasai

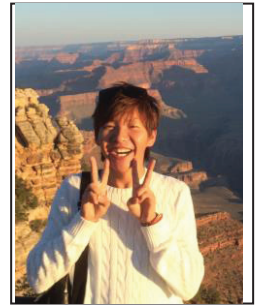
Affiliation: Micro-Nano Systems Engineering

Participated program: Medium 2015

Research theme: Study of Trapped Air under Shear Flow
Using Transparent Single Trench

Advisor at UCLA: Prof. Chang Jin Kim

Affiliation (Dept.): Mechanical and Aerospace Engineering



First of all, I would like to appreciate JUACEP gave me such a great opportunity to study in UCLA. The days I experienced in these 6 months will definitely be the foundation for my life.

Regarding study, I learned how to present in English. Our lab had group meeting every week and presented our progress of research for our professor. At first, because of my poor English and presentation skills, I could not communicate in group meeting well. However, practicing presentation every week, I gradually improved my skills and became confident to speak English. In the last month of exchange program, I taught 2 undergrad students to let them continue my research. I felt glad that they can continue my research and I became to teach my research in English as their senior. After the last meeting, our labmates held a farewell party for me. I thought it was pretty fortunate to be able to belong to this lab.

Regarding the life in Los Angeles, I touched a lot of cultures. I joined American home party many times. We bring not money but stuff such as drinks or snacks to the party, and we can meet our friends' friends. It is so fun and very good opportunity to learn other cultures. I really like American party, so after going back to Japan, I want to hold a party like this. In the end of January, we cooked Japanese foods and invited whole friends we met ever for the party. We talked about our memories, first impressions, future plans, etc. That was one of the most precious memories during this exchange program.



Farewell party with labmates



Farewell party with friends in LA

Life in LA

Name: Taichi Nakao

Affiliation: Micro-Nano Systems Engineering, Nagoya University

Participated program: Medium 2015

Research theme:

Advisor at UCLA: Prof. Suneel Kodambaka

Affiliation (Dept.): Materials Science and Engineering



I had been in UCLA for half year as a visiting researcher. I worked in-situ microscopy lab under Prof. Suneel Kodambaka who is my supervisor. My research project was about materials expected to apply the semiconductor industry. I think this project was worthwhile to do for me because my experimental results were actually sent to research institute. In fact, I could work very comfortably in this lab. My supervisor really cared about me like as I could do experiment soon when I arrived at UCLA and my lab mate was also very kind to me especially when I had a trouble in my life and I learned how to use some equipment. I'm so grateful to Kodambaka group.

In daily life, I usually spent the time with my lab mate. Actually, we often went to a bar after finishing our group meeting to drink many kinds of beer. It was so fun because there are many kinds of beer in LA we can't drink in Japan. We also went to the local brewery named as Absolution Brewing Company. Moreover, we often did home party. Japanese students were sometimes host, and other times American students were host. We could share the own culture each other.

I also went to trip around US, for example many kinds of National Park. There is really vast nature in US. The places I like in particular are Yosemite National Park and Death Valley National Park. Summer is good season for Yosemite, but I recommend going there even in winter because we can see wonderful view like the top covered snow of mountain. On the other hand, winter is good season for Death Valley National Park because it's really hot like about 125°F in summer. Here we can see many kinds of view, great landscape from top of the mountain, salt lake, and desert.

Finally, I could learn so many things I can't learn in Japan, English skill, culture, and friends around the world. Definitely, these experiences will be good effect to my future carrier. I would like to express highly appreciate to all people who supported this my awesome experiences.



Findings through JUACEP

Name: Shogo Okishio

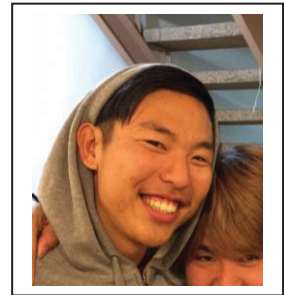
Affiliation (Dept & Univ): Aerospace Engineering, Nagoya University

Participated program: Medium 2015

Research theme: Measuring thermal conductivity of regolith simulant

Advisor at UCLA: Prof. Pilon

Affiliation (Dept.): Mechanical and Aerospace Engineering



My experience through the JUACEP program was simply amazing and unforgettable. I would love to write down so many things that happened during the stay in this paper but I have to pick up some since there is only a limited space here. It is really difficult to determine the best ones to talk about so I will start with the earnest topic. I felt that the research at UCLA was as tough as the ones in Nagoya University. I struggled to obtain the fine results and after all I was unable to make that happen. This was one of my regrets through the program. I did not feel much difference in the ability of student between Nagoya University and UCLA, although it is the one of the top university in the world. However I did feel the difference in future plans they talk about. I feel the students in Japan do not talk much about their own plans to strangers even if they had one and since I am the one who does not have specific plans, I was not able to talk what I want to do when people asked me about it. That reminded me that I need to think more about the purpose of the study now for the future.

Those were the most earnest opinions of my life and I will move on to the fun part. There were lots of experiences which I would have had any chance of trying them if I were staying in Japan. One of the most memorable things is that I joined the intermural futsal and soccer competition. First, I love playing soccer. I found out that there are some intramural competitions held in each quarters and started to look for the team. Since I did not know anyone who plays soccer here, I registered as a free agent and attended to the mandatory meeting. I thought this is a little bit unique style because I have never seen this kind of meeting being held in Japan for intramural competitions. In the meeting, I came up to this one team with holding a pizza in my hand. In this team, we played a league match once a week. We only gathered when we play the game or practice, however, it was absolutely enjoyable to play with them. We did pretty well in the futsal competition. Then in the next quarter, we gathered again as a soccer team with adding some guys. I only had one chance to play the league for this quarter but I was really glad that I had a chance to be in a team with them.

I definitely say that the most precious thing of this program is the opportunity of meeting new people. I guess I have met a thousand of people through this program. There are so many wonderful people out there and when you think back about the experiences of the entire program, you will probably recall about them and wish to have an opportunity to meet them again.

In the end, as the last sentence of the paper, I would like to thank my parents and my supervisors letting me to have this wonderful opportunity in the U.S.



What I studied in LA

Name: Takamichi Suhara

Affiliation: Materials, Physics and Energy Engineering, Nagoya University

Participated program: Medium 2015

Research theme: Electrical Transport Properties of Undoped
BaSi₂ Evaporated Thin Films

Advisor at UCLA: Prof. Kang L. Wang

Affiliation: Electrical Engineering



First of all, I'd like to express my appreciation to everyone I have met in United States. In addition, I thank JUACEP for giving such a great opportunity. The stay in Los Angeles for six month definitely change my future life.

I think UCLA is the best place to study ever. There are various students or researcher from the various countries and area. I could learn a lot of things not only research but also culture, life, people and so on. In addition, LA is very comfortable place to live and has a lot of enjoyable spots such as beaches, amusement parks and national parks. Therefore, I didn't have to worry about where I go in weekends or vacations. If I raise a bad point of LA, it's prices of stuffs. Especially, the fee for housing is very expensive here in LA.

For research in UCLA, it was a very good experience. In fact, there were a lot of difficulties for my research. I have never been able to get any results for first four months. It was very difficult time for me. The most important problem for me was communications. DRL in UCLA, which is a laboratory I joined during my stay, have so many students and researchers as many as forty people. Therefore, I needed to do any actions from me in first. Because I am shy, it was very difficult for me. However, I could remove embarrassment gradually. No, I needed to remove that. Of course, there are other difficulties than communication. It's definitely not easy to research at other places much less in other countries, however, I believe those difficulties must contribute to my life after going back to Japan. Thank you LA. Thank you US.



Research



Football game of UCLA

Findings through JUACEP

Name: Masaki Sato

Affiliation (Dept & Univ): Materials, Physics and Energy Engineering

Participated program: Medium 2015

Research theme: Growth and Characterization of Single-Crystalline
Zr(0002)/Al₂O₃(0001) and ZrC(111)/Al₂O₃(0001) Thin Films

Advisor at UCLA: Prof. Suneel Kodambaka

Affiliation (Dept.): Materials Science and Engineering



I stayed in ULCA for 6 months and studied materials engineering same as I do in Nagoya University. For research, I conducted a research of growth of thin films. That is exactly different from what I'm studying in Nagoya Univ. Therefore, in the first month, I was studying hard about this kind of area of study and practiced hard for experiment. Thanks to detailed advice and continuous support by my lab mates, Josh FankHauser and Dr. Abbas Ebnonnasir, I could get skilled enough to do experiments by myself. Prof. Kodambaka always gave me very helpful and incisive advices. I worked in lab and did experiments almost all weekdays. It resulted in 2 papers being prepared for publish.

I went hang out with lab mates so many times. We went bars almost every week. I'm very happy that I met these wonderful people. We shared almost all happy, fun and crazy time.

We hosted three Japanese parties. I think, people in USA are very interested in and excited for Japanese food. Of course, sushi is the most famous. But, some are really interested in authentic ones. I was very happy that many people asked me about the recipes.

For traveling, in winter break, I visited Vancouver, Seattle, Portland and San Francisco. I tried 20 different Breweries and more than 60 different crafted beers. Beer in USA is very different from them in Japan. I didn't like bitter beer so much before I went to USA. But, now I'm kind of addicted to them. I'm not alcoholic though. We can't find many of them in Japan. Therefore, I really want to go beer tour to USA and try many different types of beer.

In conclusion, I gained my weight by 15 pounds in 6 month. I had to be more careful about health but, beer and the Mexican foods didn't allow me to eat healthy.



Lab members



Japanese food party



BEER

Findings through JUACEP

Name: Junya Kato

Affiliation (Mechanical and Aerospace Engineering, UCLA):

Participated program: Short 2015

**Research theme: Dynamics of Dynamics of a Rotating Shaft
in Magnetic Bearing**

Advisor at UCLA/Univ. Michigan: Prof. Tsu-Chin Tsao

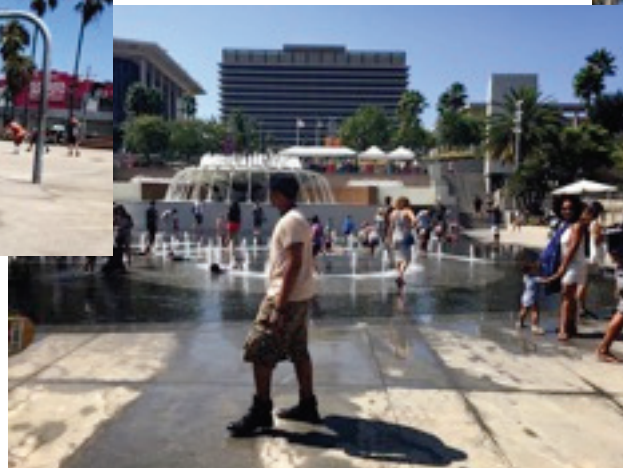
Affiliation: Mechanical and Aerospace Engineering



From August 3 to September 28, I did the research internship at UCLA through JUACEP program. In the laboratory which I belonged there are only Ph.D students, and all of them were older than me. So their experiences of life are really interesting. All of them have transfer from other university or colleges once at minimum, and some of them are foreign students. So by only studying in the laboratory they can place themselves in global environment. This is the really big difference from Japanese university. As a result of talking about them and knowing their experience I'd like to success in the world too.

I was also stimulated by American culture. At first I learned importance of making an assertion. In America we can't have my way without telling what I we want. Most of Japanese is not good at doing that, but if we can do, our life in America can be comfortable. Secondly, American people always enjoy their life each in their own way. When I went to the park holiday, I surprised. In the one park, there were so many kind of ways to spend time for example basketball, baseball, taking a nap, BBQ, skateboard, playing guitar, and anything like that. They enjoy what they want to do without caring about what others think of them. I think this culture is really great.

The stay at the Los Angeles where it is always sunny was exiting and fruitful for me. And the experience can't be replaced.



Awesome Experience

Name: Shunsuke Okumura

Affiliation (Dept & Univ): Department of Mechanical Science and Engineering,
Graduate School of Engineering, Nagoya University

Participated program: Short 2015

Research theme: Optimization of Deposition Conditions of Hexagonal Zr

Advisor at UCLA: Prof. Suneel Kodambaka

Affiliation (Dept.): Department Materials Science and Engineering



I had been in the US for 2 months, extremely short time. Basically I went to the lab and did my research and traveled on weekends. On weekdays, did my research from 10 am to 6 pm. All members in Kodambaka lab where I had been went to lunch together, so I could talk with the members in English. Friday is a pizza day, which means we had been to a pizza restaurant on every Friday. American pizza is not only big but also delicious. All senior members were so kind to me and always helped me. And experimental equipment was high-tech. Therefore, I enjoyed laboratory life.



On weekends, I traveled, hung out with my friends and experienced various things. I went to Universal Studio, surfing, Las Vegas, Grand Canyon, camping, music festival, etc. with my friends. All of them are quite awesome. Of course it took much money, but we enjoyed weekends.

I thought it was nice that weekdays and weekends are distinguishable in America.



UCLA Life

Name: Ikuya Onozato

Affiliation: Mechanical engineering, Nagoya University

Participated program: Short 2015

Research theme: Laser beams for 2D and 3D Worm Tracker

Advisor at UCLA: Prof. Katsushi Arisaka

Affiliation: Physics and Astronomy



Research

I visited University of California, Los Angeles for two months and worked in Prof. Arisaka laboratory. I did my research at Physics and Astronomy, while my department in Japan is Mechanical Engineering, so it was too hard to understand everything related to research. Furthermore, I could not communicate with laboratory members enough because my English skill was not good. However, thanks for the kindness of Prof. Arisaka and other lab members, I could make some progress by the end of summer and also do good communication with them. In our laboratory, not only doing research, but also professor held lab party at the end of every summer session and I spent great time!

LA Life

On weekdays, I went my lab at least from 9am to 6pm and I was thinking about my research after I came back to my hotel or apartment. Therefore, I did not have free time to go somewhere, but my English skill got better due to this work.

On holidays, we went to many places, for example, Hollywood, Anta Monica, and Dodger Stadium and so on, while I went lab or library sometimes. Besides the places there are a lot of kind foods, including hamburger, hot dog, ramen and especially Korean barbeque in LA, so I did not miss Japanese foods

Finally, I'd like to appreciate everyone, especially JUACEP, who gave me the great opportunity to study in UCLA for 2 months.



Precious days in LA

Name: Asami Yokoyama

Affiliation: Department of Chemical and Biological Engineering,
Graduate School of Engineering, Nagoya University

Participated program: Short 2015



Research theme: Thermo-responsive NanoVelcro Substrate
Technology
for CTC Purification and AR-v7 Mutation Analysis of Castration-
Resistant Prostate Cancer

Advisor at UCLA : Prof. Hsian-Rong Tseng

Affiliation: Department of Molecular and Medical Pharmacology, UCLA

All experiences in JUACEP were very exciting and stimulating for me. I am sure these experiences will change my future life dramatically.

I visited UCLA for 2 months and studied about Circulating Tumor Cells of prostate cancer in Prof. Hsian-Rong Tseng research group. Only a few students in the group and many staffs worked there. First communicating in English was very stressful for me because I couldn't speak English very well and understand what they were saying. However they were very kind and taught me everything about lab rules and their research field. A few weeks later after my program started I became to feel comfortable to talk with them and I studied from basic medical knowledge to applied one thanks to their help. They had a meeting everyday and that was helpful for me to learn medical expert English and research objects. And using real clinical samples was also precious experience for me because it is hard to handle them in my Japanese laboratory. From this experience I deeply recognized importance of research in Japan.



With Prof. Tseng



Temaki-sushi party



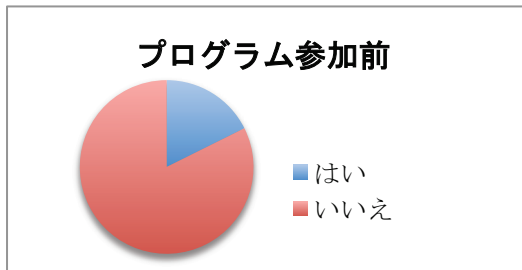
BBQ with JUACEP members

In addition, I visit many places in LA weekend and every experience was precious. Especially nature in USA, for example, Grand Canyon, sea in Santa Monica and uncountable stars was so impressive for me and I will never forget these scenes.

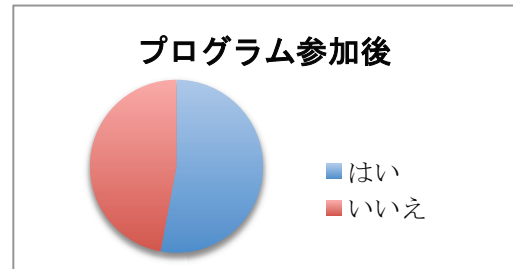
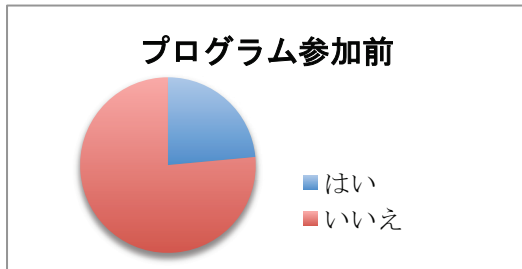
It was the first time for me to stay abroad for long time and so until just before my departure I was very nervous. But thanks to JUACEP's support I could spent precious time in LA for this 2 months. I appreciate all help both in USA and Japan for my studying abroad. If there is another opportunity, I would like to stay and live abroad for longer.

(b) 派遣プログラム参加者に行ったアンケート結果 概要

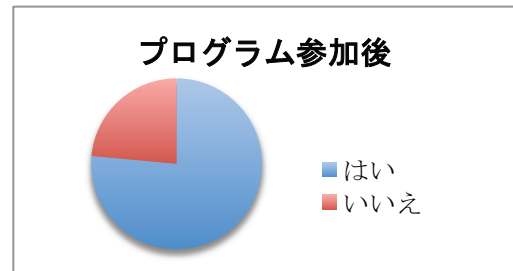
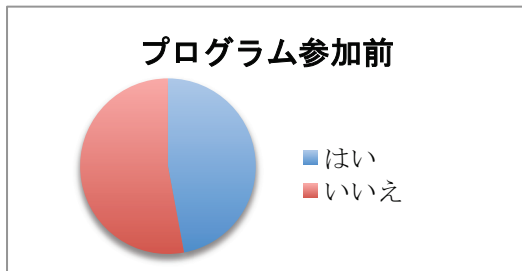
博士課程進学に興味がある



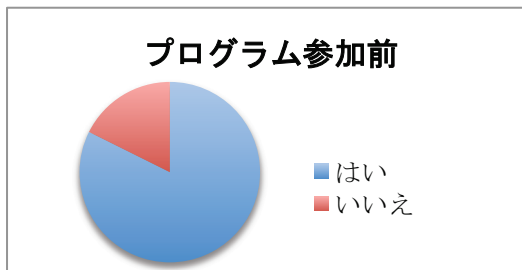
外国の大学での博士課程進学に興味がある



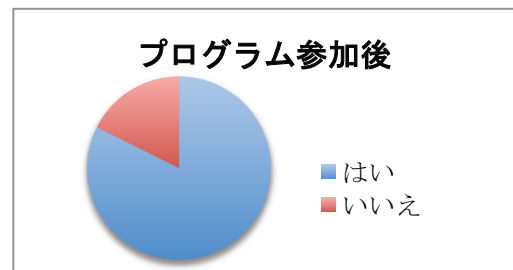
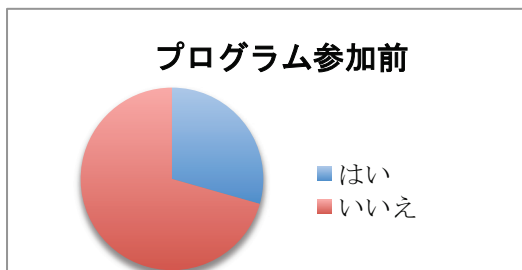
日本での外資系企業への就職に興味がある



外国での日系企業への就職（海外勤務）に興味がある



外国での日系以外の企業への就職に興味がある



1. このプログラムの良かった点（○）と改善してほしい点（×）について

- 最初の1ヶ月の宿泊代補助、航空券の補助、奨学金。
- 準備・資金・時間の壁をプログラムが低くしてくれたこと。
- 自分で受入れ研究室を選べたので、個人的にエンジニアとして身につけたかったスキルを得ることができた。
- 金銭的支援のおかげで家族にも大きな負担をかけずに済んだ。
- 自分で選んで自分で動かなければ何も進まないという態勢が私の性格に合っていた。
- 研究室の一員として研究できる点。
- 授業へも聴講者として参加できる点。
- 宿舎や研究において生活上の制約が特になく、自由に行動することができる。
- VGR (UCLA) としての在籍なので、単位は取得できないが高い学費を払うことなく半年間留学できる。
- TOEIC スコアでの応募が可能のため、応募のハードルは高くなかった。
- 就活時期を考慮して日程が設定されており、(M1 にとっては) 休学や留年の必要がなかった。
- 教員ワークショップの開催のおかげで受入れ教員が見つかりやすい。
- 留学手続きのほとんどを自分で行う点。多くの実務英語に触れるだけでなく、手続きの煩雑な米国文化を学んだ。
- 滞在ホテルが広くキッチンもあったので自炊ができ満足だった。
- 現地には、名大での JUACEP 参加米国学生がいるので、困ったことがあると助けてくれる。

- × 受け入れ研究室探しの補助。
- × 奨学金が足りない。家賃でほとんど消える。
- × 募集の段階で、どれくらい生活費がかかるのか具体的に示してもらえると経済的見通しがついてありがたい。
- × 過去の情報をもっと知りたかった、特に DS2019 やビザ取得において起きたトラブルなど。
- × 半年間のプログラムで授業一つ分の単位しか取れないこと。
- × 半年間は、研究で一つの成果を出すには短すぎた。
- × 参加学生の所属に隔たりがあると感じた。直接学生に募集案内が来るといい。
- × 短期は夏休み期間で比較的閑散としていたので、夏休み以外の期間も滞在したかった。
- × 宿舎に指定されたホテルが大学から遠い。
- × Semester に添わない留学期間だし、月の半端な日からの契約ができないため、アパート探しが大変。
- × UCLA での安全講習に参加しないと研究室の鍵がもらえないのだが、到着日が講習日当日で参加できず鍵の受け取りが2週間遅れてしまった。受入れ教授から「講習日の日程を確認して渡航日を決めてほしい」とのこと。
- × UCLA で指定している保険が高価なこと。他に保険を見つけておくべきだと思う。
- × VGR 費用を払っていても実験装置を使う権限は別。これが改善されれば研究成果が上がると思う。
- × 選考の過程や基準が不透明だと感じた。
- × 帰国直後のプレゼンはきつい。帰国間際まで研究しているので、プレゼン作成の優先度はどうしても下がる。集大成としての発表をするのだからきちんと準備させてほしい。
- × 個人の能力もあるかもしれないが、研究内容は受け入れ先に準ずるとしてしまった方が学生にとっては進行がスムーズで受入れ教員も要求をしやすいのではないかと。
- × 期間に見合った単位の取得があるといい。



2. 講義「国際共同教育外国語演習」についての感想（受講者のみ）

- ・ 初めて英語でのプレゼンを経験し、緊張・困難ともに良い経験だった。ただプレゼン準備などにとても時間がかかり、留学準備や他の授業・研究と並行させるのはとても大変だった。取得単位が2だとありがたい。
- ・ 講師のアドバイスの的確でわかりやすかった。
- ・ この授業を通して他の参加者と事前に知り合いになれ、情報交換が容易になった。
- ・ 留学先でもグループミーティングの際に役立つことが多くあった。毎回プレゼンできるので非常に練習になった。渡米前に英語を使う数少ない機会だったし、授業前後の講師との雑談さえありがたかった。
- ・ 渡航後に非常に有益だった。専門分野での英語表現のアドバイスがあれば更に充実したと思う。



3. その他、自由コメント

- ・ 手続きについての様々な支援、ありがとうございました。
- ・ ハイレベルの大学で研究経験できたおかげで、工学の学生として大きな実力となった。自分の将来のキャリアについて深く考えるきっかけになった。
- ・ 以前は、海外で活躍するという点について強い望みもなかったが、このプログラムを通して、海外で過ごすことの良い点も悪い点もリアルになり、結果として海外で仕事をしたいという気持ちが芽生えた。非常に有意義だった。
- ・ 研究内容・雰囲気ともに自分に合った研究室で、非常に充実していた。JUACEPや倉林コーディネータのアドバイスに心から感謝します。渡米後は英語力の拙さをしばらく痛感した。自分の準備不足もあるが、プレゼン以外にも英語力を養う授業があればさらにスムーズに活動できたと思う。
- ・ この留学を経て学んだことは数え切れない。
- ・ 理系院生にとっては留学は非常にハードルが高いと感じている中で、このようなプログラムは有意義。一方で、自分の専門分野と異なる研究を行う場合、半年は不十分だった。研修を受けないと使えない実験装置があることを考えると、1年留学に参加したかった。
- ・ プログラム内容から金銭的サポートまで素晴らしいプログラムなので何らかの形で継続して行ってほしい。この経験はこれまでの人生で最も自分の考え方に影響を与えた。
- ・ 研究内容は渡米後に教授と決めたが、新しい分野だったため知識を得るのに時間を要した。留学前に方針を決めていくべきだった。
- ・ 留学は以前から興味があったが、大学院では研究が忙しくてバイトで留学資金を貯めるのも難しいので諦めていた。その点ではとてもありがたいプログラム。両国で研究に集中することができた。
- ・ 渡航前は米国での研究に対するアカデミックな方面ばかり考えていたが、終わってみると、文化や考え方の違いから得るものが多かったと思う。その意味で、周りにほとんど日本人がいない環境に身を置いた学べることの多い留學生活だった。



Copyright © JUACEP 2015 All Rights Reserved

Published in February, 2016


Leaders of JUACEP

Professor Noritsugu Umehara

Professor Yang Ju

Japan-US Advanced Collaborative Education Program (JUACEP)

Graduate School of Engineering

Nagoya University  名古屋大学
NAGOYA UNIVERSITY

Furo-cho, Chikusa-ku, Nagoya 464-8603, Japan

JUACEP@engg.nagoya-u.ac.jp

<http://www.juacep.engg.nagoya-u.ac.jp>

